UNIVERSITAT POLITÈCNICA DE CATALUNYA
BARCELONATECH

Multimodal Microwave Filters

Author:
Adrián Arturo Contreras Lizárraga

Advisors:
Lluís Pradell i Cara
Miquel Ribó i Pal

Thesis submitted to the Universitat Politècnica de Catalunya in partial fulfillment of the requirements for the Degree of Doctor of Philosophy in Signal Theory and Communications

Department of Signal Theory and Communications
Radio Frequency and Microwave Systems, Devices and Materials Group

Barcelona, September 12th, 2013

ABSTRACT

This thesis presents the conception, design and implementation of new topologies of multimodal microwave resonators and filters, using a combination of uniplanar technologies such as coplanar waveguide (CPW), coplanar strips (CPS) and slotlines. The term "multimodal" refers to uniplanar circuits in which the two fundamental modes of the CPW propagate (the even and the odd mode). By using both modes of the CPW, it is possible to achieve added functions, such as additional transmission zeros to increase the rejection, or to attenuate harmonic frequencies to improve the out-of-band rejection. Moreover, it is demonstrated that by using multimodal circuits, it is possible to reduce the length of of a conventional filter up to 80%. In addition to bandpass filters, new topologies of compact band-stop filters are developed. The proposed band-stop filters make use of slow-wave resonators to decrease the total area of the filters and achieve compact topologies.

This work also addresses the development of synthesis techniques for each multimodal filter. The design equations were obtained from generalized multimodal circuits available in the literature, which have been adapted for each particular case and modeled as basic filter components, such as immitance inverters or lumped elements. By using the proposed synthesis equations, it is possible to design filters with a desired response and relative bandwidth. The use of the proposed synthesis enables a fast analysis and design of multimodal filters using circuit simulators.

As an added feature, several reconfigurable and tunable filter topologies were demonstrated, using active devices (PIN diodes and varactors) or RF-MEMS. These new topologies demonstrate the flexibility of multimodal circuits. For the RF-MEMS-based tunable filters, different capacitive and ohmic switches were designed, fabricated and measured. As an example of the additional degrees of freedom using of RF-MEMS and multimodal CPW circuits, a reconfigurable filter using RF-MEMS switchable air-bridges as a reconfiguration device has been demonstrated in this work for the first time.

ACKNOWLEDGMENTS

I would like to thank all the people who helped me during my work towards my PhD. First, to my advisor, Prof. Lluís Pradell, for his support and for guiding me since my arrival to Barcelona. My sincerest gratitude for his help and patience during the development of this work. Thanks also to Prof. Miquel Ribó for his invaluable help in multimodal circuit theory, without which it would have been impossible to conclude this thesis successfully. Thanks to Prof. Jasmina Casals-Terré, for her comments regarding RF-MEMS and for introducing me to multiphysics analysis.

I would like to thank to all members of the FBK-irst MEMS group, especially Flavio Giacomozzi, for his support and for sharing his knowledge in RF-MEMS and microfabrication (also thanks for all the nice pictures of RF-MEMS devices). Thanks to Dr. Jacopo Iannacci for his help regarding wafer masks and for his support. Thanks to F. Solazzi and Sabrina Colpo who helped me with FEM simulations and fabrication issues, respectively; and to Dr. Benno Margesin for accepting me as a visiting PhD student at FBK.

Thanks to Dr. Pierre Blondy for accepting me as a visiting PhD student at XLIM, and for sharing his knowledge in RF-MEMS and tunable filters. Thanks also to all the PhD students of the MINACOM group who kindly helped me during my stay. Also thanks to Dr. Tauno Vähä-Heikkilä for accepting me as a visiting PhD student and to Pekka Rantakari who helped me during my short stay at VTT, in Espoo, Finland.

I would also like to thank the technical staff of the TSC department: Rubén, Joaquim and Albert, for fabricating the majority of the prototypes. Also, thanks to the UPC students working in final-year projects who helped with EM simulations and matlab scripts: Marc, Nacho, Adrià, Carles and Sergi.

Thanks also to the administrative staff of the TSC department, especially to Teresa and Aynie who always helped me to schedule my trips and with my financial issues.

This work was completed under the generous support of the spanish taxpayers through the projects TEC2010-20318-C02/TCM and the fellowship BES-2008-004923 from of the Spanish Ministry of Science and Innovation.

I would like to thank my all my PhD colleagues (all of them; Mexicans, Colombians, Spanish and Catalans) who helped me during my work, and for their camaraderie. Thanks to E. Diaz for his positive attitude and for helping me during the final steps of my PhD. Thanks also to L. Yam for his philosophical comments during lunch time. Thanks also to Dr. Ignacio Llamas, for his camaraderie during URSI and other conferences.

A very special thanks to Franzi for enduring my night work hours and for helping me to find grammatical errors in this work, and for taking care of me after my appendix surgery... thank you for being there.

Finally, I want to thank my family: Dalia, Arturo, Monica and Gabriel for their help and support, even when they are passing through hard times.

Barcelona, September 2013.

CONTENTS

LIST OF FIGURES

LIST OF TABLES

Acronyms

C–V	Capacitance-Voltage
CPS	Coplanar stripline
CPW	Coplanar Waveguide
DC	Direct current
EM	Electromagnetic
FBK	Fondazione Bruno Kessler
FBW	Fractional bandwidth
FEA	Finite element analysis
FGCPW	Finite-ground coplanar waveguide
FLOMET	Floating metal
GSG	Ground-Signal-Ground
IL	Insertion loss
LPCVD	Low pressure chemical vapor deposition
LTCC	Low temperature co-fired ceramic
LTO	Low temperature oxide
MEMS	Microelectromechanical System
MIM	Metal-isolator-metal
PCB	Printed circuit board
RF	Radio frequency
RF-MEMS	Radio Frequency Microelectromechanical System
rms	Root mean square
SAB	Switchable air-bridge
SG/GS	Signal-Gound/Ground-Signal
TEOS	Tetraethyl orthosilicate

CHAPTER 1

INTRODUCTION

1.1 Uniplanar circuits

THE COPLANAR waveguide (CPW), the coplanar stripline (CPS), and the slotline are uniplanar microwave transmission lines in which shunt and series components are easily mounted [6], and have a good behavior at high frequencies. Uniplanar transmission lines offer unique advantages in RF and microwave circuit design. Their fabrication is simpler than that of microstrip or any other multilayer technology, making uniplanar circuits attractive in terms of cost reduction. In contrast to microstrip technology, uniplanar techniques allow a mixture of transmission line configurations to be used together, thereby making available a wide range of novel passive microwave structures [7–14]. The CPW, the CPS and the slotline (in this work, the word slotline will be also used to refer to the CPS, even though the CPS metal planes are narrow), can be combined to develop new circuits that cannot be achieved with microstrip topologies. The slotline (and the CPS) is a monomodal transmission line, but the CPW is a multimodal guiding structure that can simultaneously propagate two fundamental modes (the even and the odd modes, shown in Fig. 1.1, which interact at any asymmetry or transition [1, 11, 15–18].

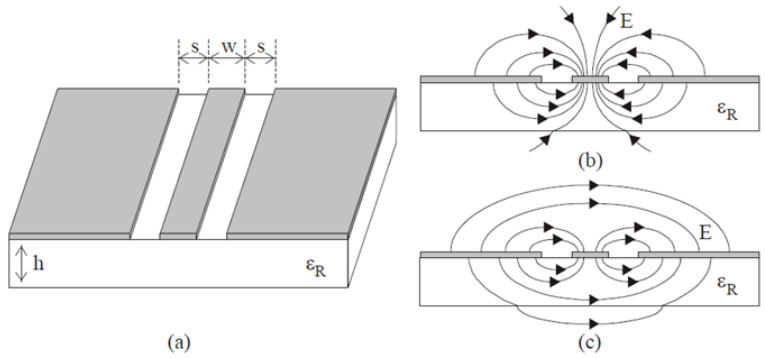

Figure 1.1 – (a) CPW and transversal electric field. (b) Even mode (c) Odd mode [1].

In practice, each mode can be excited by using GSG probes (CPW even mode) or SG/GS probes (CPW odd mode); to obtain its characteristic parameters (impedances and propagation constants) from measured data. As shown in Fig. 1.2, the characteristic parameters can be also obtained by using full-wave solvers, using the correct port configurations as described in [11, 19].

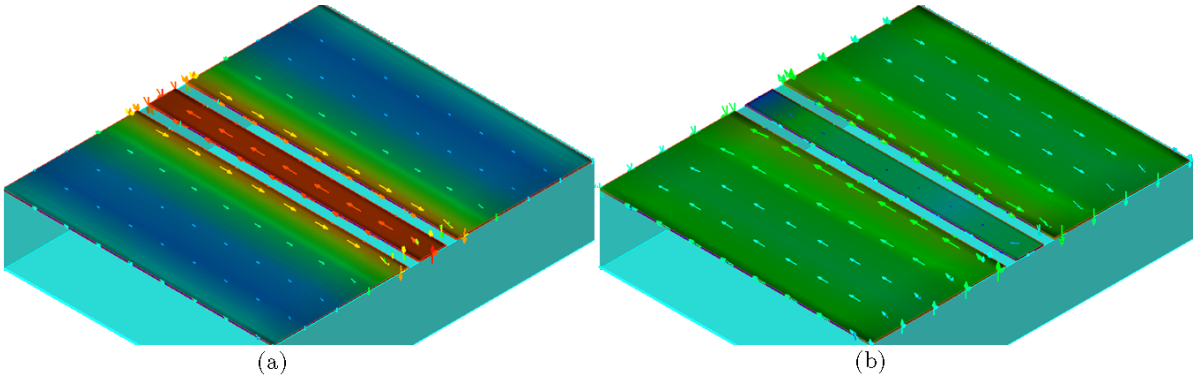

Figure 1.2 – Full-wave simulation of the current distribution in a CPW. (a) Even mode. (b) Odd mode.

The fact of having two fundamental modes in a transmission line offers a further degree of freedom for the design of uniplanar circuits. Indeed, new uniplanar multimodal circuits (that are not a direct replica of microstrip topologies into CPW even-mode topologies) can be designed, which feature good reconfiguration, compactness, and low-loss capabilities. For instance, in [20], the mul-

timodal concept was applied to a uniplanar 180° hybrid and, in [21] and [2], to wide-band, micro-electromechanical (MEMS)-based 0°/180° phase switches (see Fig. 1.3).

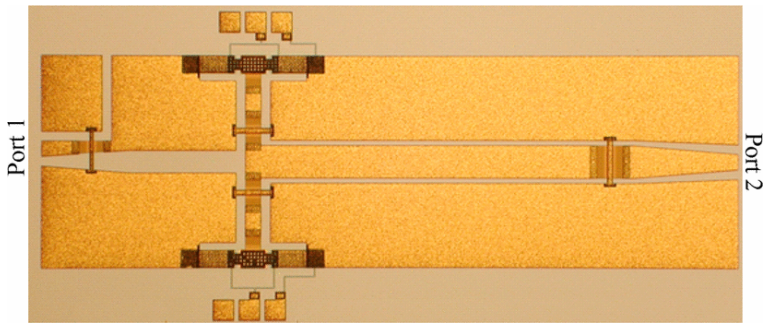

Figure 1.3 – RF-MEMS uniplanar 180° phase switch based on a multimodal air-bridged CPW cross [2].

In contrast with microstrip filters, few uniplanar filter topologies have been proposed. However, it has been proven that, by using uniplanar transmission lines, it is possible to obtain filters with small dimensions, high quality factors [22–27], and easy reconfiguration [28,29]. In [23], compact uniplanar filters with quality factors up to Q_0 = 240 were demonstrated, and in [24], a compact conductor-backed CPW-slotline bandpass filter with high selectivity was reported. In [30], a compact CPW two-pole band-stop filter, with an area of $(\lambda/4)^2$ was developed. Higher order uniplanar filters with ultra-low losses can be obtained using superconductive films, as demonstrated in [26]. In [27], a 16-pole filter using 3-D slotline resonators was presented, featuring a mid-band insertion loss lower than 0.5 dB.

Regarding CPW filters, nearly all topologies reported in the literature are even-mode circuits that replicate microstrip topologies and suppress the odd mode, considered as spurious, by means of air bridges [31, 32]. For example, the resonators and filter topologies reported in [30, 33–37] use air-bridges to suppress the CPW odd-mode, without taking advantage of both propagation modes of the CPW.

However, the use of both propagation modes can offer additional advantages compared to monomodal uniplanar circuits.

1.2 Scope and limitations

This work focuses on the design of new topologies of multimodal microwave filters using coplanar waveguides, which can be modeled using generalized circuits models proposed in [1]. A recent thesis involvining multimodal microwave circuits [38] included the design of a new type of CPW-slotline transition, a 180º uniplanar hybrid and new reconfigurable multimodal phase switch using RF-MEMS. This thesis follows a similar approach, focusing on the conception, design and implementation of feasible topologies of multimodal microwave filters. Moreover, this thesis proposes synthesis techniques for multimodal microwave filter topologies (band-pass and band-stop), which can be used to design structures with a defined response (e.g. Butterworth, Chebyshev) and fractional bandwidth (FBW). In addition, new tunable or reconfigurable topologies of multimodal microwave filters are developed, using active devices (e.g. PIN diodes or varactors) and RF-MEMS devices. For the latter, different capacitive and ohmic RF-MEMS switches were designed, implemented and characterized. The development of the RF-MEMS switches and the new tunable or reconfigurable filter structures was carried out using the technology of an external foundry process [5].

1.3 Objectives

A fundamental part of this work is the research of feasible multimodal microwave filters structures, which can be designed using synthesis methods based in circuits models proposed in [1]. Therefore, the main objectives of this thesis are:

• Investigate new physically realizable multimodal resonators and filters, with a performance similar to existing traditional monomodal structures.

• Explore the advantages (compared to monomodal structures) of multimodal filters, such as: compactness/size reduction, easy reconfiguration, generation of additional poles or transmission zeros.

• Develop synthesis methods based on the multimodal circuit models of the new uniplanar multimodal filter structures.

• Design, implement and characterize the new topologies of multimodal filter structures.

Additionally, the following objectives are defined:

• Design and characterize RF-MEMS switches which can be used to design tunable and reconfigurable multimodal microwave filters.

• Develop new topologies of tunable and reconfigurable multimodal microwave filters, using active devices and RF-MEMS.

• Propose further applications of multimodal circuits.

1.4 Outline

This work is divided in 7 chapters. Chapter 2 shows the basic multimodal filter structures, circuit models and design equations. Chapter 3 is devoted to give a simple introduction into RF-MEMS theory, and deals with the design of the RF-MEMS switches used in this work. Chapter 4 introduces the design, implementation and validation of several multimodal band-pass filter topologies, based on the basic multimodal structures presented in Chapter 2. Chapter 5 deals with different topologies of tunable and reconfigurable multimodal bandpass filters, using PIN diodes, varactors and some of the RF-MEMS switches presented in Chapter 3. Chapter 6 presents two different topologies of multimodal band-stop filters, including its design, implementation and characterization. Finally, Chapter 7 draws the conclusions obtained form this work and future research topics.

CHAPTER 2

MULTIMODAL CIRCUITS

In asymmetrically-loaded CPW structures, there is an exchange of energy between the two fundamental CPW modes: the even mode, and the odd mode (or slotline mode). Most designs consider the odd mode as spurious and suppress it by means of air bridges, which do not affect the even mode. However, the odd mode can be used to achieve new circuit concepts. Asymmetrically-loaded CPW structures, modeled using multimodal equivalent circuits [15–18], can be used as a basis for new topologies of circuits, such as hybrids [20] and phase shifters [21]. This chapter introduces basic multimodal filter structures developed in this Thesis, along with their circuit models and design equations.

2.1 CPW circuits with asymmetric shunt impedances

CPW circuits with asymmetrical shunt impedances can be accurately modeled using the circuit model proposed in [16]. This section describes different types of CPW circuits with asymmetrical shunt impedances that can be used as bandpass resonators, band-stop resonators and immittance inverters.

2.1.1 Asymmetrically-loaded resonator

Fig. 2.1 shows a multimodal bandpass resonator. It consists of a CPW section limited by two air bridges between ground planes. This section has a slot short-circuited at appropriate distances (l_1 and l_2) of the air bridges. When an even-mode wave coming from any of the circuit ports (1 or 2 in Fig. 2.1) arrives at the asymmetric short circuit, outward-propagating even and odd-mode waves are generated. The even-mode waves are not affected by the air bridges, whereas the odd-mode waves are confined between the air bridges, forming a resonator of total length $l_t = l_1 + l_2$.

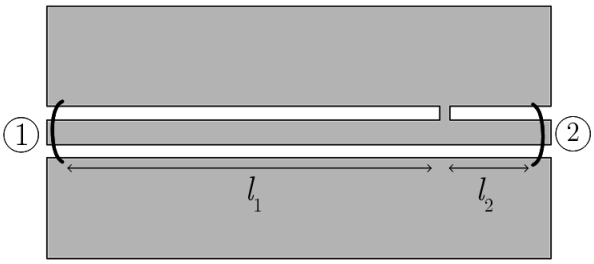

Figure 2.1 – Multimodal CPW bandpass resonator.

This resonator can be modeled using a simplification of the multimodal circuit model for asymmetric shunt impedances in CPWs [16], as shown in Fig. 2.2, where β_e, β_o, Z_{0e} and Z_{0o} are the propagation constants and characteristic impedances for the even and odd modes, respectively. It is clear from Fig. 2.2 that the odd mode forms a short-circuited transmission-line resonator shunt-coupled to the main even-mode transmission line. It will resonate at a frequency f_0 at which the resonator total length l_t is equal to $\lambda_o/2$ (where is the odd mode wavelength), not affecting the even-mode propagation. The sections where the CPW odd mode propagates, can be represented as two shunt stubs with input impedances $Z_1 = jZ_{0o}\tan(\beta_o l_1)$ and $Z_2 = jZ_{0o}\tan(\beta_o l_2)$. It is apparent that when l_1 or l_2 have a length $\lambda_o/2$ this stubs will produce transmission zeros at $f_{zero} = v_{po}/(2l_i)$, $i = 1,2$; where v_{po} is the odd-mode propagation velocity.

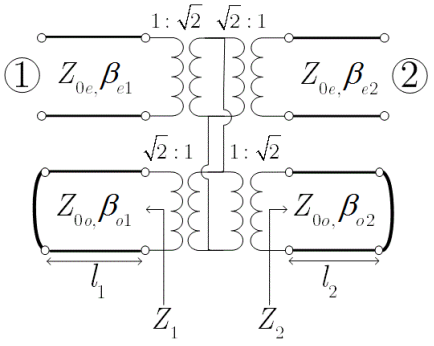

Figure 2.2 – Circuit model of the multimodal bandpass resonator.

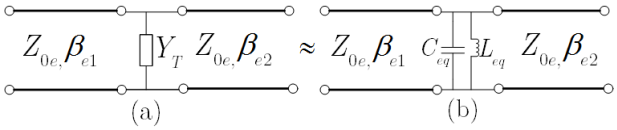

Figure 2.3 – Comparison between (a) a simplification of the circuit model of Fig. 2.1 and (b) a parallel LC resonator.

The whole resonant structure can be modeled by an admittance shunt-connected to the even-mode transmission line (Fig. 2.3(a)) of value

$$Y_T = \frac{-j4}{Z_{0o}} \left\{ \frac{1}{\tan\left[(\pi l_1/l_t)\left(f/f_0\right)\right]} + \frac{1}{\tan\left[(\pi l_2/l_t)\left(f/f_0\right)\right]} \right\}. \tag{2.1}$$

Since the resonator has a pass-band response, it can be locally modeled, near its resonance frequency, by a shunt LC resonator (Fig. 2.3(b)) of total admittance

$$Y_{eq} = j\left[\omega C_{eq} - 1/(\omega L_{eq})\right] = j\omega C_{eq}\left[1 - \left(f_0/f\right)^2\right] \tag{2.2}$$

where $f_0 = 1/(2\pi\sqrt{L_{eq}C_{eq}})$.Comparing the first-order Taylor-series coefficients for both Y_T and Y_{eq} around the resonance frequency f_0, it can be found that

$$C_{eq} = \frac{Y_{0o}}{f_0}\left[\frac{l_1}{l_t \sin^2(\pi l_1/l_t)} + \frac{l_2}{l_t \sin^2(\pi l_2/l_t)}\right]. \tag{2.3}$$

Thus, the capacitance C_{eq} can be changed by adjusting the position of the asymmetric short circuit (length l_1). Using (2.3) we can calculate the resonator fractional bandwidth

$$FBW = (\Omega_C/C_{eq})(g_1/Z_0), \tag{2.4}$$

where Ω_c and g_1 are the cut-off frequency and normalized element of the first-order low-pass filter prototype, respectively. Fig. 2.4 shows the frequency response of an ideal resonator with a center frequency . As can be seen, if the length l_1 increases, the FBW decreases, according to (2.4).

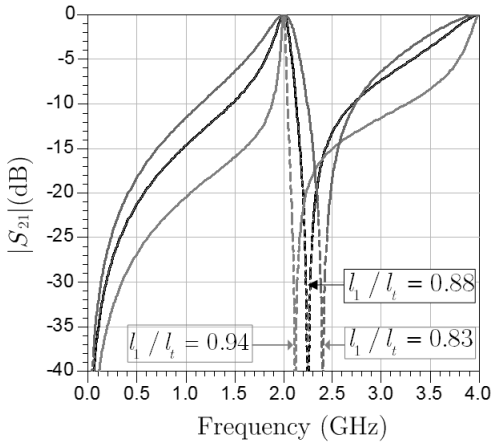

Figure 2.4 – Frequency response of an ideal multimodal bandpass resonator.

2.1.2 CPW – slotline transition as immittance inverter

Fig. 2.5 shows a multimodal immittance inverter. It consist of an asymmetric CPW transition, formed by a short-circuit in one slot of the CPW. This structure performs a modal conversion between the even mode of port 1 and the slotline mode of port 2 by means of a multimodal CPW section of length $l_{o1} + l_{e2}$, which simultaneously propagates the CPW even and odd modes. It can be modeled using a simplification of the multimodal circuit for generic asymmetric shunt impedances presented in [16], as shown in Fig. 2.6.

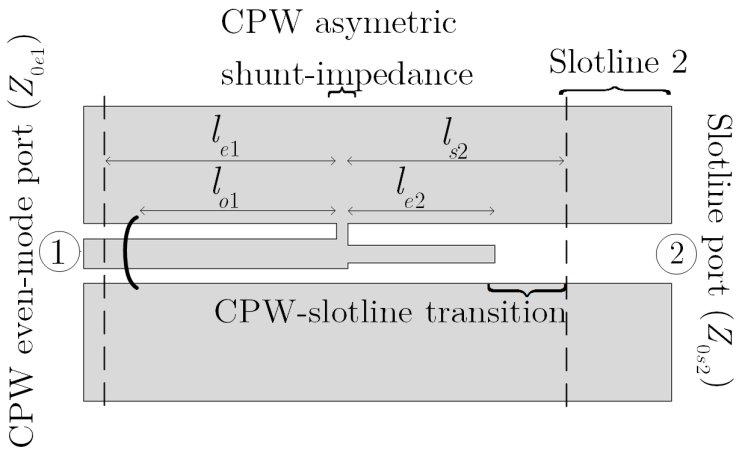

Figure 2.5 – Multimodal immittance inverter (MII).

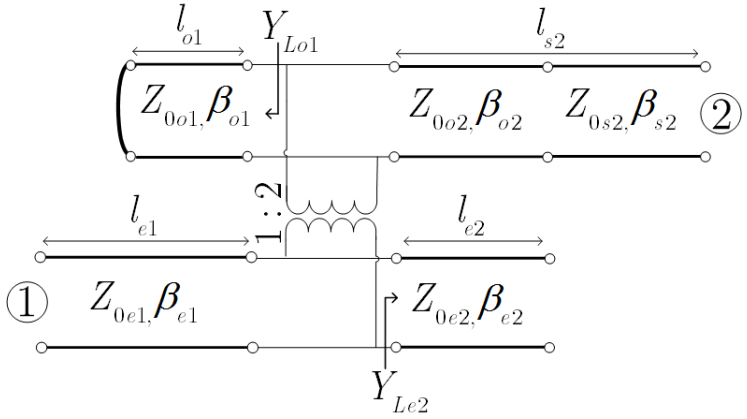

Figure 2.6 – Circuit model for the multimodal immittance inverter of Fig. 2.5. $Z_{0e1}, \beta_{ei}, Z_{0oi}, \beta_{oi}, Z_{0s2}, \beta_{s2}$ are, respectively, the characteristic impedances and phase constants of the even and odd modes of the CPW (i=1,2), and of the slotline mode.

From Fig. 2.6 is apparent that when an exciting even mode (the usual mode used in most CPW designs) propagating from port 1 arrives at the transition, reflected and transmitted even and odd modes are generated. The reflected even mode propagates back to port 1. The reflected odd mode is short-circuited with an air bridge at a distance l_{o1} from the transition, forming an odd-mode stub. The transmitted even mode propagates forward until the CPW-to-slotline transition, forming an open-ended stub of length . Finally, the transmitted odd mode propagates forward until the CPW-to-slotline transition, where it is transformed into a slotline mode due to their modal compatibility (it is assumed that $Z_{0o2} = Z_{0s2}$ and $\beta_{o2} = \beta_{s2}$), and reaches port 2. The S parameters of the inverter of Fig. 2.5, computed from its equivalent circuit of Fig. 2.6 (with port 1 referred to Z_{0e1} and port 2 to Z_{0s2}), are

$$S_{11} = \frac{Y_{0e1} - 4Y_{0s2} - 4Y_L}{Y_{0e1} + 4Y_{0s2} + 4Y_L} e^{-j2\beta_{e1} l_{e1}}, \tag{2.5}$$

$$S_{22} = \frac{-Y_{0e1} + 4Y_{0s2} - 4Y_L}{Y_{0e1} + 4Y_{0s2} + 4Y_L} e^{-j2\beta_{s2} l_{s2}}, \tag{2.6}$$

$$S_{21} = S_{12} = \frac{4\sqrt{Y_{0e1} Y_{0s2}}}{Y_{0e1} + 4Y_{0s2} + 4Y_L} e^{-j(\beta_{e1} l_{e1} + \beta_{s2} l_{s2})}, \tag{2.7}$$

with

$$Y_L = jB_L = Y_{Lo1} + \frac{Y_{Le2}}{4} = -j\frac{\cot(\beta_{o1} l_{o1})}{Z_{0o1}} + j\frac{\tan(\beta_{e2} l_{e2})}{4Z_{0e2}}. \tag{2.8}$$

The S parameters of a generic immittance inverter with inverter constant $K = 1/J$, characterized by a Y-parameter matrix

$$Y = \begin{bmatrix} 0 & jB \\ jB & 0 \end{bmatrix}, \quad J = \frac{1}{K} = |B|$$

are (with port 1 referred to Z_{0e1} and port 2 to Z_{0s2})

$$S_{11} = S_{22} = \frac{Y_{0e1} Y_{0s2} - B^2}{Y_{0e1} Y_{0s2} + B^2}, \tag{2.9}$$

$$S_{21} = S_{12} = -j2B\frac{\sqrt{Y_{0e1} Y_{0s2}}}{Y_{0e1} Y_{0s2} + B^2}. \tag{2.10}$$

By comparing (2.5)–(2.7) and (2.9)–(2.10), the design equations for the circuit of Fig. 2.5 as an immittance inverter can be derived as

$$|B_L| = \frac{1}{2|B|}\sqrt{\left(B^2 - 4Y_{0s2}^2\right) \cdot \left(B^2 - \frac{Y_{0e1}^2}{4}\right)} \tag{2.11}$$

for $|B| > \max\left(2Y_{0s2}, \frac{Y_{0e1}}{2}\right)$ or $|B| < \min\left(2Y_{0s2}, \frac{Y_{0e1}}{2}\right)$,

$$\beta_{e1} l_{e1} = \frac{1}{2}\arctan\left(\frac{8Y_{0e1} B_L}{16Y_{0s2}^2 - Y_{0e1}^2 + 16B_L^2}\right) \tag{2.12}$$

for $|B| > \sqrt{Y_{0e1} Y_{0s2}}$,

$$\beta_{e1} l_{e1} = \frac{1}{2}\arctan\left(\frac{8Y_{0e1} B_L}{16Y_{0s2}^2 - Y_{0e1}^2 + 16B_L^2}\right) \pm \frac{\pi}{2} \tag{2.13}$$

for $|B| < \sqrt{Y_{0e1} Y_{0s2}}$,

$$\beta_{s2} l_{s2} = -\frac{1}{2} \arctan\left(\frac{32 Y_{0s2} B_L}{16 Y_{0s2}^2 - Y_{0e1}^2 - 16 B_L^2} \right) \tag{2.14}$$

for $\left(Y_{0e1} Y_{0s2} - B^2\right) \cdot \left(16 Y_{0s2}^2 - Y_{0e1}^2 - 16 B_L^2\right) > 0$, and

$$\beta_{s2} l_{s2} = -\frac{1}{2} \arctan\left(\frac{32 Y_{0s2} B_L}{16 Y_{0s2}^2 - Y_{0e1}^2 - 16 B_L^2} \right) \pm \frac{\pi}{2} \tag{2.15}$$

for $\left(Y_{0e1} Y_{0s2} - B^2\right) \cdot \left(16 Y_{0s2}^2 - Y_{0e1}^2 - 16 B_L^2\right) < 0$.

For a desired value of J or K (and therefore of $|B|$), | $|B_L|$can be computed using (2.11). Then, from $|B|$ and $|B_L|$, the electrical lengths $\beta_{e1} l_{e1}$ and $\beta_{s2} l_{s2}$ can be derived using (2.12)–(2.15). The choice of signs of $|B|$,$|B_L|$, and in some values of $\beta_{e1} l_{e1}$ and $\beta_{s2} l_{s2}$, give several sets of valid design parameters. Finally, for a given sign of $|B_L|$, a suitable combination of electrical lengths of the odd-mode stub ($\beta_{o1} l_{o1}$) and the even-mode stub ($\beta_{e2} l_{e2}$) can be determined from (2.8). As explained below, these lengths can be conveniently chosen to produce additional transmission zeros in a filter. It should be noted that the port distances l_{e1} and l_{s2} , need not be longer than the stub lengths l_{o1} and l_{e2}, and that l_{e1} and l_{s2} can even be negative, thus absorbing lengths of transmission lines connected to them. It should also be noted from (2.12)–(2.15) that values of $|B| = J = 1/K$ in the range

$$\min\left(2 Y_{0s2}, \frac{Y_{0e1}}{2}\right) < |B| < \max\left(2 Y_{0s2}, \frac{Y_{0e1}}{2}\right)$$

are not physically realizable with this structure. This is not an issue for the intended use of this kind of inverters, since only either high or low values of immittance-inverter constants are required in the filter structures presented in Chapter 3.

In order to validate the circuit model of Fig. 2.6, an electromagnetic simulation of an inverter such as that of Fig. 2.5 was performed using Agilent Momentum, and compared with the results obtained with its circuit model. The parameters of the (lossless) inverter are: substrate relative permittivity ε_r=3.8, substrate thickness = 0.4 mm; CPW central-strip width w = 0.3 mm and slot with s = 0.2 mm; slotline slot with = *2s+w*; lateral-ground-plane width w_g = 1.4 mm, l_{e1} = 8.45 mm, l_{o1} = 6.8 mm, l_{e2} = 8.55 mm, and l_{s2} = 10.55 mm.

Fig. 2.7 compares the electromagnetic simulation of the circuit of Fig. 2.5 with the circuit-model simulation using Fig. 2.6. The good agreement between both simulations validates the circuit model of Fig. 2.6. It should be noted that, above 4 GHz, parasitics in the asymmetric shunt-short circuit transition become noticeable. They can be easily modeled by replacing the connection between the odd-mode transmission lines and the ideal transformer, with a small inductance L_{tp} (associated to the short-circuit in the upper CPW slot), as shown in Fig. 2.8, and (if required) by connecting small series reactances or shunt susceptances to its four ports.In this case, L_{tp} = 0.177845 nH, the odd-mode inductance L_{op1} = 0.3807 nH, and the even-mode parasitic capacitance C_{ep2} = 6.63666 fF.

These parasitics have to be previously determined, for the intended utilization band—since they need not be constant with frequency, by curve fitting with a test circuit and then, if necessary, the inverter has to be fine tuned (using its circuit model) to maintain its performance. For the circuit simulation of Fig. 2.7, the values of the parasitics where determined to obtain an overall agreement up to 20 GHz.

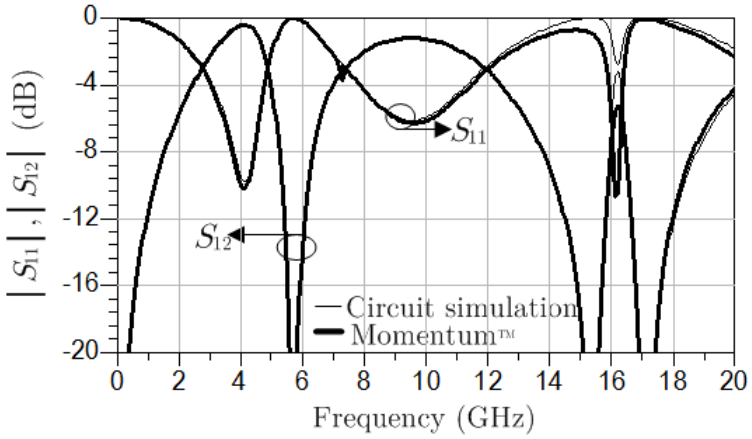

Figure 2.7 – Comparison between electromagnetic and equivalent-circuit simulations for the inverter of Fig. 2.5.

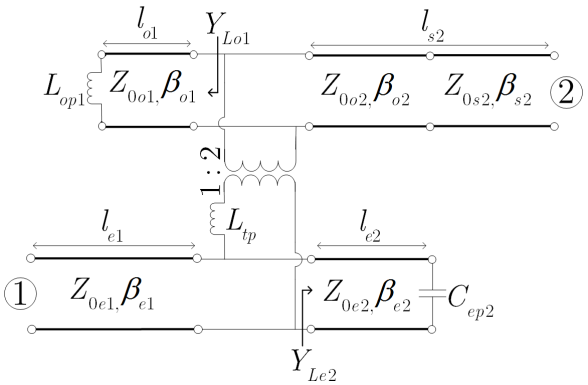

Figure 2.8 – Circuit model for the multimodal immitance inverter of Fig. 2.5, including parasitic elements.

2.1.3 Quarter-wavelength band-stop resonator

A structure similar to that of Fig. 2.5 can be used as a band-stop resonator, since a single even-mode stub can be used to produce a transmission zero. Fig. 2.9 shows its multimodal structure.

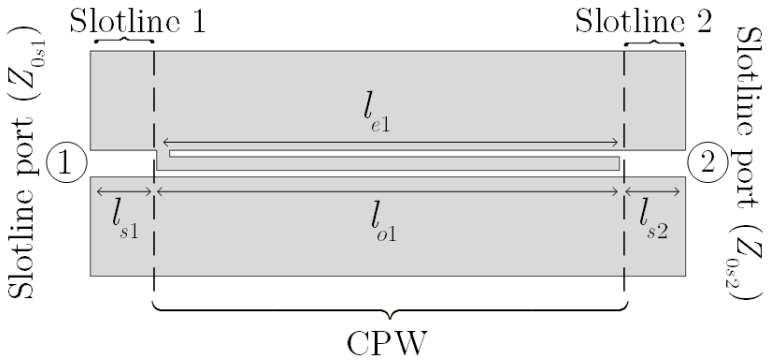

Figure 2.9 – Proposed quarter-wavelength band-stop resonator.

Here, the input and output ports are slotlines, with a central CPW section with an asymmetric short circuit at one end. When a slotline mode wave coming from any of the circuit ports arrives at the asymmetric short circuit, outward-propagating even and odd-mode waves are generated. The odd-mode waves reach the ports of the circuit as reflected and transmitted odd-mode waves (since this mode is compatible with the slotline mode), whereas the even-mode waves are confined within the CPW section.

The multimodal circuit of the band-stop resonator is shown in Fig. 2.10, which is similar to a generic band-stop resonator [39, 40] . It is apparent that this resonator will produce a transmission zero at $f_0 = f_{zero} = v_{pe}/(4l_{e1})$, where v_{pe} is the even-mode propagation velocity.

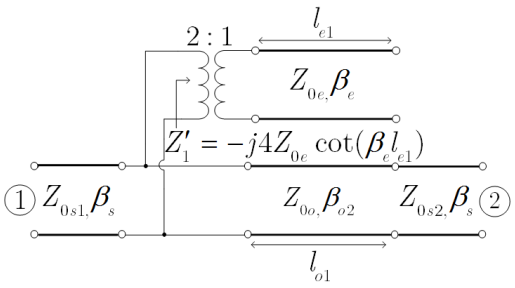

Figure 2.10 – Multimodal circuit of the quarter-wavelength band-stop resonator.

The input impedance Z_{0s1} is equal to the CPW odd-mode impedance, Z_{0o}. To design a resonator with a certain bandwidth the even-mode stub impedance can be calculated as

$$Z_{0e} = \frac{Z_M}{\alpha g_0 g_1}, \tag{2.16}$$

with

$$Z_M = \frac{Z_{0o}}{4} = \frac{Z_{0s1}}{4}. \tag{2.17}$$

The bandwidth parameter is $\alpha = \cot[(\pi/2)(1 - FBW/2)]$, the output impedance is $Z_{0s2} = Z_{0s1} g_2/g_0$; g_0,g_1 and g_2 are the normalized elements of a first-order low-pass filter prototype. Note that equation 2.16 was proposed in [39]; but for the multimodal resonator of Fig. 2.9, the impedance Z_M is equal to one quarter of the impedance of the odd-mode (2.17).

In order to validate the circuit model of Fig. 2.10, a band-stop resonator such as that of Fig. 2.9, with a central frequency f_0 and a $FBW = 0.225$ with a Butterworth response was designed. The chosen odd-mode impedance is $Z_{0o} = Z_{0s1} = 130\,\Omega$, which gives an even-mode impedance of $Z_{0e} = 91\,\Omega$. The parameters of the substrate are: relative permittivity $\varepsilon_r = 3.02$, thickness = 1.52 mm and metallization thickness = 0.035 mm. The CPW central-strip width is w =0.2 mm, with a slot width is $s = 0.1$ mm, and a slotline slot with $2s + w$, the lateral-ground-plane width is $w_g = 1$ mm, the eve-mode lenght is $l_{e1} = 25.7$ mm and the lenghts of the slotlines is $l_{s1} = l_{s2} = 0.8$ mm . An electromagnetic simulation of a resonator such as that of Fig. 2.9 was performed using Agilent Momentum, and compared with the results obtained with its circuit model. Fig. 2.11 compares the electromagnetic simulation of the circuit of Fig. 2.9 with the circuit-model of Fig. 2.10. The good agreement between both simulations validates the circuit model of Fig. 2.10.

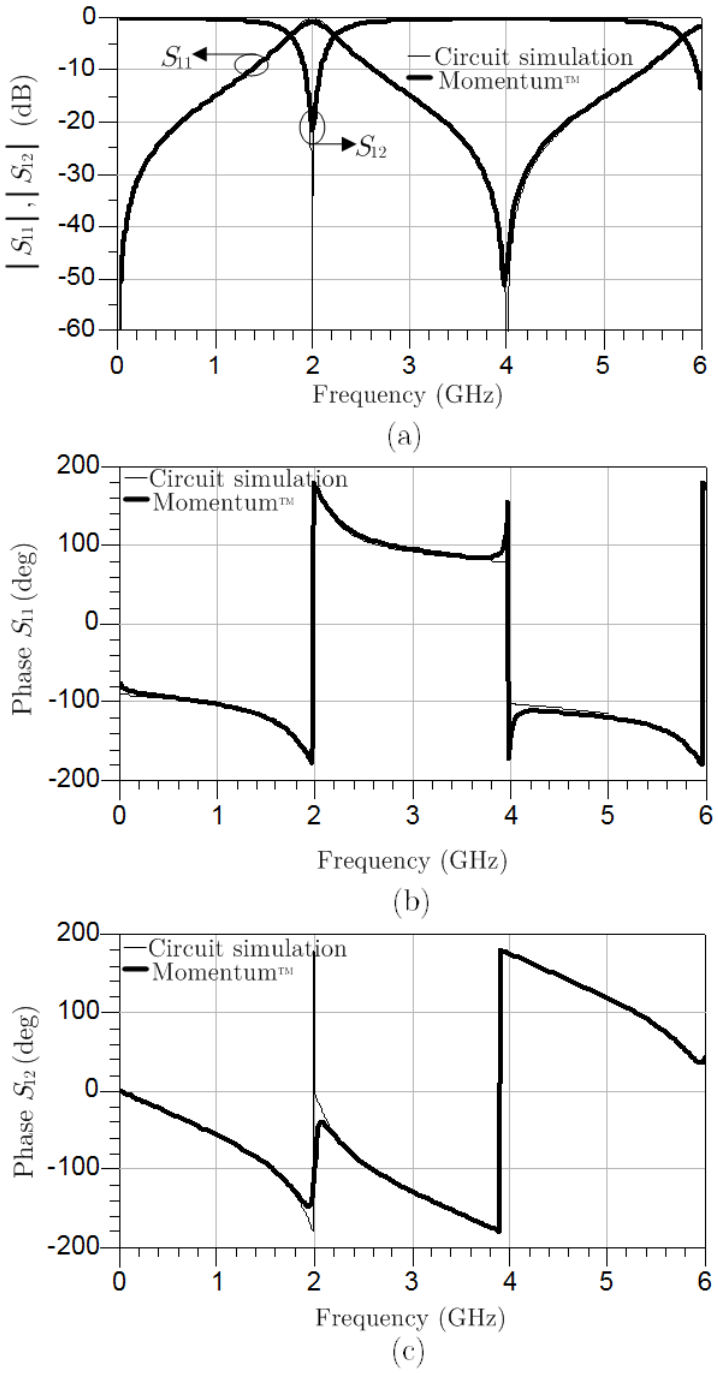

Figure 2.11 – Comparison between electromagnetic and equivalent-circuit simulations for the quarter-wavelength band-stop resonator of Fig. 2.9. (a) Magnitude of S_{11} and S_{12}. (b) Phase of S_{11}. (c) Phase of S_{12}.

2.2 CPW circuits with slotline-CPW tees

A slotline-CPW tee is a transition formed by the connection of a slotline to either of the slots of a CPW (Fig. 2.12 (a)). At the transition, a complex interaction between the slotline mode and the CPW even and odd modes takes place, which can be accurately modeled using a multimodal circuit model for coplanar-slotline tees [17]. This circuit model confines the contribution of either CPW mode into a different port and, therefore, can easily take into account situations where the CPW load behaves differently for either mode.

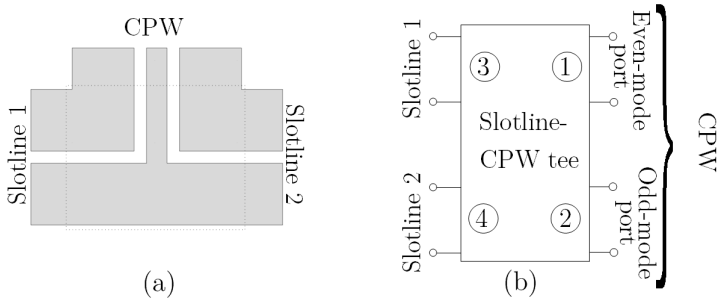

Figure 2.12 – A slotline-CPW tee (a) Topology (b) Multimodal circuit model.

Fig. 2.12 (b) shows the 4-port circuit model of the slotline-CPW transition, which corresponds to the S-parameters matrix [17]

$$S = \frac{1}{3}\begin{bmatrix} -1 & 0 & 2 & 2 \\ 0 & 1 & -2 & 2 \\ 2 & -2 & 0 & 1 \\ 2 & 2 & 1 & 0 \end{bmatrix}. \tag{2.18}$$

It should be noted that although it was derived initially for a CPW-slotline tee, this model is also valid for any other transmission-line-technology circuit where a coupled transmission line is connected to two other non-coupled transmission lines [17].

If the CPW-slotline tee is loaded with a symmetric CPW structure that presents a different response to either CPW mode, it can be modeled as shown in Fig. 2.13.

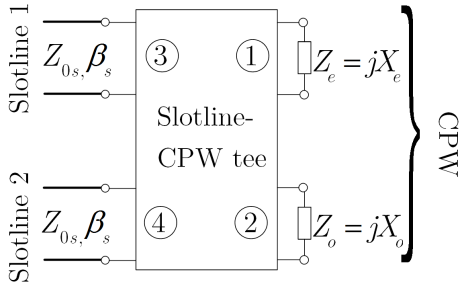

Figure 2.13 – A slotline-CPW tee multimodal circuit model with CPW even and odd mode loads.

The S parameters of the circuit of Fig. 2.13 can be computed as

$$S = -S_U e^{-j\varphi} \quad S_U = \begin{bmatrix} S_{11U} & S_{21U} \\ S_{21U} & S_{11U} \end{bmatrix}, \tag{2.19}$$

$$\text{with} \quad S_{11U} = \frac{1 + \bar{X}_e \bar{X}_o}{\sqrt{1+4\bar{X}_e^2}\sqrt{1+\frac{\bar{X}_o^2}{4}}}, S_{21U} = \frac{-j\left(2\bar{X}_e - \frac{\bar{X}_o}{2}\right)}{\sqrt{1+4\bar{X}_e^2}\sqrt{1+\frac{\bar{X}_o^2}{4}}}$$

$$\text{and} \quad \varphi = \arctan(2\bar{X}_e) - \arctan(\bar{X}_o/2),$$

where all reactances have been normalized to the slotline characteristic impedance Z_{0s}.

Fig. 2.14(a) and Fig. 2.14(b) show examples of symmetric loads of slotline-CPW tee, and Fig. 2.14(c) shows their multimodal circuit model.

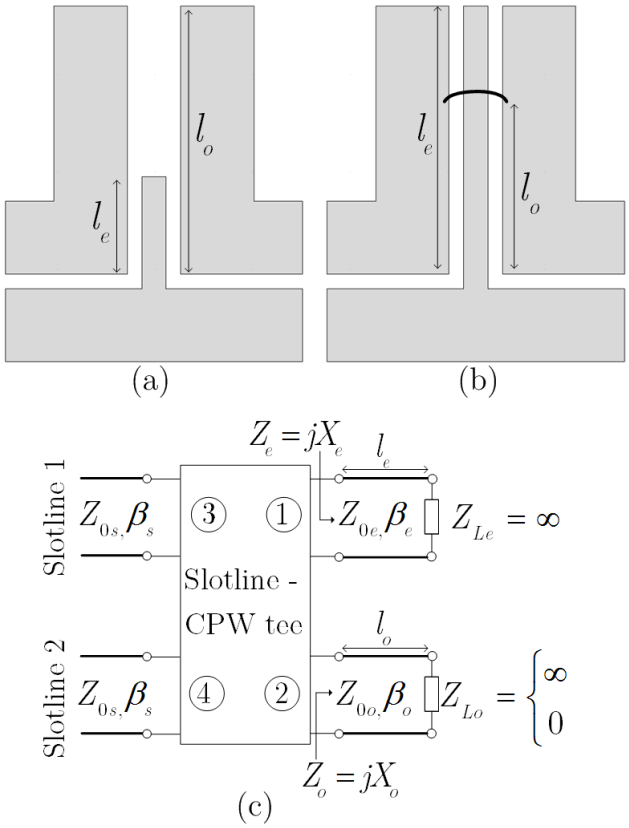

Figure 2.14 – Slotline-CPW tees loaded with symmetric CPW structures. (a) CPW odd mode section longer than that of the CPW even mode,($l_o > l_e$), both modes terminated with an open circuit ($Z_{Le} = Z_{Lo} = \infty$). (b) CPW even mode section longer than that of the CPW odd mode ($l_e > l_o$) , even mode terminated with an open circuit and odd mode terminated with a short-circuit ($Z_{Le} = \infty, Z_{Lo} = 0$). (c) Multimodal circuit model for CPW symmetric loads for case (a) and (b).

A slotline-CPW tee can be used to reduce the length of a slotline section or as an immittance inverter. These two applications are described in the following subsections.

2.2.1 Slotline-CPW tee for length reduction

The length l of a slotline section (Fig. 2.15 (a)) can be reduced by bending it (Fig. 2.15 (b)) . To achieve a strong length reduction, the slotline-bend sections have to be placed very close. In this case the bend no longer behaves as a slotline section of length l, but as a CPW section. In fact, the structure of Fig. 2.15 (b) is a loaded CPW-slotline tee, whose behavior is described by the multimodal circuit model of Fig. 2.14 (c) with $l_e = l_o$,$Z_{Le} \to \infty$ and $Z_{Lo} = 0$.

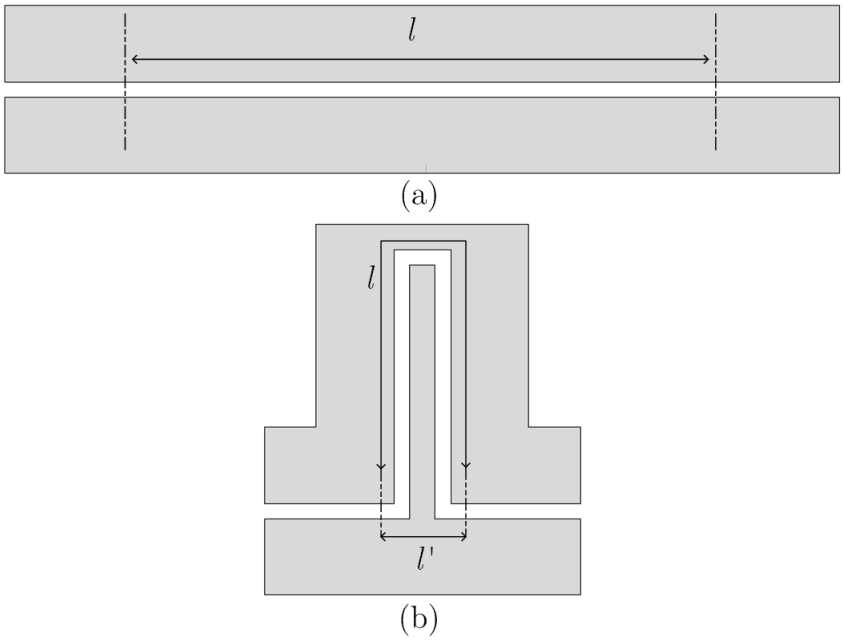

Figure 2.15 – (a) Slotline section of characteristic impedance Z_{0s} and electrical length $\beta_s l$. (b) Bended slotline section forming a CPW.

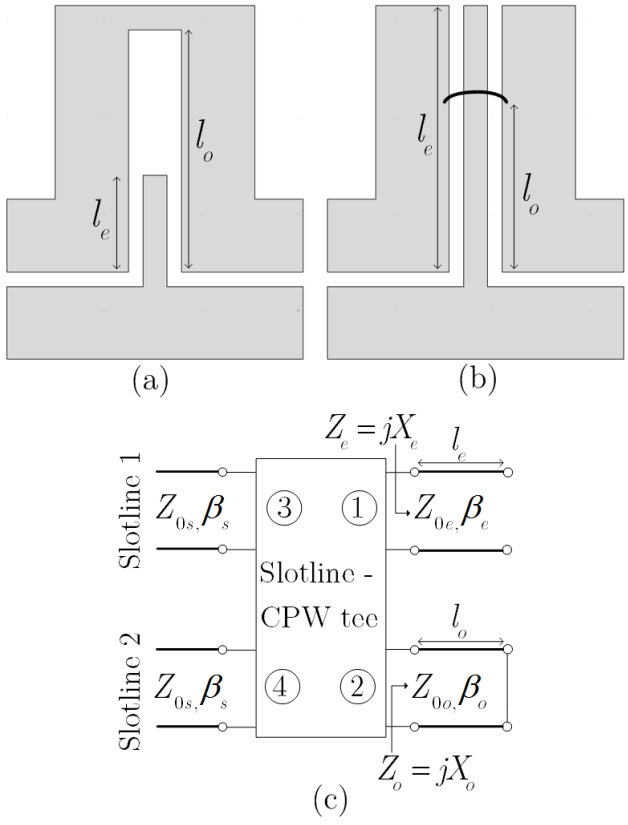

Figure 2.16 – Reduced-length slotline equivalents. (a) Reduced-length slotline equivalent with $l_o > l_e$. (b) Reduced-length slotline equivalent with $l_e > l_o$. (c) Equivalent multimodal circuit model.

The slotline-CPW tees of Fig. 2.16(a)–(b) can be designed to emulate a slotline section of length l. Indeed, if $\bar{X}_e\bar{X}_o = -1$ then 2.19 reduces to

$$S = \begin{bmatrix} 0 & 1 \\ 1 & 0 \end{bmatrix} e^{-j\phi} \tag{2.20}$$

where $\phi = \pi + 2\arctan(2\bar{X}_e)$.

Equation 2.20 corresponds to the S parameters of a slotline of characteristic impedance Z_{0s} and electrical length $\beta_s l = \pi + 2\arctan(2\bar{X}_e)$, with reference impedances Z_{0s} at both its ports.

The values $\bar{X}_e$ of $\bar{X}_o$ and can be adjusted in an independent way provided that the CPW-slotline tee is loaded as in the circuits of Fig. 2.16(a)–(b), whose multimodal circuit model is shown in Fig. 2.16(c). In Fig. 2.16(a), the even mode is open circuited at the end of the CPW central strip. There, the odd mode is transformed into a slotline mode (with a very similar characteristic impedance and phase constant due to their modal compatibility) and propagates until it is short circuited at the top of the structure. In Fig. 2.16(b), the odd mode is short circuited by the air bridge, and does not propagate further, whereas the even mode is not affected by it, and propagates until it is open circuited at the top of the structure. Therefore, using either the structure of Fig. 2.16(a) or Fig. 2.16(b), any value of l_e and l_o (and, therefore, of $X_e = -Z_{0e}\cot(\beta_e l_e)$ and $X_o = Z_{0o}\tan(\beta_o l_o)$ can be obtained.

Design expressions for l_e and l_o can be obtained as follows:

$$\frac{\beta_s l}{2} = -\frac{\pi}{2} + \arctan(2\bar{X}_e) \Rightarrow$$

$$\tan\left(\frac{\beta_s l}{2}\right) = -\frac{1}{2\bar{X}_e} \Rightarrow$$

$$\bar{X}_e = -\frac{1}{2}\cot\left(\frac{\beta_s l}{2}\right) \quad , \quad \bar{X}_o = 2\tan\left(\frac{\beta_s l}{2}\right) \tag{2.21}$$

From 2.21, l_e and l_o can be derived as

$$l_e = \frac{1}{\beta_e}\arctan\left(\frac{2Z_{0e}}{Z_{0s}}\tan\left(\frac{\beta_s l}{2}\right)\right), \tag{2.22}$$

$$l_o = \frac{1}{\beta_o}\arctan\left(\frac{2Z_{0s}}{Z_{0o}}\tan\left(\frac{\beta_s l}{2}\right)\right). \tag{2.23}$$

To validate the circuit model of Fig. 2.16(c), an electromagnetic simulation of a reduced-length slotline section such as that of Fig. 2.15(b) was performed, and compared with the results obtained with its circuit model. The parameters of the structure are: substrate relative permittivity $\varepsilon_R = 3.02$, substrate thickness = 1.52 mm; CPW central-strip width $w = 0.2$ mm and slot with $s = 0.1$ mm; slotline slot with= $2s + w$; input slotline width $ws = 1$ mm, and CPW section ground plane width $w_g = 0.65$ mm. For a given insertion phase of 14° at $f_0 = 2$ GHz, the calculated dimensions of the CPW section are $l_e = 3$ mm and $l_o = 3.1$ mm . The length of the input and output slotlines are $l_s = 1$ mm . The total insertion phase of the structure is 21° (14° for the insertion phase of the transition, plus 3.5° for each slotline).

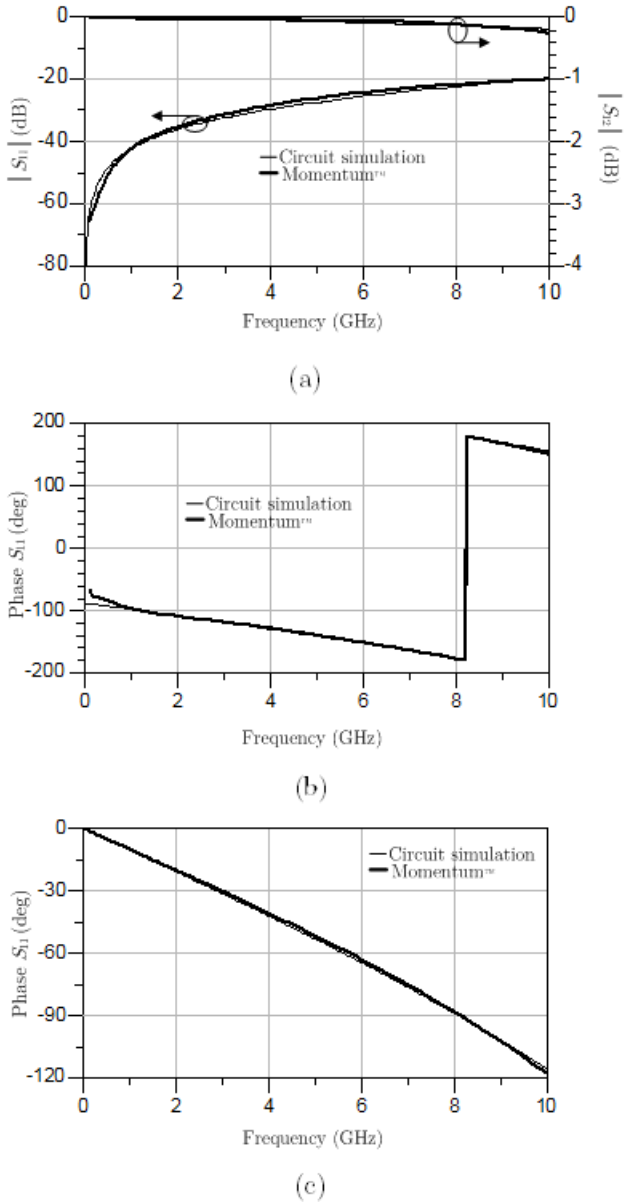

Figure 2.17 – Comparison between electromagnetic and equivalent-circuit simulations for the reduced-length slotline section of Fig. 2.15(b).

2.2.1.1 A Practical example: an uniplanar delay line

In order to validate the proposed structure, a test circuit has been fabricated in a Rogers RO4003C substrate, with a relative permittivity ε_R = 3.55 and thickness h = 1.52 mm. The test circuit shown in Fig. 2.18 includes 2 pairs of cascaded slotline-CPW tees (for a total a 4 transitions), separated by one slotline. The calculated lengths, at f_0 = 1.5 GHz, of each CPW section are l_e = 4 mm and l_o = 4.1 mm, which represent an insertion phase of 15° per transition, for a total of 60° (including all 4 transitions). The input and output slotlines (all slotlines have a slot width s_s = 0.2 mm and strip width w_s = 1.1875 mm) have been placed to avoid any influence of the SG/GS probes over the tees. The total length of the test structure of Fig. 2.18 is l_t = 17.65 mm.

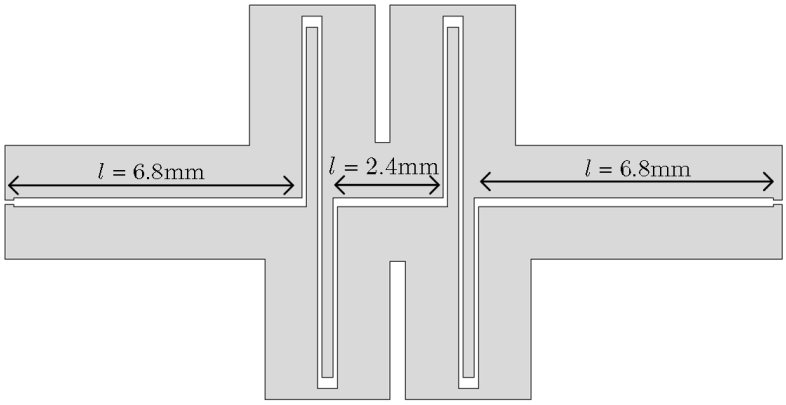

Figure 2.18 – Test structure: 2 pairs of cascaded slotline-CPW tees between slotlines.

A comparison between the equivalent-circuit simulation and the measured data of the test structure structure of Fig. 2.18 is shown in Fig. 2.19. At 1.5 GHz, the measured insertion phase of the whole structure is 98°. A simple slotline (fabricated in the same substrate and with the same dimensions of the ones used in the test structure) needs a total length of l_t = 35.1 mm to achieve the same phase shift. Thus, the length has been reduced by 50%.

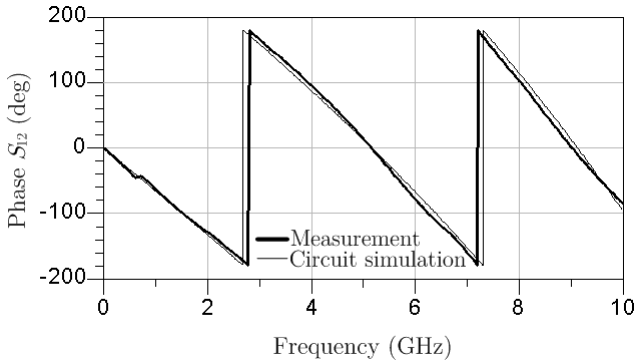

Figure 2.19 – Phase insertion comparison between measurement and the equivalent-circuit simulation of the test structure of Fig. 2.18.

2.2.2 Slotline-CPW tee as immittance inverter

An immitance inverter has an S-parameter matrix with $S_{11} = S_{22}$ real. Therefore 2.19 can also be interpreted as the S-parameter matrix of an immitance inverter with equal-length slotline sections (of characteristic impedance Z_{0s}) connected to its ports (Fig. 2.20). In order to establish a relationship between the generic parameters (X_e and X_o) of the circuit of Fig. 2.12 (a) and those of the circuit of Fig. 2.20, the S-parameters of the later have to be computed. If the immitance inverter of Fig. 2.20 is characterized by its Z-parameter matrix

$$Z = \begin{bmatrix} 0 & jX \\ jX & 0 \end{bmatrix} \qquad K = |X| \tag{2.24}$$

where K is the inverter constant, then the S-parameters of the circuit of Fig. 2.20 are

$$\begin{aligned} S &= S_{INV} e^{-j2\beta_s l} \\ S_{INV} &= \frac{1}{X^2+Z_{0s}^2} \begin{bmatrix} X^2 - Z_{0s}^2 & j2Z_{0s}X \\ j2Z_{0s}X & X^2 - Z_{0s}^2 \end{bmatrix}, \end{aligned} \tag{2.25}$$

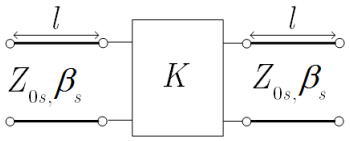

Figure 2.20 – Immitance inverter with two equal-length slotlines connected at its ports.

By comparing (2.19) and (2.25), three different equivalences between circuits such as those of Fig. 2.12 (a) and that of Fig. 2.20 can be found, namely

$$\begin{aligned} S_{INVA} &= -S_U \qquad 2\beta_s l_A = \varphi \\ S_{INVB+} &= S_U \qquad 2\beta_s l_{B+} = +\pi + \varphi \\ S_{INVB-} &= S_U \qquad 2\beta_s l_{B-} = -\pi + \varphi \end{aligned}$$

where subindexes $A, B+$ and $B-$ have been added to identify them. The previous equivalences cannot be analytically solved for $\bar{X}_e$ and $\bar{X}_o$ (and thus for the physical parameters of the loaded CPW-sloltine tees l_e and l_o) as a function of the desired value of X. However, they can be easily solved for X, and $\bar{X}_e$,$\bar{X}_o$ and $\beta_s l$ can then be found by graphical means.

The first solution (corresponding to $S_{INVA} = -S_U$ and $2\beta_s l_A = \varphi$) is

$$\begin{aligned} \bar{X}_A &= \operatorname{sgn}\left(2\bar{X}_e - \frac{\bar{X}_o}{2}\right) \sqrt{\frac{\sqrt{1+4\bar{X}_e^2}\sqrt{1+\frac{\bar{X}_o^2}{4}} - (1+\bar{X}_e\bar{X}_o)}{\sqrt{1+4\bar{X}_e^2}\sqrt{1+\frac{\bar{X}_o^2}{4}} + (1+\bar{X}_e\bar{X}_o)}}, \\ \beta_s l_A &= \tfrac{1}{2}\left[\arctan(2\bar{X}_e) - \arctan(\bar{X}_o/2)\right], \end{aligned} \tag{2.26}$$

where sgn(x) is the sign function and all reactances are normalized to Z_{0S}. The information about $\bar{X}_A$ and $\beta_s l_A$ can be easily represented in a contour plot as a function of $\bar{X}_e$ and $\bar{X}_o$ (Fig. 2.21 and Fig. 2.22). To design a loaded CPW-slotline tee as an immitance inverter, from $\bar{X}_A$, sets of adequate values of $\bar{X}_e$ and $\bar{X}_o$ have to be selected from Fig. 2.21 and, among them, which give the most appropriate value to $\beta_s l_A$ (for instance, a negative value in a filter design to reduce the physical length of the filter) from Fig. 2.22.

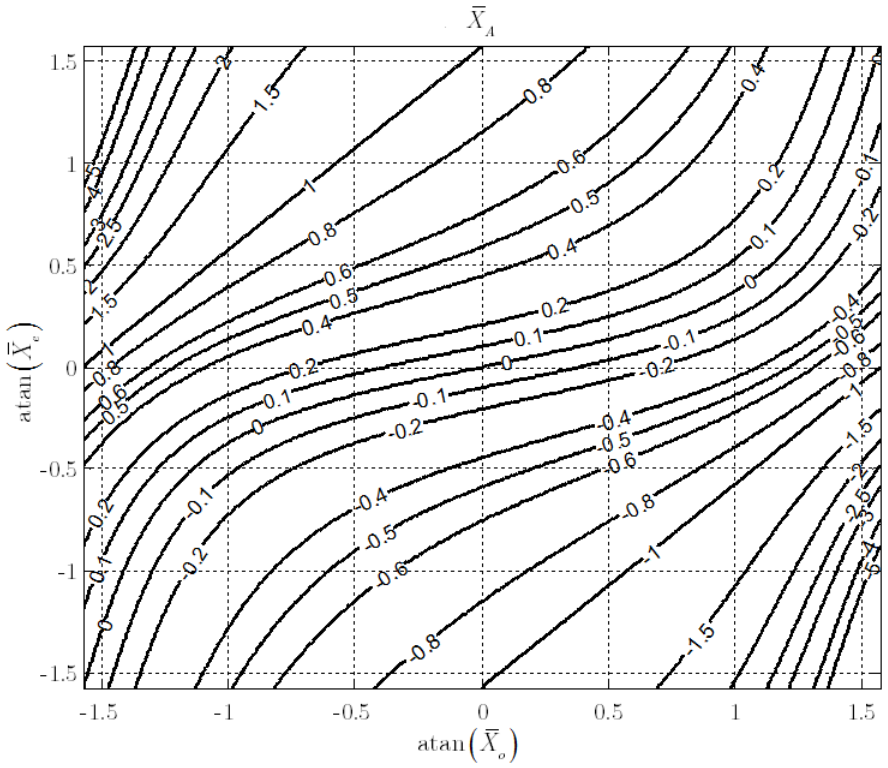

Figure 2.21 – $\bar{X}_A$ as a function of $\bar{X}_e$ and $\bar{X}_o$.

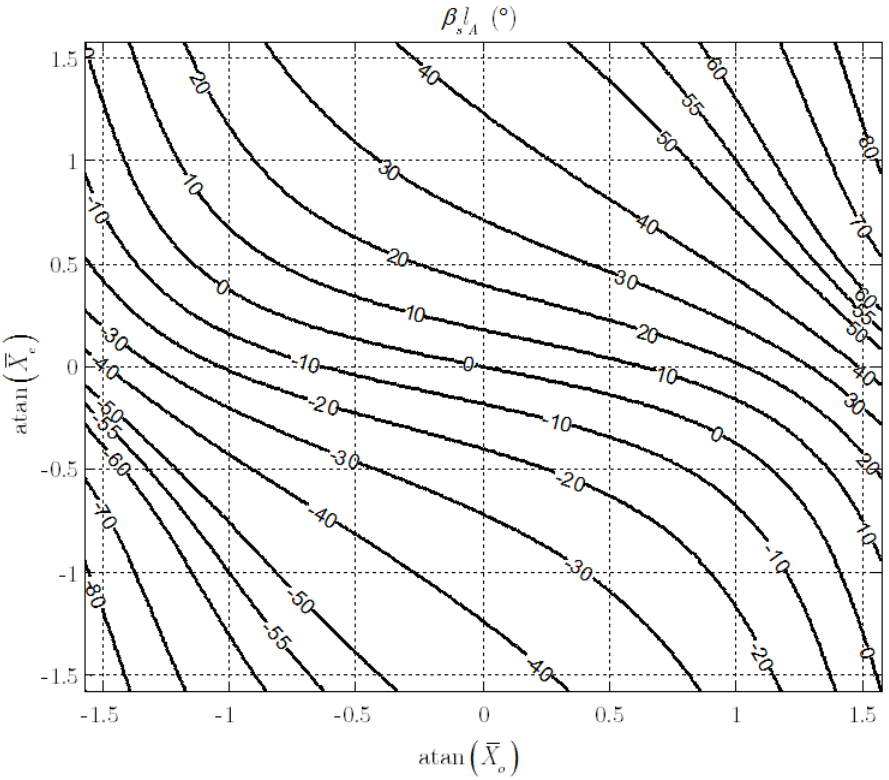

Figure 2.22 – $\beta_s l_A$ as a function of $\bar{X}_e$ and $\bar{X}_o$.

For convenience, these solutions can be overlapped in a single graph, as shown in Fig. 2.23.

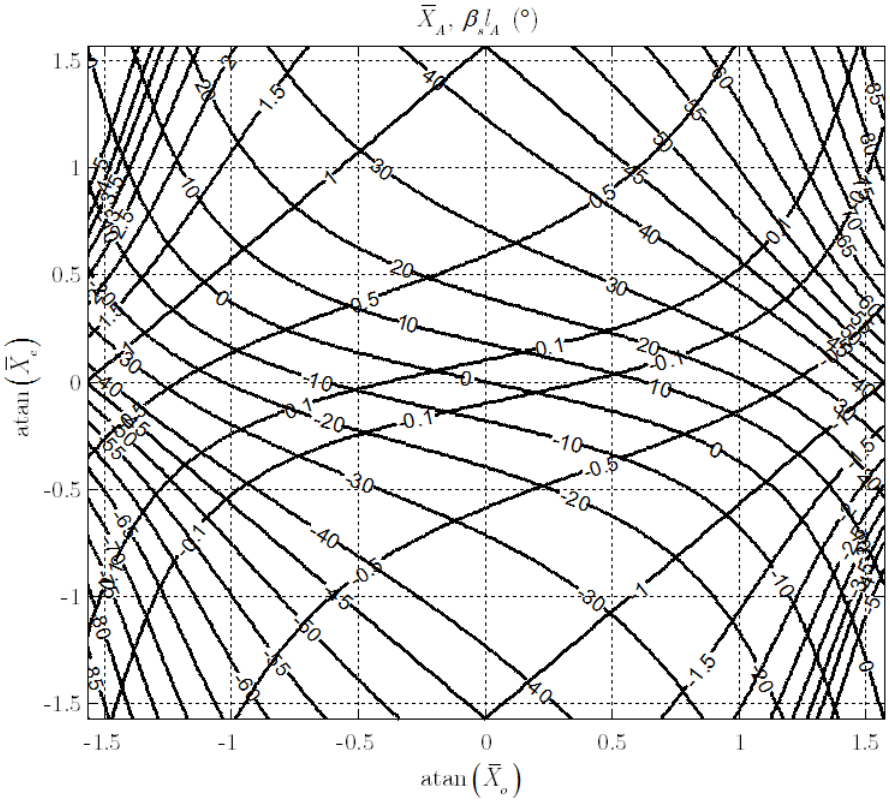

Figure 2.23 – $\bar{X}_A$ and $\beta_s l_A$ as a function of $\bar{X}_e$ and $\bar{X}_o$.

The second and third solutions (corresponding to $S_{INVB+} = S_U$, and $2\beta_s l_{B+} = \varphi+\pi$ and $2\beta_s l_{B-} = \varphi-\pi$ respectively) are

$$\begin{aligned} \bar{X}_{B+} &= \bar{X}_{B-} = -\tfrac{1}{\bar{X}_A} \\ \beta_s l_{B+} &= +\tfrac{\pi}{2} + \beta_s l_A \\ \beta_s l_{B+} &= -\tfrac{\pi}{2} + \beta_s l_A \,. \end{aligned} \tag{2.27}$$

These solutions can be treated graphically to design the desired immitance inverter in an analogous way to that of the first solution. It is apparent from (2.26) and (2.27) that the same values of $\bar{X}_e$ and $\bar{X}_o$ that give an impedance inverter in (2.26), give an admittance inverter in (2.27), and vice versa (if the slotline lengths are adequately chosen).

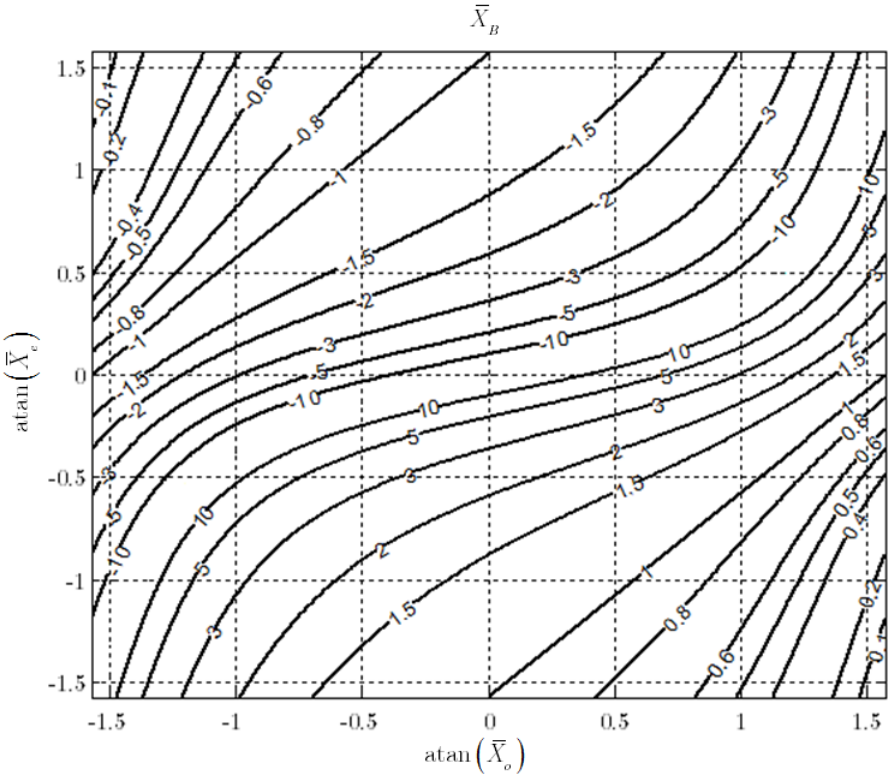

Figure 2.24 – $\bar{X}_B$ as a function of $\bar{X}_e$ and $\bar{X}_o$.

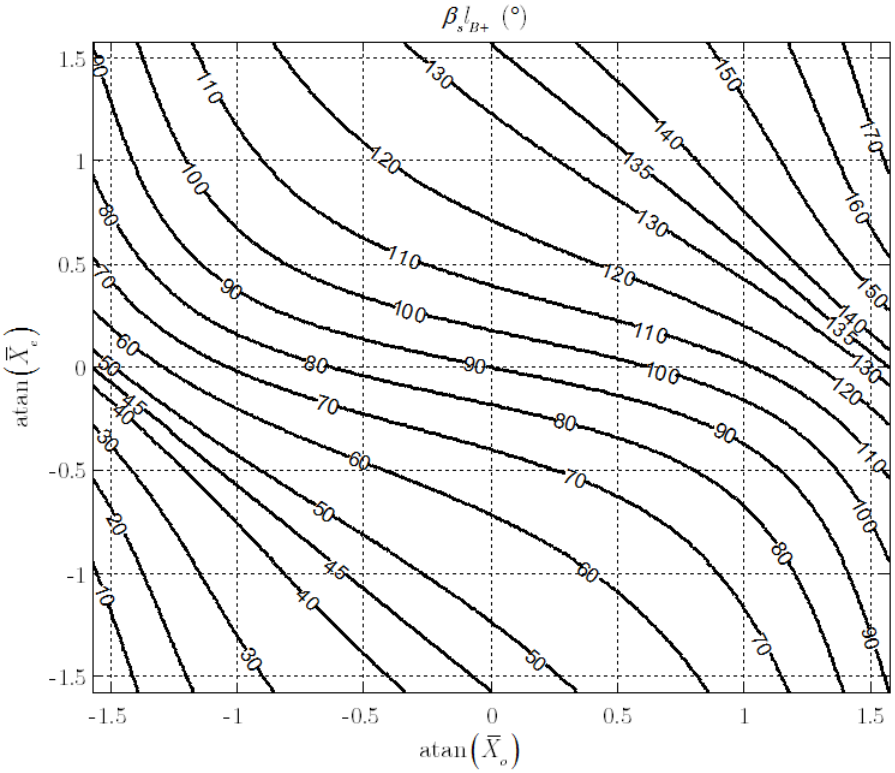

Figure 2.25 – $\beta_s l_{B+}$ as a function of $\bar{X}_e$ and $\bar{X}_o$.

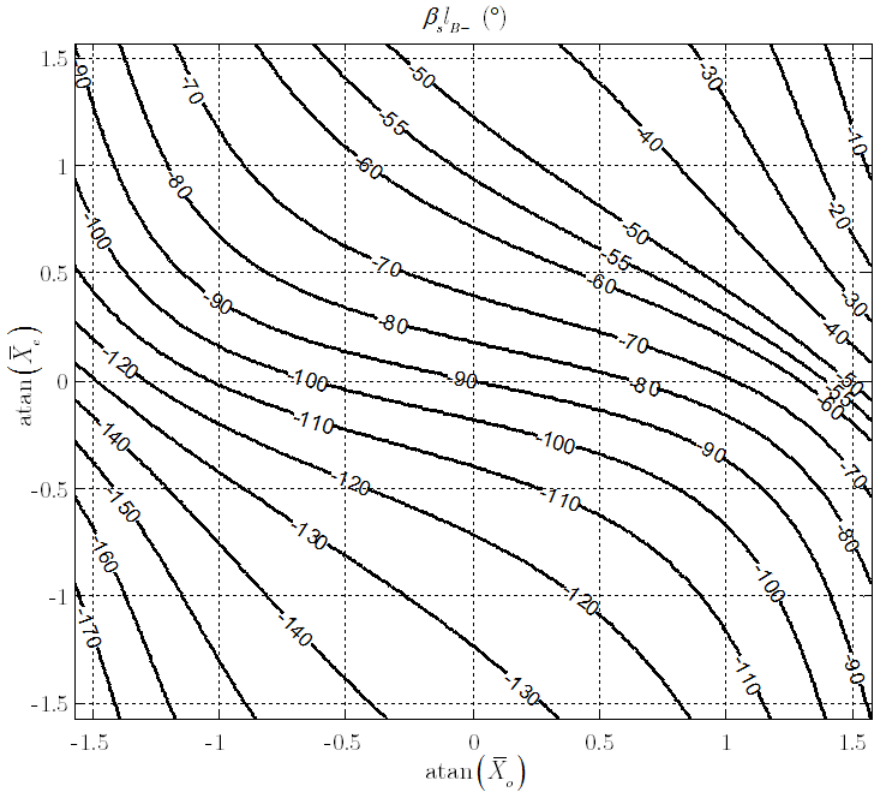

Figure 2.26 – $\beta_s l_{B-}$ as a function of $\bar{X}_e$ and $\bar{X}_o$.

2.3 CPW circuits with asymmetric series impedances

2.3.1 Band-stop resonator

Fig. 2.27 shows two topologies of multimodal band-stop resonators. These asymmetric structures are composed of a CPW section limited by air-bridges that contains a series slotline, terminated with a short-circuit or an open circuit.

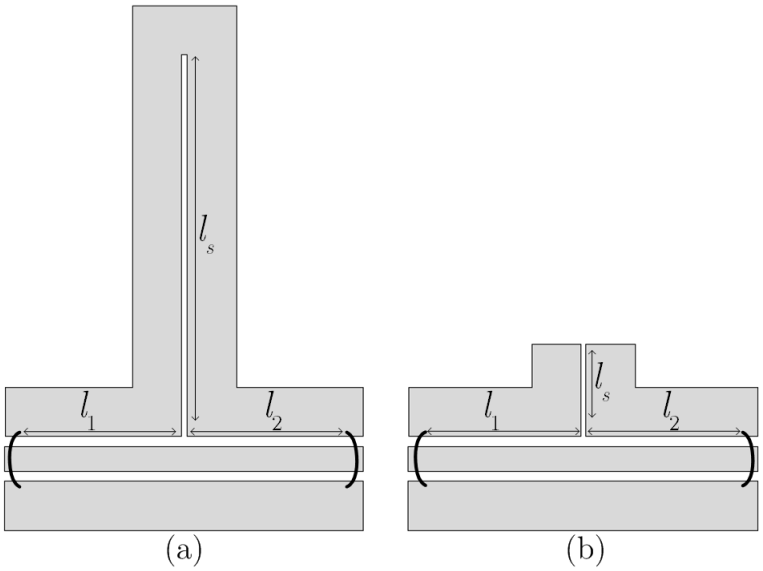

Figure 2.27 – Multimodal bandstop resonator. (a) With a short-circuited slotline stub. (b) With an open-circuited slotline stub.

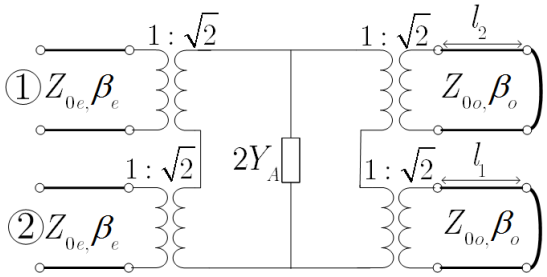

Figure 2.28 – Circuit model of the multimodal band-stop resonators of Fig. 2.27.

These structures can be modeled using the multimodal circuit model for asymmetric series-impedances in CPWs [15] as shown in Fig. 2.28, where $\beta_e, Z_{0e}, \beta_o, Z_{0o}$, are the propagation constants and the characteristic impedances of the even and odd modes, respectively. Y_A is the input admittance of the slotline stub given by $Y_A = 1/Z_s$. For an open-circuited stub $Z_s = -jZ_{0s}\cot(\beta_s l_s)$ and for a short-circuited one, $Z_s = jZ_{0s}\tan(\beta_s l_s)$.

The multimodal circuit model of Fig. 2.28 can be viewed as a series parallel-resonant branch, in which the slotline stub provides the capacitive element and the short-circuited odd-mode CPW stubs provide the inductive element.

The whole resonant structure can be modeled by an impedance Z_T connected to the even-mode transmission line (Fig. 2.29(a)) of value

$$Z_T = \frac{1}{\frac{2}{j(Z_{0o}/2)\left[\tan(\beta_o l_{o1})+\tan(\beta_o l_{o2})\right]} + \frac{4}{Z_s}}. \tag{2.28}$$

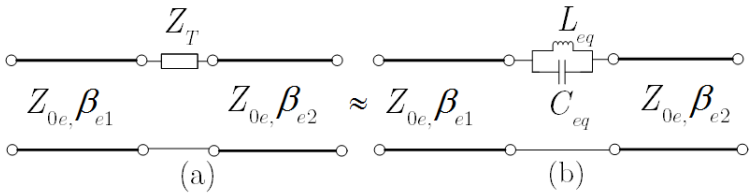

Figure 2.29 – Comparison between (a) a simplification of the circuit model of Fig. 2.28 and (b) a series-parallel LC resonator.

The impedance of series parallel-resonant branch (Fig. 2.29(b)) is

$$Z_{eq} = \frac{1}{(1/j\omega_0 L_{eq}) + j\omega_0 C_{eq}}, \tag{2.29}$$

Comparing 2.28 and 2.29, and assuming that $l_{o1} = l_{o2} = l_o$ and that $\beta_o l_o < \pi/4$, the following equivalence can be found

$$L_{eq} = Z_{0o}\tan(\beta_o l_o)/(2\omega_0). \tag{2.30}$$

Given that $\omega_0 C_{eq} = 1/\omega_0 L_{eq}$, the susceptance slope for the circuit is

$$\omega_0 C_{eq} = \frac{2}{Z_{0o}\tan(\beta_o l_o)} = \frac{4}{Z_{0s}\cot(\beta_s l_s)}, (\text{open} - \text{circuit slotline stub}), \tag{2.31}$$

$$\omega_0 C_{eq} = \frac{2}{Z_{0o}\tan(\beta_o l_o)} = \frac{-4}{Z_{0s}\tan(\beta_s l_s)}, (\text{short} - \text{circuited slotline stub}). \tag{2.32}$$

Thus, by calculating the equivalent inductance and capacitance of an ideal series parallel-resonant branch for a required bandwidth, the electrical lengths $\beta_o l_o$ and $\beta_s l_s$ can be found. For filters of n order

$$\left(\frac{Y_U}{Y_0}\right)^2 = g_0 g_{n+1}, \tag{2.33}$$

and the susceptance slope of series-parallel resonators is given by [41]

$$b_i = \omega_0 C_i = 1/\omega_0 L_i = Y_0 \left(\frac{Y_U}{Y_0}\right)^2 \frac{g_0}{g_i \Omega_c FBW} \text{for} i = 1\ to\ n, \tag{2.34}$$

where Y_0 is the terminating admittance and Y_U is the admittance of the immittance inverters placed between two series-parallel resonant branches (in this case $Y_0 = 1/Z_{0e} = Y_{0e}$).

CHAPTER 3

RF-MEMS AND THEIR APPLICATIONS IN MULTIMODAL CIRCUITS

In comparison with active devices, electrostatic RF-MEMS switches have proved their superior performance in terms of losses, linearity and power consumption [42]. During the last two decades, researchers have developed tunable and reconfigurable circuits based on RF-MEMS, achieving state-of-the-art performances. One of the advantages of electrostatic actuation is that there is no current consumption. Its drawback is that the required pull-in voltage V_{pi} for RF-MEMS electrostatic switches is high, usually from 30 V to 120 V. This depends mainly on the area of the electrodes (which is proportional to the electrostatic force, F_e), and the stiffness of the suspension or spring constant (k). The relationship between these two parameters will be explained in this chapter.

On the other hand, uniplanar circuits (such as CPW, CPS or slotlines) are ideal technologies for implementing tunable and reconfigurable circuits using RF-MEMS. Among these, CPW multimodal circuits can be easily reconfigured using these devices, as already demonstrated in [21].

This chapter introduces basic concepts of RF-MEMS and presents new low-actuation-voltage switches, which are developed to be used in some of the uniplanar multimodal reconfigurable filters presented in Chapter 5. In particular, this section presents a new shunt-type ohmic contact RF-MEMS switch specifically designed as a switchable CPW air bridge. The switch can be used in CPW reconfigurable multimodal circuits, for a selective use of the CPW odd-mode.

3.1 RF-MEMS electrostatic switches

3.1.1 Electrostatic actuation

A RF-MEMS electrostatic switch, as shown in Fig. 3.1, is in essence a micro-machined capacitor with a moving top electrode. The components behave like a mass-spring system, actuated by an electrostatic force F_e. The electrostatic force F_e is produced by applying a voltage V between the two electrodes.

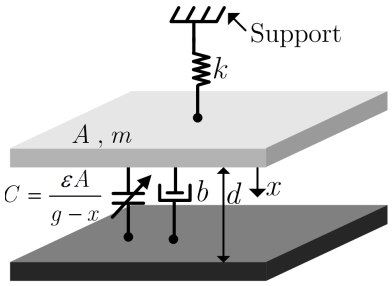

Figure 3.1 – Electromechanical model of an electrostatically-actuated parallel-plate switch (voltage mode) [3, 4].Top plate (light grey) is mobile and bottom plate (dark grey) is fixed.

Assuming the area of the plates is much greather than the separation between them (ignoring the fringing capacitance), the two-parallel-plate structure of Fig. 3.1, has a capacitance given by

$$C = \frac{\varepsilon A}{d - x}, \tag{3.1}$$

where ε is the the dielectric permittivity of the medium between plates (presumed to equal that of free space), A is the plate area, d the initial gap and x is the displacement of the top plate. If a voltage V is applied to the parallel-plate capacitor there will be a electrostatic potential energy

$$U = \frac{1}{2} C V^2, \tag{3.2}$$

which is stored between the volume of the plates.

For the constant voltage case [3, 43], the electrostatic force F_e can be defined as

$$F_e = -\frac{\partial U^*}{\partial x}\bigg|_{V\,ct} \tag{3.3}$$

where U^* is the co-energy. For two-parallel-plate structures –characterized by a capacity, C–, the energy and the co-energy are equivalent.

By substituting (3.2) into (3.3), the electrostatic force in a two-parallel-plate structure like the one shown in Fig. 3.1, is defined by

$$F_e = -\frac{1}{2} \frac{\varepsilon A V^2}{(d - x)^2}. \tag{3.4}$$

The electrostatic force is balanced by the mechanical restoring force which is given by Hooke's law (assuming one degree of freedom):

$$F_R = kx \tag{3.5}$$

where k is the total stiffness (spring) constant. The mobile top plate can be moved by applying a voltage V, but an equilibrium solution is not always achieved, and when this applied voltage V surpasses the pull-in voltage V_{pi}, a collapse of the mobile plate happens, as the mechanical force can no longer balance the electrostatic force. Neglecting the dynamics of the system, the pull-in occurs when the mobile plate has gone through one third of the initial gap d ($x = x_{pi} = d/3$), for an actuation voltage [3, 44]

$$V = V_{pi} = \sqrt{\frac{8kd^3}{27\varepsilon A}}. \tag{3.6}$$

Equation (3.6) is valid for switches without dielectric insulator between electrodes. For capacitive switches, the thickness of the dielectric insulator t_d can be taken into account using the following expression [42]:

$$V_{pi} = \sqrt{\frac{8k(d + (t_d/\varepsilon_r))^3}{27\varepsilon A}}, \tag{3.7}$$

where ε_r is the permittivity of the dielectric of the dielectric insulator. As mentioned before, the pull-in voltage V_{pi} depends mainly on the area of the electrodes, the stiffness of the suspension or spring constant (k), and the initial gap d.

On the other hand, the hold-down voltage (V_h) of a capacitive switch (the voltage required to maintain the switch in the down-state), is given by [42]:

$$V_h = \sqrt{\frac{2k}{\eta\varepsilon A}(d - x)\left(d + \left(\frac{t_d}{\varepsilon_r}\right)\right)^2}, \tag{3.8}$$

whereη accounts for the reduction in the parallel-plate capacitance due to the roughness of the metal-to-dielectric interface [42].

The switching time can be calculated as [42]

$$t_s = 3.67\frac{V_{pi}}{V\omega_0} = 3.67\frac{V_{pi}}{V\sqrt{k/m}},$$

where m is the mass of the moving electrode and V is the applied bias voltage.

3.1.1.1 Dynamics of MEMS devices using electrostatic actuation

The dynamics of motion of a suspended membrane in an electrostatically-actuated parallel-plate configuration can be approximated by the non-linear differential equation of a mass-spring-damper system (1-D model) [3]

$$m\frac{d^2x}{dt^2} + b\frac{dx}{dt} + kx = F_e = \frac{1}{2}\frac{\varepsilon AV^2}{(d - x)^2}, \tag{3.9}$$

where b is the damping coefficient.

The system's transfer function and frequency response can be obtained, by applying the Laplace transform to (3.9), as

$$\frac{X(s)}{F_e(s)} = \frac{1}{m}\frac{1}{s^2 + s\frac{b}{m} + \frac{k}{m}}, \tag{3.10}$$

$$s = j\omega, \therefore \frac{X(j\omega)}{F_e(j\omega)} = \frac{1}{k} \frac{1}{1 - \left(\frac{\omega}{\omega_0}\right)^2 + j\frac{\omega}{Q_m \omega_0}}, \tag{3.11}$$

where the mechanical resonance angular frequency ω_0 and the mechanical quality factor Q_m are defined as

$$\omega_0 = \sqrt{k/m} \tag{3.12}$$

$$Q_m = \frac{\sqrt{km}}{b} = \frac{k}{\omega_0 b} = \frac{1}{2\zeta} \tag{3.13}$$

where ζ is the relative damping factor.

3.1.1.2 Effects on MEMS switches under medium to high-power conditions

Self-biasing, self-actuation, RF power latching and heating are common effects in MEMS switches under medium to high-power conditions. Each concept will be defined in this section.

Self-biasing:

Self-biasing is the attractive force due to the RF signal rms voltage (V_{RFrms}), causing the membrane (moving electrode) to deflect (or to change the initial gap between electrodes, d) . It should be noted that self-biasing is not the same as self-actuation, since the latter implies the collapse of the beam. For both cases, the total electrostatic force, F_{et}, can be expressed as

$$F_{et} = -\frac{1}{2}\frac{\partial C}{\partial x}\left(V_{DC}^2 + V_{RFrms}^2\right). \tag{3.14}$$

For shunt MEMS switches, the configuration shown in Fig. 3.2 can be considered, assuming that the switch is terminated at both ports and that the generator is well matched.

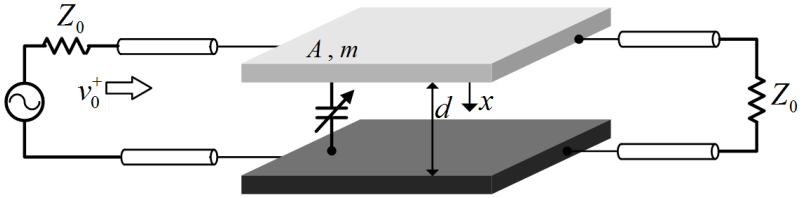

Figure 3.2 – Electrostatically-actuated RF-MEMS capacitive switch [3].

Then, the RF voltage amplitude at the switch is the incident wave amplitude $V_0 = |v_0^+|$, and can be related to the incident RF power $P_{RF(av)}$, by

$$P_{RF(av)} = \frac{V_{RFrms}^2}{Z_0} = \frac{V_0^2}{2Z_0}, \tag{3.15}$$

where Z_0 is the characteristic impedance of the transmission line. The total effective voltage applied to the membrane is

$$V = \sqrt{V_{DC}^2 + \frac{V_0^2}{2}} = \sqrt{V_{DC}^2 + P_{RF(av)} Z_0} \tag{3.16}$$

Thus, a new pull-in voltage $V_{DC,pi}$ can be obtained from (3.1) as

$$V_{DC,pi} = \sqrt{V_{pull-in}^2 - P_{RF(av)} Z_0}. \tag{3.17}$$

As shown by (3.17), the new pull-in voltage $V_{DC,pi}$ decreases as the $P_{RF(av)}$ increases. For high power values, the electrostatic force provided by $P_{RF(av)}$ may cause self-biasing. For example, an incident signal with a RF power of 2 W (assuming a characteristic impedance Z_0=50 Ω) , will produce a rms voltage of V_{RFrms} = 10 V.

From another point of view, and assuming that the membrane is in the up-state, and no power is reflected, the required power to actuate the switch is [45]

$$P_{act} = \frac{8kd^3}{27\varepsilon Z_0 A_{\mathrm{RF}}}, \tag{3.18}$$

where A_{RF} is the switch overlapping RF area.

Self-biasing can be avoided by using higher-stiffness constant suspensions or by reducing the capacitance between electrodes, at the expense of a higher actuation voltage. Another choice is to decouple the bias from the RF signal. As can be seen in (3.18), if the overlapping RF area is minimized, the switch will be less sensitive to high power levels.

RF power latching:

When the rms voltage related to the input power is equal or higher than the hold-down voltage V_h of the switch, the membrane is no longer able to assume its up-state position even without DC bias [45–47]. As demonstrated in [45], the RF power required to keep a switch in the down state (after the switch has been actuated) is less than the required for self-actuation. In the down-state, the switch characteristic impedance is not the same than the port impedance Z_0, therefore there will be a reflected voltage. In this case, the rms voltage is [45]

$$V_{RFrms} = \frac{|V_0|}{\sqrt{2}\sqrt{1 + \left(\pi f C_{down} Z_0\right)^2}}. \tag{3.19}$$

Depending on the electrical resonance frequency of the capacitive switch (hold-down power is higher at the frequency where the switch presents a better short-circuit [45]) , the necessary RF power to hold the switch is

$$P_h = \frac{2kd\left(d_{air} + t_d/\varepsilon_r\right)^2 \left[1 + \left(\pi f C_{down} Z_0\right)^2\right]}{A_{\mathrm{RF}} \varepsilon_0 Z_0}. \tag{3.20}$$

where d_{air} is the air-gap between electrodes in the down-state (typically less than 0.1 μm)

This demonstrates that the hold-down power is a function of the down-state capacitance. However, (3.18) and (3.20) do not take into account thermal issues, which could lead to additional stiction problems [45].

Thermal effects:

Another side effect of high RF power is heating. RF power induces a non-uniform current in the suspended membrane and its suspensions, producing a temperature rise, and therefore the materials tend to expand. In most cases the suspended membrane and suspensions loose rigidity, thus lowering the pull-in voltage. Thermal analyses for MEMS switches were published in [48–54].

3.1.2 FBK-irst RF-MEMS technology

The technology used for the fabrication of the devices presented in this chapter consists of an eight-mask surface micro-machining process, developed by the MEMS group of FBK [5]. Fig. 3.3 shows the fabrication process flow. First, an insulating layer consisting of 1μm of silicon oxide is grown by wet thermal oxidation.The DC -actuation pads, bias lines and contact bumps (dimples) are defined by using a high-resistivity polysilicon layer with a thickness of 0.63 μm. An insulating layer of 300 nm SiO_2 is deposited by LPCVD (low pressure chemical vapor deposition) using TEOS (tetraethyl orthosilicate). A second lithography step defines the opening for the contacts (Fig. 3.3a)). A multi-metal layer (Ti/TiN/Al/Ti/TiN) with the same thickness than polysilicon (0.63 μm, in order to avoid distortions in the bridge) is used as an "underpass" to connect signal lines under suspended structures. Then, a 100 nm thick SiO_2 dielectric layer (low temperature oxide, LTO) is deposited. The next lithography step defines the vias in the LTO. A 5-nm-Cr 150-nm-Au layer (Fig. 3.3c)) is deposited by electron beam gun to be used both as floating metal and to reduce the metal-Au resistance inside vias. This 150-nm layer defines metal-insulator-metal (MIM) capacitors or ohmic contacts. For the fabrication of suspended movable membranes and air bridges, different thicknesses of sacrificial layer (spacer) can been used, usually from 1.6 μm to 3 μm. Two gold layers of different thicknesses can be deposited (electroplated) to define transmission lines and suspended membranes. The movable bridges are manufactured using a 1.8-μm-thick gold layer (Fig. 3.3e) and a second 3.5-μm-thick superimposed gold layer (Fig. 3.3f) is used to increase the rigidity of selected parts of the membranes.

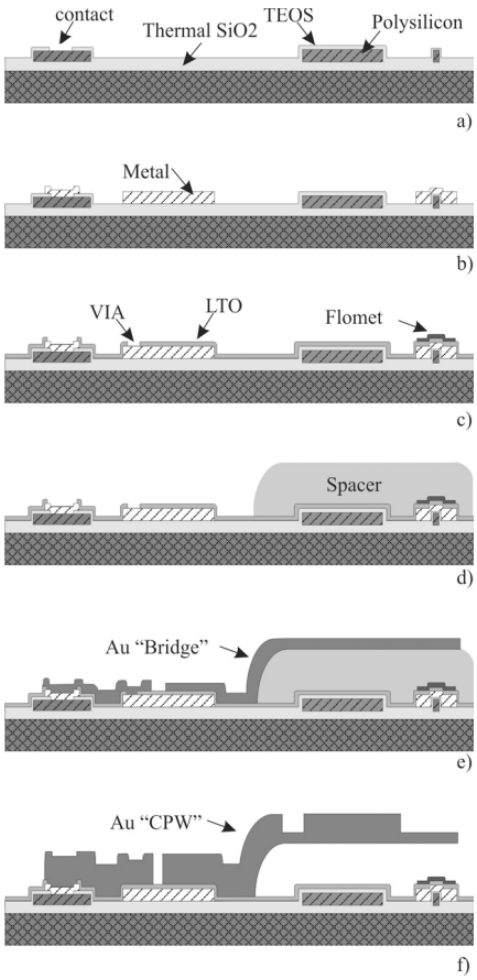

Figure 3.3 – Process flow. a) Thermal oxidation; polysilicon and TEOS deposition and contact opening. b) Metal deposition and patterning. c) LTO deposition, vias opening and floating metal deposition. d) Spacer deposition and backing. e) Seed layer and first Au "Bridge" electroplating. f) Second Au "CPW" electroplating and release of suspended structures. (Figure taken from [5]).

The advantages of this process are:

- RF and DC actuation pads are de-coupled, thus increasing power-handling capabilities and unwanted RF coupling effects.
- The third 150-nm gold layer (or floating metal, FLOMET) ensures that the down-state capacity is always the same.
- The process is compatible with high-resistivity silicon wafers and quartz wafers.
- Dielectric-less switches can be designed to increase reability [5].

The following sections will explain the design of capacitive and ohmic switches using the FBK process.

3.1.3 Design of a low-voltage capacitive switch

In this section, the design of a low-voltage electrostatic-actuated capacitive switch will be explained. The chosen characteristics of the capacitive switch are:

- Insertion loss below 1 dB up to 50 GHz.
- Isolation from 20 GHz to 75 GHz higher than 15 dB.
- Pull-in voltage below 25 V.

As explained in section 3.1.1, the pull-in voltage voltage V_{pi} of the devices is defined by the area and separation of the bias electrodes, and also by the stiffness of the suspension k. In this case, folded beam suspensions (Fig. 3.4) were chosen due to its capability to compensate for intrinsic residual stress gradients induced by the fabrication process and to provide a good trade-off between spring-constant values and the spacer thickness, in order to obtain a low-actuation voltage [42, 55].

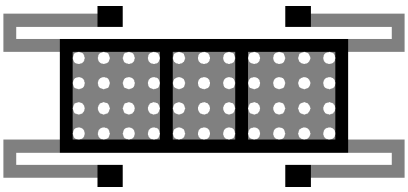

Figure 3.4 – Capacitive switch layout. Grey areas represent a single gold layer with a thickness t_2 = 1.8 μm and black areas represent anchors and the reinforcement frame of the membrane (gold layer with total thickness of $t_1 + t_2$ = 5.3 μm). The membrane is divided in 3 sections, in which the square sections represent the electrodes, and the rectangular (center) section makes contact with the capacitive area.

The devices were fabricated using different thicknesses of sacrificial layer (spacer of 2.7 μm and 1.6 μm). The total stiffness of the suspension can be calculated analytically [42]. However, to take into account the residual stresses produced by the fabrication process, a 3D FEA) (finite element analysis) using ANSYS® Workbench™ has been performed. As shown in the last section, the process allows the deposition of two different gold layers: the suspensions and the membrane can be fabricated with a single layer with a thickness of t_2 = 1.8 μm. The membrane can be reinforced using the second gold layer with a thickness t_1 = 3.5 μm. The used initial stress values are σ_2 = 58 MPa (gold layer with a thickness t_2 = 1.8 μm) and σ_1 = 62 MPa (gold layer with a thickness t_1 = 3.5 μm). Once the dimensions of the device are parameterized, its 3D model is built and the physical properties of the materials of the switch are defined. After meshing the structure and defining the boundary conditions, a static structural simulation was performed.

The area of each polysilicon actuation electrode is 90 μm × 85 μm. The simulated stiffness constant is k_{ANSYS} = 16.3 N/m. Then, the calculated pull-in voltage using (3.6) is V_{pi} = 12 V. In the case of the switch with an air-gap of 2.7 μm, the calculated V_{pi} is 26 V. Fig. 3.5 shows the deformation of the membrane (switch with a 1.6-μm air-gap) when a bias voltage of 12 V is applied to the electrodes.

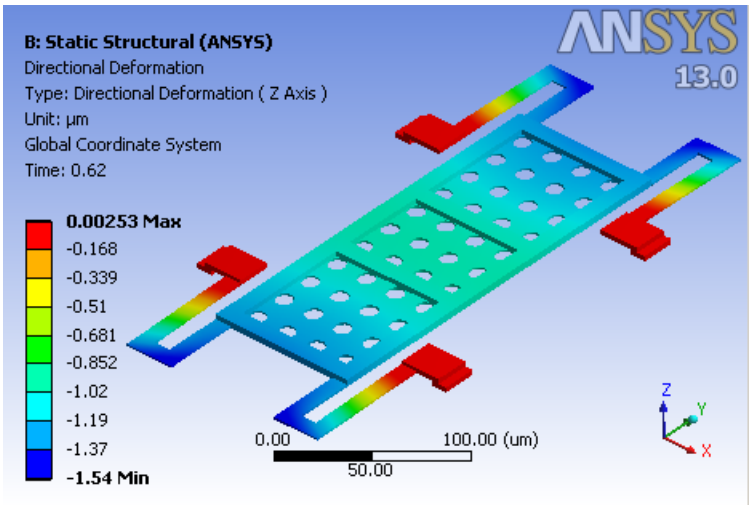

Figure 3.5 – Displacement of the capacitive switch (1.6-μm sacrificial layer) when V_{bias} = 12 V.

Before calculating the required capacitance, an electromagnetic (EM) simulation of the switch should be performed to evaluate the inductance and the resistance of the switch in the down-state, which defines the electrical resonance frequency of the switch. Fig. 3.6 shows the results of the EM simulation (performed using Agilent Momentum). The chosen area of the MIM capacitor (formed by stacking three layers: 150 nm gold (FLOMET), silicon oxide and the multi-metal layer) under the central part of the bridge is 90 μm × 50 μm, which gives a capacitance of 1.5 pF (without taking into account the fringing fields). The MIM capacitor and the inductance of the switch on the down state forms a series RLC circuit, that resonates at 50 GHz.

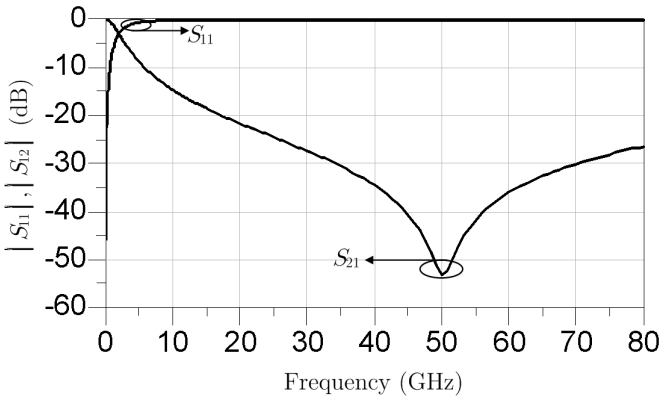

Figure 3.6 – EM simulation of the capacitive switch.

The device was fabricated on a quartz substrate with a thickness h =300 μm, and it is shown in Fig. 3.7. Fig. 3.8 shows the measured C–V hysteresis curve of a 1.6-μm air-gap capacitive switch. The 12-V measured pull-in voltage agrees with FEA simulations. Four devices were measured (two with d = 1.6 μm and two with d = 2.7 μm) showing similar hysteresis curves in each case.

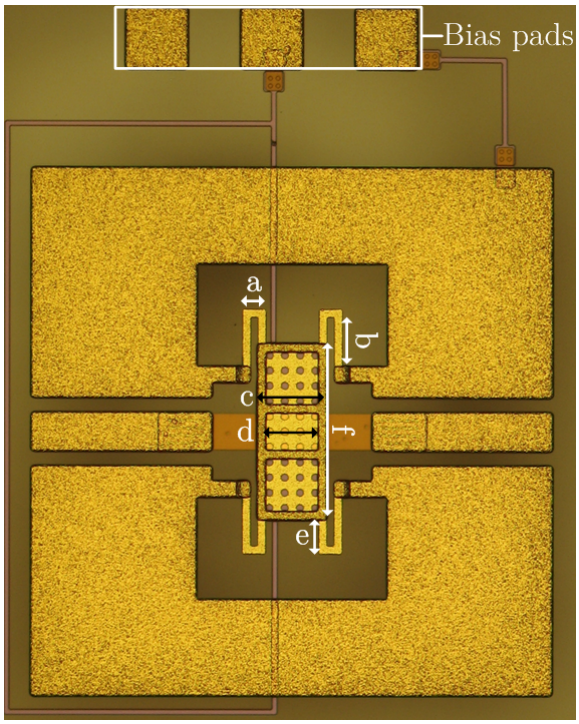

Figure 3.7 – RF-MEMS bridge-type capacitive switch (fabricated on quartz substrate with a thickness $h = 300\ \mu$m).

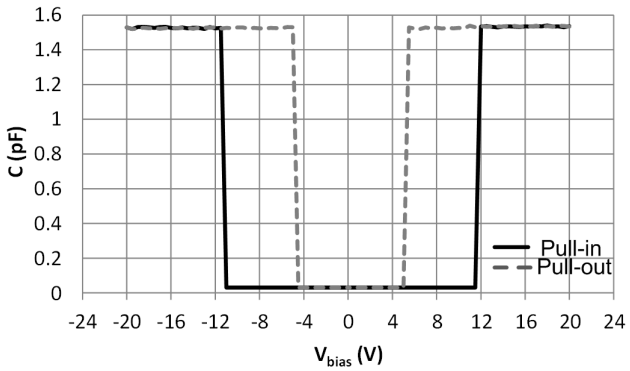

Figure 3.8 – Measured C–V hysteresis of a capacitive switch (air-gap $d = 1.6\ \mu$m).

As can be seen in Fig. 3.7, the switch was implemented on a CPW test-circuit composed of two CPW sections with different dimensions due to fabrication and measurement constraints. The outer CPW sections feature 20-μm slots and a 50-μm central strip, resulting in characteristic even and odd-mode impedances $Z_{0e1} = 65\,\Omega$ and $Z_{0o1} = 100\,\Omega$, respectively. The inner CPW section features 195-μm slots instead, resulting in characteristic even and odd-mode impedances $Z_{0e2} = 135\,\Omega$ and $Z_{0o2} = 195\,\Omega$, respectively. The S parameters of the high impedance CPW line, where the switches are actually placed, were obtained by de-embedding of the low-impedance input and output sections. The dimensions and mechanical parameters of the proposed switches are shown in Table 3.1.

The RF performance of the switches was measured using 150-μm-pitch GSG probes. After normalizing with the appropriate characteristic impedance, the measured insertion loss when the switch is in its up state is lower than 0.4 dB, while the return loss is better than 20 dB up to 50 GHz. Fig. 3.9 shows the measured S parameters when the capacitive switches are in their down state. The measured isolation is better than 20 dB from 15 GHz up to 50 GHz.

Parameter	Air-gap d =1.6 / 2.7 μm
Meander length, a (μm)	30
Supporting-beams width (μm)	10
Supporting-beams length, b (μm)	65
Supporting-beams length, e (μm)	45
Bridge width, c (μm)	90
Window width, d (μm)	70
Bridge length, f (μm)	230
MIM area (μm^2)	50×90
Spring constant, k (N/m)	16.3
Pull-in voltage, V_{pi} (V)	12 / 25
Pull-out voltage, V_{po} (V)	5.5 / 12

Table 3.1 – Dimensions and parameters of the switch of Fig. 3.7.

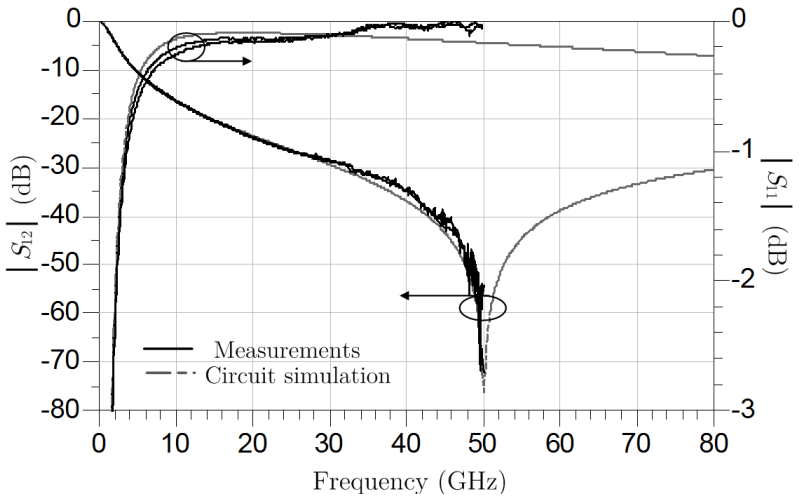

Figure 3.9 – S parameters of two different capacitive switches (with 1.3-μm and 2.7-μm air gap) in the down state.

Fig. 3.10 shows the equivalent circuit model of the capacitive switches. The value of the elements of the equivalent circuit were obtained from the measured data. For 2.7-μm air-gap switches, the up-state capacitance is C_{Coff} = 0.0305 pF. The down-state measured capacitance (on both 1.6-μm and 2.7-μm air gaps) is C_{Con} = 1.53 pF. Thus, the capacitance ratio is C_{Con}/C_{Coff} = 50.16. The circuit simulation is shown in Fig. 3.9. As can be seen, the simulated isolation is better than 30 dB from 31 GHz to 80 GHz.

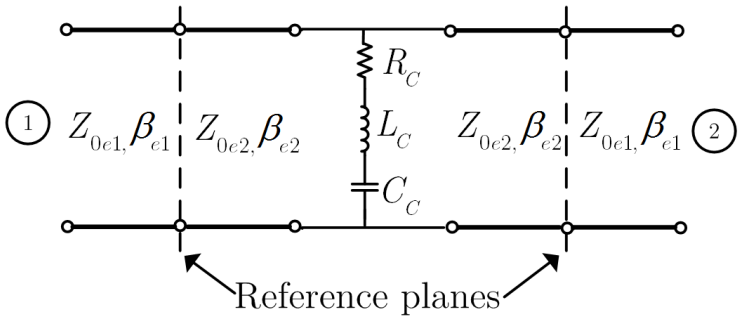

Figure 3.10 – Equivalent circuit model of the capacitive switch. The switch capacitance is C_{Coff} = 0.0305 pF in the up state and C_{Con} = 1.53 pF in the down state. For both states, R_C = 0.01 Ω, L_C = 6.6 pH. β_{e1}, β_{e2} are the CPW even-mode phase constants.

3.1.4 Low-voltage ohmic switches

3.1.4.1 RF-MEMS switchable CPW air-bridges (SABs) on quartz substrates

Fig. 3.11 shows a RF-MEMS ohmic-contact switch which behaves as a switchable short-circuit for the CPW odd-mode. This device can be used in MEMS multimodal circuits and slotline MEMS tunable circuits. When a bias voltage higher than the actuation voltage (V_{pi}) is applied to the electrodes, the bridge makes an ohmic contact with a 150-nm-thick gold layer (FLOMET), which is connected to the ground planes of the CPW, by using the multi-metal layer as an underpass. To improve contact resistance, a dimple (with an area of 10 μm × 12 μm) of polysilicon has been placed under the multi-metal layer at the contact area. Thus, in the up-state, the distance between the membrane and the contact is just 1.3 μm.

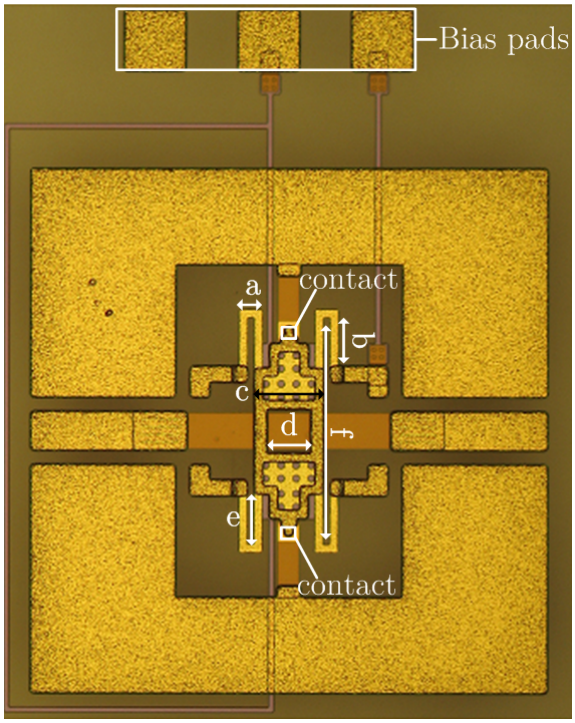

Figure 3.11 – RF-MEMS switchable CPW air-bridge (fabricated on a quartz substrate with a thickness h =300 μm).

As the capacitive switch described in the previous section, this device uses folded-beam suspensions. Because of this, the structure can handle positive and negative stress gradients without compromising the function of the switch. Fig. 3.12 shows the simulated deformation of the bi-layer membrane,

where the used initial stress values are σ_2 = 58 MPa (gold layer with a thickness t_2 = 1.6 μm) and σ_1 = 62 MPa (gold layer with a thickness t_1 = 3.5 μm). For this case, the simulated maximal deflection is less than 0.07 μm.

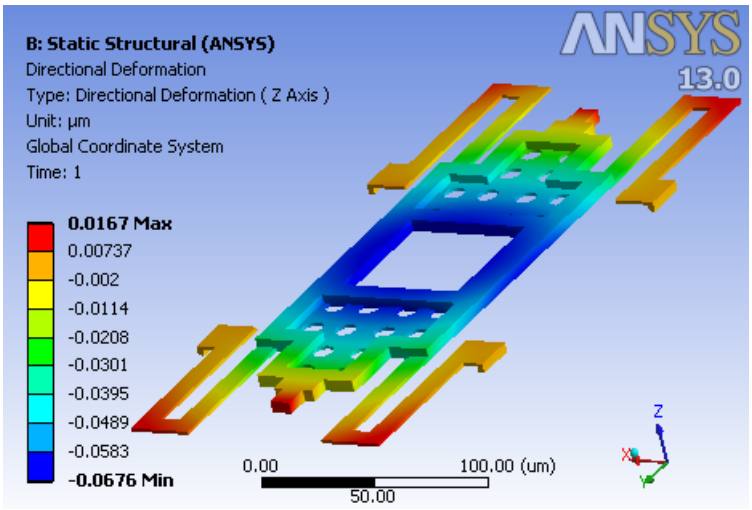

Figure 3.12 – Simulated deformation due to stress gradient effects.

Fig. 3.13 shows an optical-profiler image and a plot of the surface profile of one of the fabricated devices. As can be seen, the main membrane is almost flat. There is a very small negative stress gradient; which has little effect in the performance of the device.

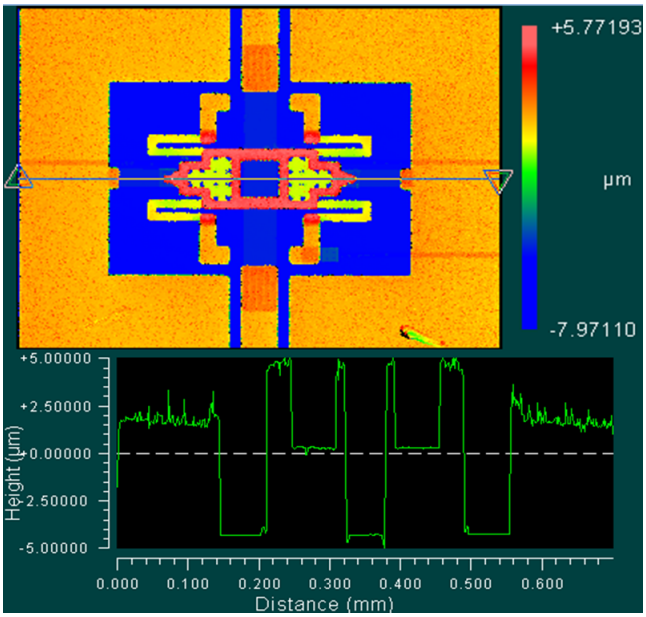

Figure 3.13 – Optical-profiler measurements of the fabricated ohmic switch.

The total overlap area of both electrodes is 0.014 μm^2. The simulated stiffness constant is k_{ANSYS} = 13.3 N/m. Then, the calculated pull-in voltage using (3.6) of the ohmic switches with an air-gap of 1.6 μm is V_{pi} = 11.4 V. The measured V_{pi} is 12 V, as shown in the measured hysteresis C–V curves of Fig. 3.14 .The difference could be attributed to small differences in the thicknesses of the gold layers. As can be seen, the isolation of the switch improves for bias voltages higher than V_{pi} , due to the fact that the contact resistance also improves when the electrostatic force is increased.

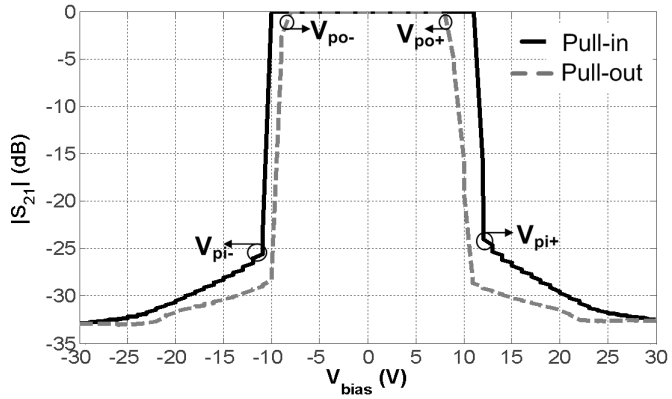

Figure 3.14 – Measured C–V hysteresis (at f = 50 MHz) of an ohmic switch (air-gap d = 1.6 μm).

The dimensions and mechanical parameters of the SAB are shown in Table 3.2.

Parameter	Air-gap d =1.6 μm / 2.7 μm
Meander length, a (μm)	30
Supporting-beams width (μm)	10
Supporting-beams length, b (μm)	78
Supporting-beams length, e (μm)	67
Bridge width 1, c (μm)	90
Window width, d (μm)	60
Bridge length, f (μm)	275
Contact area (μm^2)	10×12
Spring constant, k (N/m)	13.3
Pull-in voltage, V_{pi} (V)	12 / 26
Pull-out voltage, V_{po} (V)	8 / 21
Center-beams area (μm^2)	15×50
Down-state even-mode capacitance (pF)	0.095

Table 3.2 – Dimensions and parameters of the switch of Fig.3.11.

The RF performance of four different ohmic switches, concerning the CPW odd-mode was measured using 150 μm-pitch SG-GS probes. The S parameters of the high-impedance CPW line where the switch is actually placed were obtained from de-embedding of the low-impedance input and output sections. After normalizing with the proper characteristic impedance, it can be seen that the insertion loss of the switch in the up state is better than 1.2 dB up to 30 GHz, and the isolation in the down state is better than 20 dB up to 8 GHz and 10 dB up to 30 GHz, as shown in Fig. 3.15.

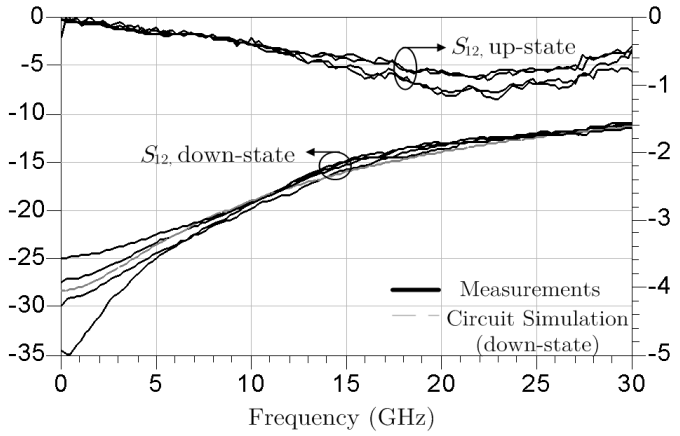

Figure 3.15 – Measured insertion loss (up-state) and isolation (down-state) of four different ohmic switches.

Using the measured data, the circuit model of Fig. 3.16 was obtained for the ohmic switch when it is excited with the CPW odd-mode. The total inductance of the switch is L_t = 0.18 nH and its total resistance is R_t = 2 Ω. This includes the effect of the underpass line and the ohmic-contact resistances. The applied voltage in the above measurements is $1.4 \cdot V_{pi}$ =36.4 V.

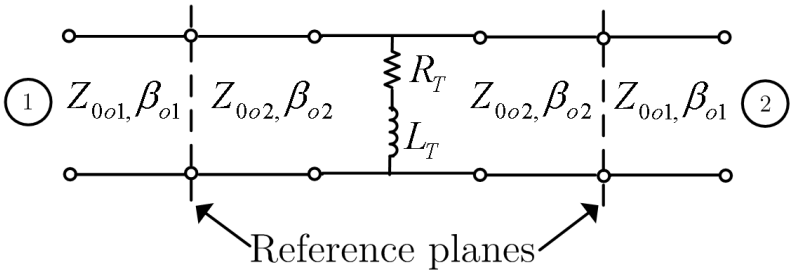

Figure 3.16 – Equivalent circuit model (for the CPW odd mode) when the switch is in the down state, R_T = 2 Ω and L_T = 0.18 nH. β_{o1}, β_{o2} are the odd mode phase constants.

The influence of the switch on the even mode is mainly capacitive. When the pull-in voltage is applied to the electrodes, the bridge touches the contact areas first, avoiding that the center beams of the bridge remain flat above the underpass (less than 20% of the area of the center beams of the bridge is making contact). After measuring the switch using GSG probes, it was found that the capacitance in the down state is C_{pe} = 0.095 pF. The effect of C_{pe} over the even-mode S parameters is shown in Fig. 3.17. If necessary, C_{pe} might be reduced by using narrow center beams (less than 15 μm, if design rules allow it).

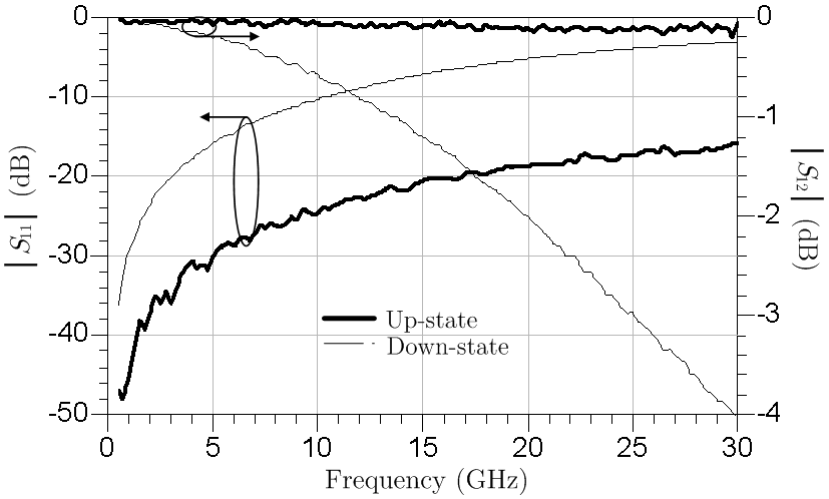

Figure 3.17 – Even-mode measured S parameters for both states.

3.1.4.2 RF-MEMS switchable CPW air-bridges (SABs) on silicon substrates

Fig. 3.18 shows a switchable air-bridge fabricated on a high-resistivity (5 kΩ·cm) silicon substrate, with a permittivity $\varepsilon_r = 11.9$ and thickness $h = 200$ μm, using the integrated RF-MEMS process from FBK. A sacrificial layer of 3 μm was used (the air gap between bias electrodes and the membrane is around 2.9 μm) , and the air gap at the ohmic contact is 2.7 μm. Notice that under the contact areas, a polysilicon bump (dimples with and area of 10 μm × 12 μm and a thickness of 0.63 μm) has been placed to improve the contact.

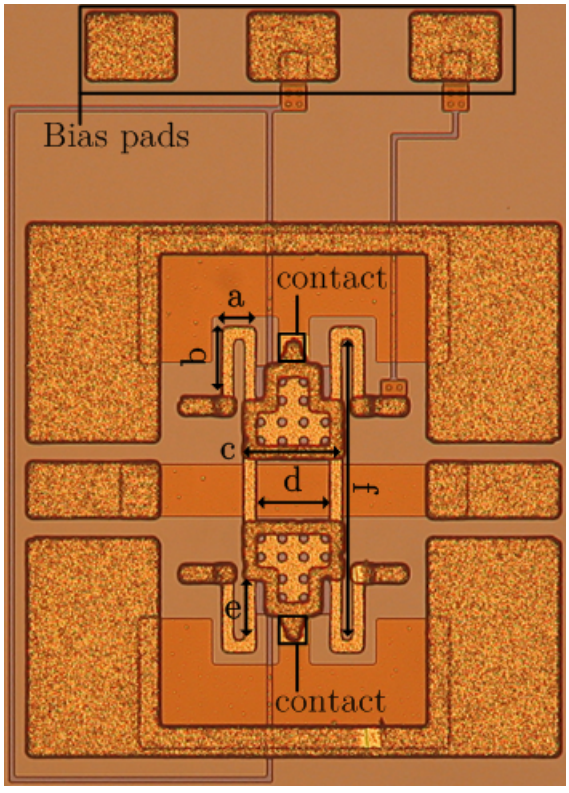

Figure 3.18 – RF-MEMS switchable CPW air-bridge (fabricated on a silicon substrate).

The dimensions of the switch are shown in Table 3.3. Compared to the SAB presented in the previous section (a SAB fabricated on quartz), this device uses shorter folded-beam suspensions to reduce the area of the switch, and thinner center beams to reduce the even-mode capacitance.

Parameter	
Meander length, a (μm)	30
Supporting-beams width (μm)	10
Supporting-beams length, b (μm)	58
Supporting-beams length, e (μm)	58
Bridge width, c (μm)	90
Window width, d (μm)	70
Bridge length, f (μm)	275
Contact area (μm^2)	10×12
Spring constant, k (N/m)	16
Pull-in voltage, V_{pi} (V)	30
Center-beams area (μm^2)	10×50
Down-state even-mode capacitance (pF)	0.047

Table 3.3 – Dimensions and parameters of the switch of Fig.3.18.

As can be seen in Fig. 3.18, the CPW test-circuit has been modified to reduce the inductance of the underpass line connected to the ground planes (which contributes to the total inductance L_t of the switch). The CPW test-circuit is composed of two CPW sections with different dimensions: the outer CPW sections feature 20-μm slots and a 50-μm central strip, resulting in characteristic even and odd-mode impedances $Z_{0e1} = 50\,\Omega$ and $Z_{0o1} = 102\,\Omega$, respectively. The inner CPW section has a characteristic even and odd-mode impedances $Z_{0e2} = 78\,\Omega$ and $Z_{0o2} = 118\,\Omega$, respectively. The S parameters of the high impedance CPW line, where the switches are actually placed, were obtained by de-embedding the low-impedance input and output sections. After normalizing with the proper characteristic impedance, it can be seen that, for the CPW odd-mode, the insertion loss of the switch in the up state is better than 0.65 dB up to 30 GHz, and the isolation in the down state is better than 20 dB up to 9.02 GHz, as shown in Fig. 3.19. Using the same equivalent circuit as in Fig. 3.16, when the switch is in the down state, $R_T = 1\,\Omega$ and $L_T = 0.12$ nH. Thus, R_T and L_T have improved with respect to the SAB fabricated on a quartz substrate.

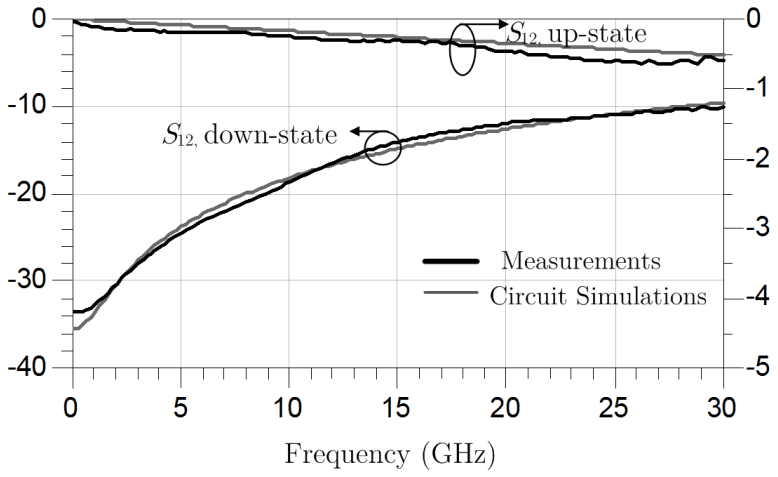

Figure 3.19 – Measured insertion loss (up state) and isolation (down state) of one SAB fabricated on a silicon substrate.

In the down-state, the bridge is making contact with the ground planes, but the overlapping RF area (center beams) is just A_{RF} = 2·(10 μm × 50 μm). As explained before, polysilicon dimples have been placed under the contact areas. Thus, when the pull-in voltage is applied to the electrodes, the bridge touches the contact areas first, avoiding that the center beams of the bridge remain flat above the underpass (less than 20% of the area of the center beams of the bridge is making contact). Since the center beams of the switch are narrower, the measured capacitance in the down state is smaller (C_{pe} =0.047 pF). This agrees with the calculated capacitance of a two-dielectric layer capacitor [42] (assuming that the contact area is 20%, and a roughness, d_{air} =500 Å),

$$C_d = \frac{\varepsilon_0 A}{2}\left(\frac{1}{d_{air} + t_d/\varepsilon_r} + \frac{\varepsilon_r}{t_d}\right)$$

where ε_r is the permittivity of the silicon-dioxide layer.

This means that this SAB has less impact on the CPW even-mode, and, in addition, it is more robust against high-power level effects, such as self-biasing and power latching. Since the switch is not connected to the ground planes in the up-state, and the odd-mode overlapping RF area is minimal, it is highly immune to self-actuation.

3.1.5 A switched capacitor bank

In this section, a MEMS ohmic switch for slotline circuits is presented. Fig. 3.20 (a) shows a slotline 3-bit switched capacitor bank, designed for uniplanar tunable filters operating between X and Ku bands. It is composed of 3 ohmic cantilevers [56], which are connected to MIM capacitors. The 3-bit capacitor bank was fabricated on a high-resistivity (5 kΩ·cm) silicon substrate, with a permittivity ε_r =11.9 and thickness h = 200 μm, using the integrated RF-MEMS process from FBK. A sacrificial layer of 3 μm is used, and the air gap at the ohmic contact is 2.7 μm. The bias electrodes have an area of 110 μm×110 μm . The pull-in voltage is V_{pi} = 56 V, thus the estimated stiffness constant is k = 42 N/m. The ohmic contact between the 1.8-μm-thick gold layer and the FLOMET layer was designed to obtain a low up-state capacitance. Fig. 3.20(b) shows a close-up of a switched capacitor. The overlapped area between each FLOMET finger (there are 7 fingers per switch) and the cantilever is just (14 μm×8 μm), thus the maximum the up-state capacitance per switch is C_{OFF} = 2.5 fF (without fringing effects). This matches with the total up-state measured capacitance of the switched capacitor bank, C_{T_OFF} = 10 fF.

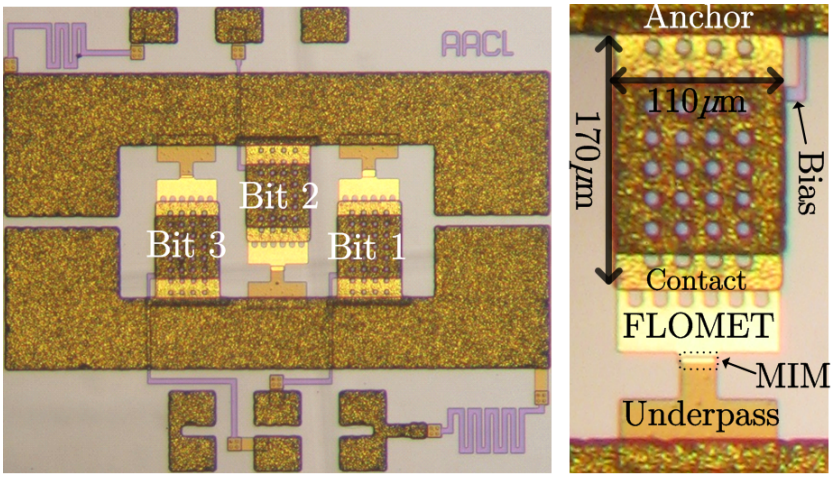

Figure 3.20 – RF-MEMS 3-bit switched capacitor bank. (a) Test structure. (b) Detail of a single switched capacitor.

The area of the switched capacitor bank, including bias lines, is 0.96 mm × 0.82 mm. The capacitor bank of Fig. 3.20(a) was measured using 150-μm-pitch SG-GS probes. Fig. 3.21 shows the measured

S parameters and the insertion phase for all states of the switched capacitor bank. As can be seen, the insertion phase increases as the capacitance of the switched bank increases.

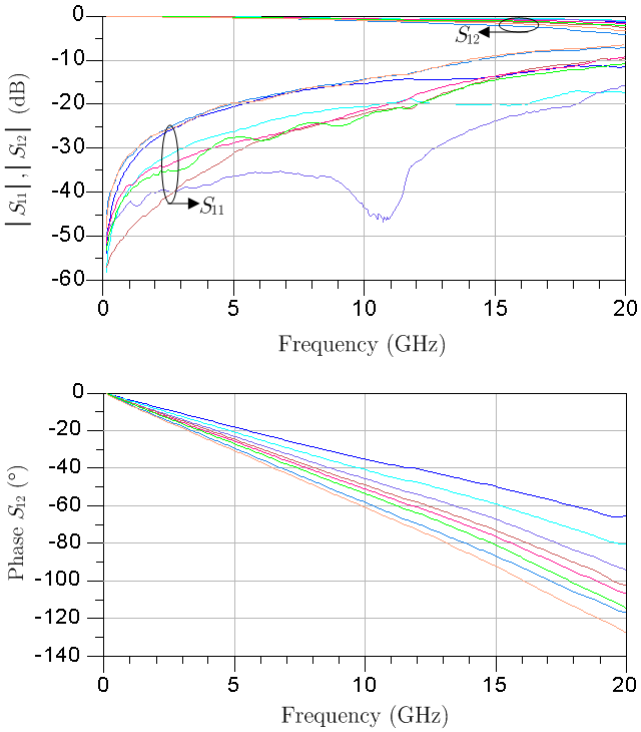

Figure 3.21 – Measured *S* parameters and insertion phase of the switched capacitor bank.

The maximum "down-state" capacitance is C_{T_ON} = 276 fF, and therefore the capacitance ratio is C_{T_ON}/C_{T_OFF} = 27.6. Table 3.4 shows the measured capacitance per bit. From the measured data, the circuit model of Fig. 3.22 was obtained (up-state capacitance per bit is not shown).

Bit	MIM capacitor area (μm^2)	Measured capacitance (ohmic switch in the down state), C_{ON} (fF)
1	25 × 14.5	127.5
2	25 × 11	97
3	25 × 6	51.5

Table 3.4 – Switched capacitor bank parameters.

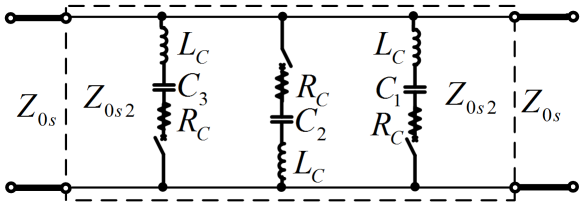

Figure 3.22 – Equivalent circuit model of the 3-bit switched capacitor bank of Fig. 3.20(a). R_C = 1.2 Ω, L_C = 4 pH. Z_{0s} = 50 Ω and Z_{0s2} =90 Ω.

CHAPTER 4

MULTIMODAL BANDPASS FILTERS

This chapter introduces new topologies of uniplanar multimodal bandpass filters. It will be shown that multimodal CPW structures offer potential advantages over conventional microstrip and monomodal CPW filters, such as easy reconfiguration and the possibility to increase the rejection or attenuate harmonics by adding additional transmission zeros, and, at the same time, maintain a small area.

4.1 Multimodal Bandpass filters based on CPW asymmetrical shunt impedances

4.1.1 Bandpass filter based on asymmetrically-loaded resonators

A second-order filter can be obtained by cascading two multimodal resonators, as shown in Fig. 4.1. Here, the central admittance inverter (J_{12}) is a quarter-wavelength even mode CPW, formed by the sum of lengths $l_2 + l_2' + \Delta l$.

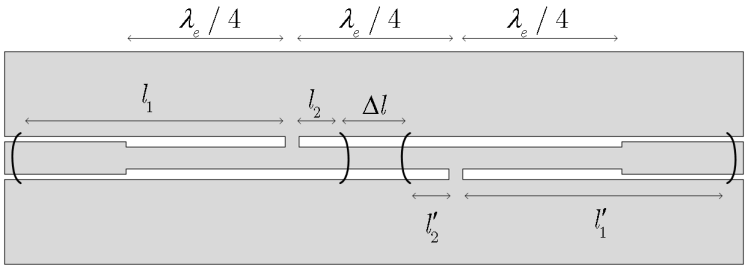

Figure 4.1 – Multimodal CPW bandpass filter.

Admittance inverters J_{01} and J_{23} are also $\lambda_e/4$ CPW sections, whose length is absorbed by l_1 and l_1' respectively. The multimodal circuit model of the bandpass filter is shown in Fig. 4.2.

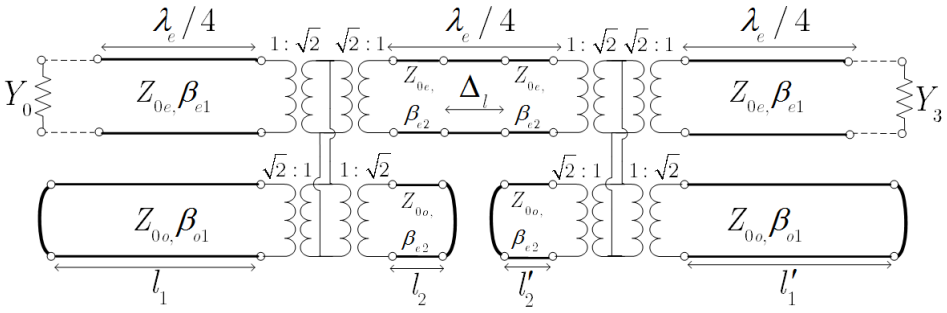

Figure 4.2 – Circuit model of the multimodal CPW bandpass filter.

Following the nomenclature used in [40] for a second-order filter (see Fig. 4.3), the design equations for the structure of Fig. 4.2 are

$$C_{eq1} = \frac{Y_{0e1}^2 \Omega_c g_0 g_1}{Y_0 FBW \omega_0}, \tag{4.1}$$

$$C_{eq2} = \frac{Y_{0e3}^2 \Omega_c g_2 g_3}{Y_3 FBW \omega_0}, \tag{4.2}$$

and

$$\frac{J_{0,1}^2 J_{2,3}^2}{J_{1,2}^2 Y_3^2} = \frac{Y_{0e1}^2 Y_{0e3}^2}{Y_{0e2}^2 Y_3^2} = 1; \tag{4.3}$$

where C_{eq1}, C_{eq2} are the equivalent capacitances of the first and second resonators, respectively (see Fig. 4.3), Y_{0e1} and Y_{0e3} are the characteristic admittance of the first and third inverters, respectively; Y_{0o} and Y'_{0o} are the odd mode characteristic admittance of the first and second resonators, respectively, Y_0 is the generator admittance and Y_3 is the load admittance. Equation (2.3) describes the relationship between the lengths l_1 and l_1' and the capacitances C_{eq1}, C_{eq2} (Chapter 2, Section 2.1.1).

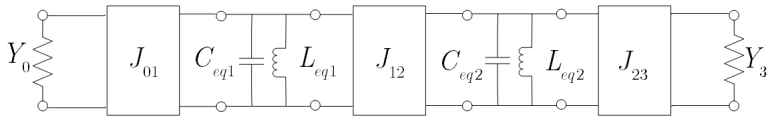

Figure 4.3 – A generalized two-pole bandpass filter using admittance inverters.

Equations (4.1) and (4.2) establish the relationship between FBW, admittance inverters and slot short-circuit positions: the FBW can be changed by varying the characteristic impedance of the inverters or by changing the position of the slot short-circuits. The second option will be demonstrated in chapter 5.

4.1.2 Filters with multimodal immitance inverters and slotline resonators

This section presents the design and implementation of uniplanar bandpass filters that use end-coupled slotline resonators and multimodal immittance inverters (MMIs). The design equations of the CPW-slotline transition as a impedance inverter were presented in Section 2.1.2 of Chapter 2. In this section, different classes of compact, low-loss, arbitrary-order, easily-reconfigurable, uniplanar filters featuring half-wavelength and quarter-wavelength end-coupled resonators are presented. The bandpass filters are based on the coupled-resonator structure of Fig. 4.4, whose normalized inverter values can be computed from [40] and are summarized in Table 4.1. λ_{0s2} is the wavelength for the slotline mode (compatible with the odd mode) at the center frequency f_0.

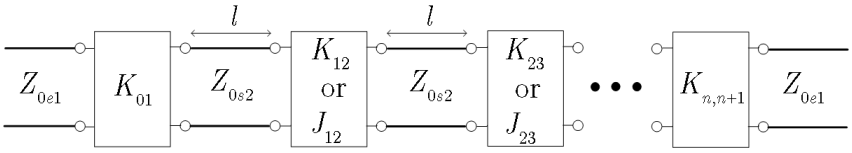

Figure 4.4 – Generic coupled-resonator filter structure.

$l = \lambda_{0s2}/2$	$l = \lambda_{0s2}/4$ (n even)
$K_{01} = \sqrt{\frac{Z_{0e1} Z_{0s2} \pi FBW}{2 g_0 g_1}}$	$K_{01} = \sqrt{\frac{Z_{0e1} Z_{0s2} \pi FBW}{4 g_0 g_1}}$
$K_{i-1,i} = \frac{Z_{0s2} \pi FBW}{2\sqrt{g_{i-1} g_i}}$	$J_{i-1,i}$ (i even) $= \frac{\pi FBW}{4 Z_{0s2} \sqrt{g_{i-1} g_i}}$ or $K_{i-1,i}$ (i odd) $= \frac{Z_{0s2} \pi FBW}{4\sqrt{g_{i-1} g_i}}$
$K_{n,n+1} = \sqrt{\frac{Z_{0e1} Z_{0s2} \pi FBW}{2 g_n g_{n+1}}}$	$K_{n,n+1} = \sqrt{\frac{Z_{0e1} Z_{0s2} \pi FBW}{4 g_n g_{n+1}}}$

Table 4.1 – Design values for the coupled-resonator filter of Fig. 4.4.

Two different filter structures, which use the immitance inverters as their outer K inverters (K_{01} and $K_{n,n+1}$), can be implemented. One of them features half-wavelength ($\lambda_{0s2}/2$) slotline resonators (and inner K inverters realized by inductive coupling [57–59]), as that shown in Fig. 4.5(a) for a second-order filter. The other filter features quarter-wavelength ($\lambda_{0s2}/4$) slotline resonators (and alternating J and K inner inverters realized by capacitive [57] and inductive coupling, respectively), as that shown in Fig. 4.5(b), again for a second-order filter. The CPW-slotline transitions used as (outer) multimodal immittance inverters (see Section 2.1.2) perform simultaneously several circuit functions:

• They behave as immitance inverters.

• They perform a modal conversion between the exciting CPW even modes and the inner slotline modes, including the impedance transformation between even and slotline modes (usually $Z_{0s2} > Z_{0e1}$), which is embedded in their behavior as inverters.

• They perform, in contrast with other CPW-to-slotline transitions reported in the literature, a shunt connection between an input (even-mode) CPW, an output slotline and two even/odd-mode CPW stubs in a simple way. This shunt connection is necessary for the filters proposed below.

• They can create additional transmission zeros to attenuate harmonic transmission bands.

On the other hand, the inner slotline structure presents several advantages over a CPW even-mode one:

• It is easier to bend slotline resonators (for size-reduction) than CPW resonators since the former do not present problems associated with odd-mode generation (and resonance) which can arise from the non-ideal behavior of the air bridges placed at the CPW bends [21].

• The inductive and capacitive coupled ends of the slotline sections are more immune to dimension tolerances than those of even-mode sections, thus resulting in better-defined and repeatable inverter constants.

• Reconfigurable filters can be easily obtained by means of active devices shunt connected between lateral ground planes in slotline or odd-mode structures. This technique avoids the symmetric active-device duplication needed in even-mode configurations, with its associated problems of space and of spurious odd-mode generation if the symmetry is not well preserved.

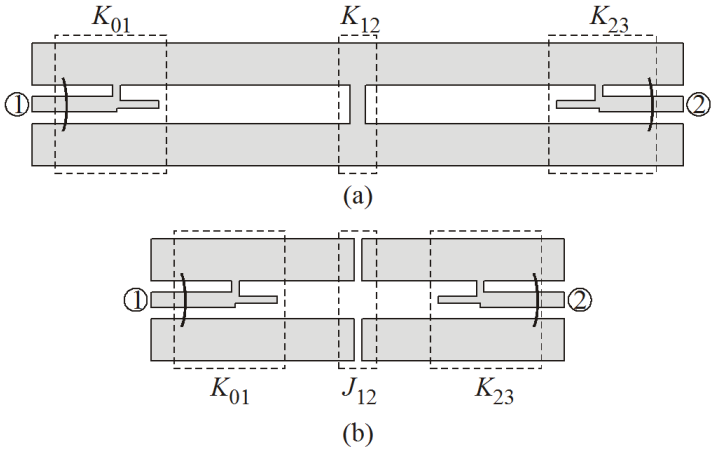

Figure 4.5 – Second-order multimodal coupled-resonator bandpass filters. (a) Filter with half-wavelength ($\lambda_{0s2}/2$) slotline resonators (and inner K inverters). (b) Filter with quarter-wavelength ($\lambda_{0s2}/4$) slotline resonators (and alternating inner J and K inverters).

The filter of Fig. 4.5(a) can be modeled by using the multimodal circuit of presented in section 2.1.2 for the outer K_{01} and K_{23} inverters, as shown in Fig. 4.6(a). From Fig. 4.6(a), it is apparent that the filter features a physical odd-mode–slotline resonator of length $l_r = l_{o1} + l_{s2} + \lambda_{0s2}/2$, where $l_{o1} \approx -l_{s2}$. Thus, the second-order filter of Fig. 4.6(a) has a total length around λ_{0s2}.

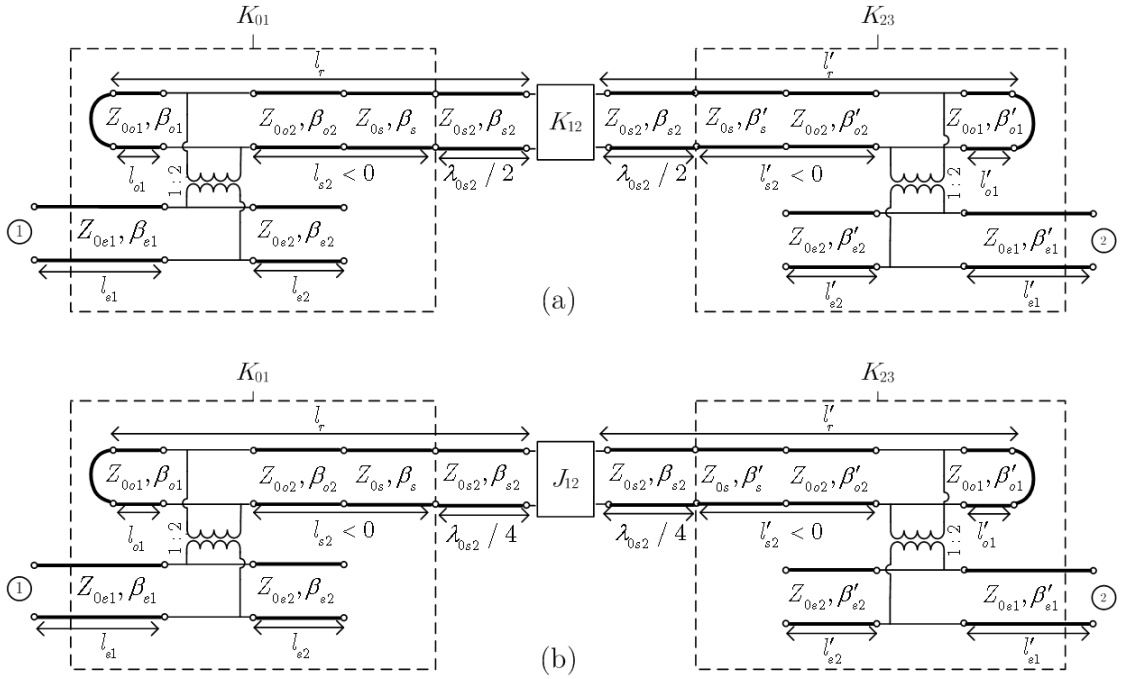

Figure 4.6 – (a) Multimodal circuit model for the filter with half-wavelength slotline resonators of Fig. 4.5(a). (b) Multimodal circuit model for the filter with quarter-wavelength slotline resonators of Fig. 4.5(b).

In the same way, the filter of Fig. 4.5(b) can be also modeled by using the multimodal circuit of presented in section 2.1.2 for the outer K_{01} and K_{23} inverters, as shown in Fig. 4.6(b). In this case, the filter features a physical odd-mode–slotline resonator of length $l_r = l_{o1} + l_{s2} + \lambda_{0s2}/4$, where $l_{o1} \approx -l_{s2}$. Thus, the second-order filter of Fig. 4.6(b) has a total length around $\lambda_{0s2}/2$.

The filters of Fig. 4.5 exhibit the following transmission zeros and attenuated bands:

• The usual attenuated bands of the coupled-resonator filter structures of Fig. 4.4, i.e. at $(2n+1)\cdot f_0/2$ for a filter with half-wavelength resonators (Fig. 4.5(a)), and at $2n\cdot f_0$ for a filter with quarter-wavelength resonators [Fig. 4.5(b)].

• Transmission zeros at frequencies where $\beta_{o1} l_{o1} = n\pi$ (Fig. 4.5), because a short circuit is seen at the asymmetric shunt-short-circuit transition.

• Transmission zeros at frequencies where $\beta_{e2} l_{e2} = (2n+1)\cdot\pi/2$ (Fig. 4.5), because a short circuit is seen at the asymmetric shunt-short-circuit transition.

• Attenuated bands at frequencies where $\beta_{s2}(l_{s2}+\lambda_{0s2}/2) \approx n\pi$ for a filter with half-wavelength resonators (Fig. 4.5(a)) because the approximate short-circuit condition of the K_{12} inverter transforms into an imperfect short circuit at the asymmetric shunt-short-circuit transition.

• Attenuated bands at frequencies where $\beta_{s2}(l_{s2}+\lambda_{0s2}/4) \cong (2n+1)\cdot\pi/2$ for a filter with quarter-wavelength resonators (Fig. 4.5(b)) because the approximate open-circuit condition of the J_{12} inverter transforms into an imperfect short circuit at the asymmetric shunt-short-circuit transition.

Thus, the filter design offers multiple degrees of freedom in order to allocate transmission zeros at several filter harmonic passbands. For instance, in the quarter-wavelength filter of Fig. 4.5(b), a choice of $\beta_{e2} l_{e2} = \pi/6$ and $\beta_{e2} l'_{e2} = \pi/10$, at f_0, would generate transmission zeros at $3f_0$, $9f_0$, $15f_0$, ,..., and $5f_0$, $15f_0$, $25f_0$,..., respectively, thus attenuating the first ($3f_0$) and second ($5f_0$) harmonic bands, among others. Besides, the rest of attenuation and transmission-zero generation mechanisms described above would generate additional attenuated bands which could result in a very wide spurious-free band.

4.1.2.1 Filters with half-wavelength slotline resonators

In order to design the filter (let us suppose a second-order filter such as that of Fig. 4.5(a)) , for a desired fractional bandwidth FBW and low-pass filter prototype elements, the required inverter constants are calculated using the expressions in Table 4.1. Next, $|B_L|$, $\beta_{e1}l_{e1}$ and $\beta_{s2}l_{s2}$ are computed, using the equations of section 2.1.2, for $|B| = 1/K_{01}$ and physically realizable characteristic impedances. With $\beta_{e2}l_{e2}$ chosen to suppress some harmonic pass band, $\beta_{o1}l_{o1}$ can then be computed. The same procedure is applied to the output inverter K_{23}. Finally, the inverter K_{12} is designed by properly choosing the inductive coupling between slotline-section ends using the pole-splitting method [41]. A useful expression for assessing the attainable filter FBW, in terms of the admittance ratio $R = Y_{0s2}/Y_{0e1}$ is

$$FBW = \frac{g_0 g_1}{\pi} \cdot \left[F - \sqrt{F^2 - 4}\right] \tag{4.4}$$

where

$$F = 4R \cdot \left(1 + \frac{1}{16R^2} + \left|\bar{B}_L\right|^2\right).$$

From (4.4) it can be seen that, for a chosen value of l_{e2}, the FBW can be controlled either by changing the length l_{o1} or the impedance ratio R. In Fig. 4.7, the attainable FBW for a half-wavelength filter ($l = \lambda_{0s2}/2$) is plotted as a function of the electrical length $\beta_{o1}l_{o1}$, with R as parameter. The degree of control on the FBW by changing R (which depends on the CPW transverse dimensions) is more limited than by changing $\beta_{o1}l_{o1}$.

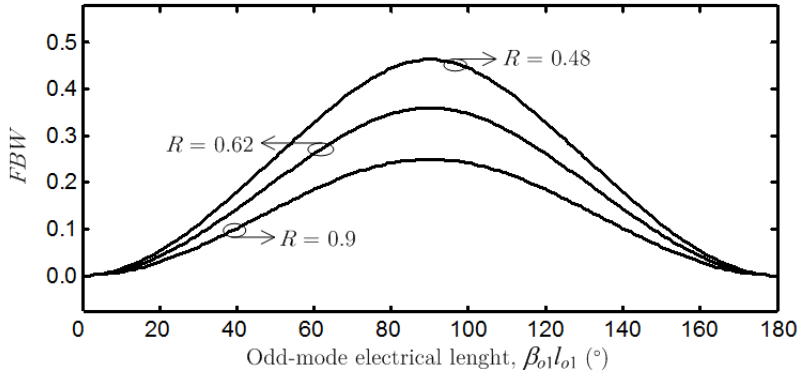

Figure 4.7 – Attainable FBW versus odd-mode electrical length $\beta_{o1}l_{o1}$ (for $l_{e2} = 0$), for a half-wavelength filter ($l = \lambda_{0s2}/2$) .

4.1.2.2 Filters with half-wavelength slotline resonators and stub-line-stub sections

In order to shorten a slotline section in the filter of Fig. 4.5(a) (or, in fact, in any other), as well as to achieve a better harmonic band suppression, a slotline section of length l can be replaced by a shorter stub-line-stub (SLS) section (Fig. 4.8), with slotline characteristic impedance Z_{0l} and identical series slotline stubs with input reactance X_s. The relationship between the length l of the replaced slotline section, its characteristic impedance Z_{0s2}, and the parameters of the SLS section ($\beta_l l_l$, Z_{0l}, and X_s) can be derived, at the filter center frequency f_0 as

$$\bar{X}_s = -\cot(\beta_s l) + \sqrt{\left(\frac{1}{\sin(\beta_{s2} l)}\right)^2 - \left(\bar{Z}_{0l}\right)^2} \tag{4.5}$$

$$\bar{Z}_{0l} = \frac{sin(\beta_l l_l)}{sin(\beta_{s2} l)}, \tag{4.6}$$

where X_s and Z_{0l} are normalized to Z_{0s2}. The minimal achievable Z_{0l} (corresponding to the minimal achievable slot width), limits the amount of length reduction (l_l as compared to l) in (4.6). For a typical impedance ratio = 0.7 and $\beta_{s2l} l = 90°$, the length reduction would be some 25%. The insertion of a SLS section modifies the filter fractional bandwidth FBW due to the change in the slope of susceptance at the resonator feeding points caused by the series stubs and the different characteristic impedance Z_{0l} of the reduced section. Since the analytical expression of the susceptance slope is cumbersome, the multimodal model of Fig. 4.6(a) (modified with that of Fig. 4.8 (b)) can be used to easily fine tune the feeding point and SLS-section position to preserve the intended FBW. Only small changes in the length l_{o1} are required. The short-ended stubs of input reactance X_s provide additional transmission zeros at those frequencies where their length is an odd multiple of a quarter of wavelength because then an open circuit is presented to the slotline.

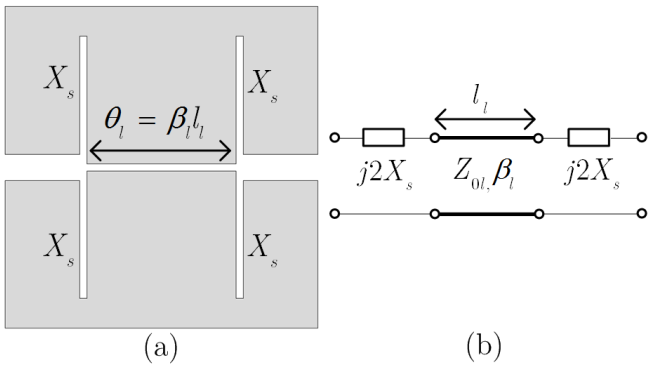

Figure 4.8 – Stub-line-stub (SLS) sections. (a) Topology. (b) Circuit model.

A second-order Butterworth bandpass filter with half-wavelength slotline resonators and SLS sections was designed, with center frequency f_0 = 2 GHz and FBW = 0.04 (Fig. 4.9). It was fabricated on a Rogers RO3003 substrate with ε_r = 3.02, dielectric thickness of 1.52 mm, tanδ=0.0013, and copper-layer thickness of 35 μm. The dimensions of its CPW section are: central-strip width w = 0.6 mm, slot width s = 0.3 mm, and ground-plane width w_g = 8.96 mm. The slot width of the slotline section is 1.2 mm. For these dimensions, Z_{oe} = 83 Ω and $Z_{0o} = Z_{0s}$ = 92 Ω.The width of the SLS stubs and line is 0.2 mm, which corresponds to an impedance Z_{0l} = 67 Ω, and their electrical lengths are 25.26° and 46.656° respectively. The rest of the filter parameters are summarized in Table 4.2.

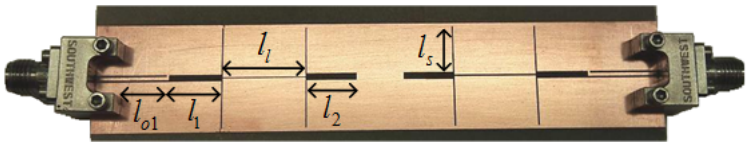

Figure 4.9 – Fabricated second-order bandpass filter with half-wavelength slotline resonators and SLS sections.

l_{o1}, l'_{o1}	7.6 mm
l_{s2}, l'_{s2}(calculated)	-9.05 mm
l_s	8.3 mm
l_l	14.5 mm
Length of first slotline section, l_1	9.1 mm
Length of second slotline section, l_2	8.8 mm
l_r, l'_r	39.75 mm
Coupling length (K_{12} inverter)	8 mm

Table 4.2 – Dimensions of the filter of Fig. 4.9.

Fig. 4.10 compares the filter measured S parameters with those obtained from its multimodal circuit model (including transmission-line losses). The insertion loss is 1.8 dB, and the return loss is better than 25 dB at f_0. The good agreement between simulation and measurement validates the proposed filter concept and its multimodal analysis.

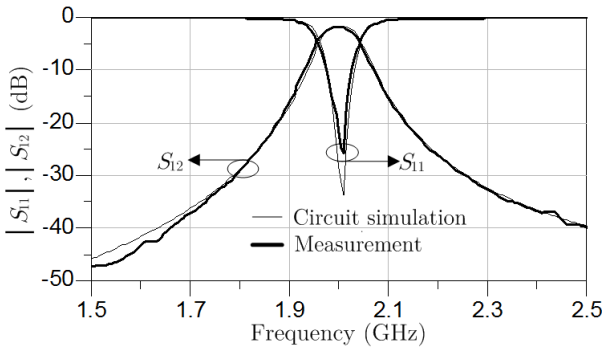

Figure 4.10 – Comparison between measurement and circuit simulation of the filter of Fig. 4.9.

The filter area is 89 mm × 19 mm; since the odd-mode wavelength is 119.2 mm at 2 GHz, the filter length (in λ) is 0.74 λ. As mentioned above, the SLS structure reduces length and improves the out-of-band rejection, due to the frequency response of the SLS, which is close to the frequency response of the replaced slotline section only at the vicinity of f_0, but differs from it at other frequencies. Specifically, it can be shown by simulation of the SLS section alone that the presence of the SLS stubs creates a transmission zero at 7.61 GHz, where the SLS stub lengths (l_s) are a quarter of wavelength (open circuit presented to the slotline). Other zeros are created at 11.32 GHz, where the odd-mode stub l_{o1} is a half-wavelength, and at 2.27 GHz, where the rest of the odd-mode resonator (formed by l_1, the SLS section and l_2) behaves as a half-wavelength stub, thus presenting short circuits at the slotline-resonator feeding point. Due to these combined effects, the harmonic pass bands at nf_0 are attenuated. In Fig. 4.11, the measured filter response is plotted up to 16 GHz, showing that the harmonic pass bands are below –20 dB in a wide frequency range (4–16 GHz). The difference between the multimodal circuit simulation and the measured data above 6 GHz is attributed to the fact that the circuit modeling of the inductive coupling (performed at f_0 = 2 GHz) looses its accuracy above this frequency, and to parasitics added by the coaxial-to-CPW transition.

4.1.2.3 Filters with quarter-wavelength slotline resonators

The filter structure depicted in Fig. 4.5 (b) can be modeled, by using the multimodal of section 2.1.2, for the outer K_{01} and K_{23} inverters, as shown in Fig. 4.6 (b). In this case, slotline $\lambda_{0s2}/4$ resonators are used, so the filter length is roughly a half of that presented in section 4.1.2.1. It can be designed, from the parameters on Table 4.1, for the generic filter of Fig. 4.4, in an analogous way. Fig. 4.12 shows the layout of a second-order filter with slotline meanders to improve its compactness.

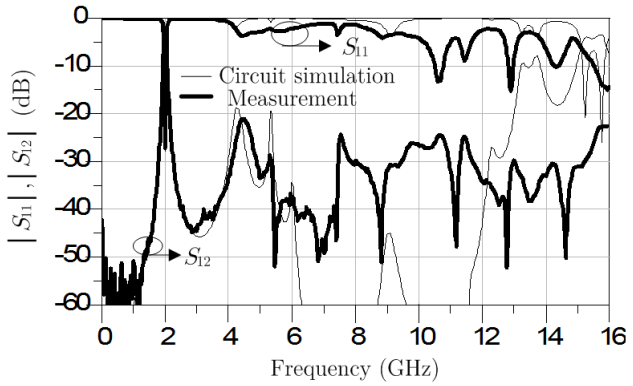

Figure 4.11 – Measured wide-band response of the filter of Fig. 4.9 and circuit simulation.

As explained above (see Fig. 4.4), higher-order filters with quarter-wavelength slotline resonators can be obtained by alternating J and K inverters, as in the fourth-order filter whose layout is shown in Fig. 4.13 . The two inner resonators of this filter were bent in order to achieve greater compactness, whereas its two outer resonators were not bent in this case so as to facilitate its measurement with a probe station.

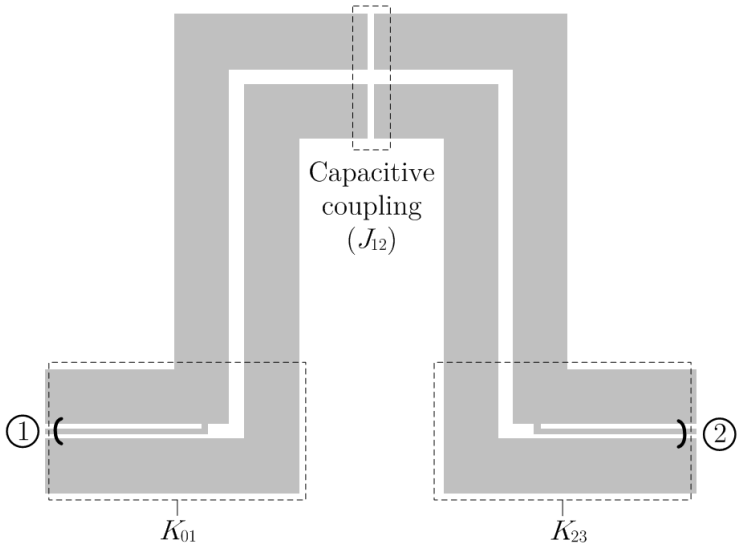

Figure 4.12 – Layout of the fabricated second-order bandpass filter with quarter-wavelength slotline resonators.

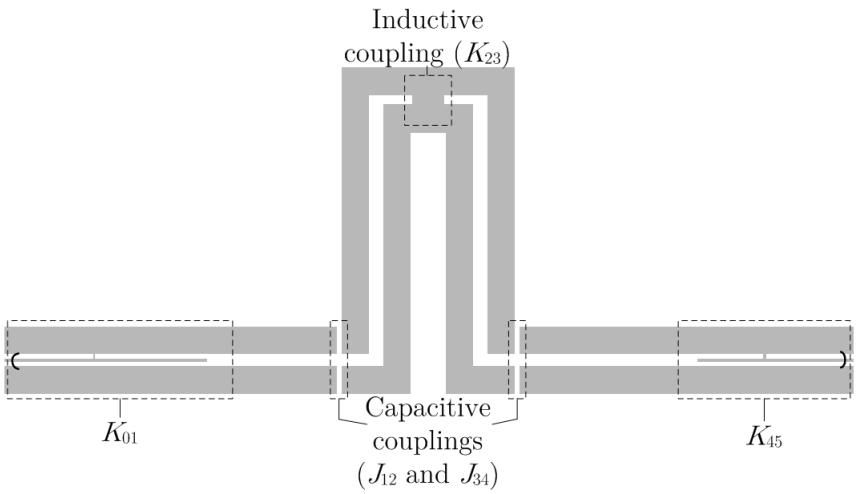

Figure 4.13 – Layout of the fabricated fourth-order bandpass filter with quarter-wavelength slotline resonators.

l_{o1}, l'_{o1}	5.1 mm
l_{s2}, l'_{s2}	-5.03 mm
l_r, l'_r	25.8 mm
Coupling gap (J_{12} inverter)	0.1 mm

Table 4.3 – Dimensions of the filter of Fig. 4.14 (a).

Both filters were fabricated on the Rogers RO3003 substrate, with a ε_r = 3.02, dielectric thickness of 1.52 mm, tanδ=0.0013, and copper-layer thickness of 35 μm. For the input and output CPW sections, a central-strip width of s = 0.2 mm, with a slot width of w = 0.1 mm and a ground-plane width of w_g = 2.18 mm were used. The slotline section has a slot width of 0.4 mm. For the chosen dimensions, Z_{0e} = 75 Ω, $Z_{0o} = Z_{0s}$ = 90.5 Ω. For the second-order filter, a Chebyshev response with a ripple of 0.1 dB, FBW = 0.05, and center frequency f_0 = 1.95 GHz, was chosen. The fabricated filter, with an area of 25.4 mm × 18.95 mm, and whose lengths are listed in Table 4.3, is shown in Fig. 4.14 (a).

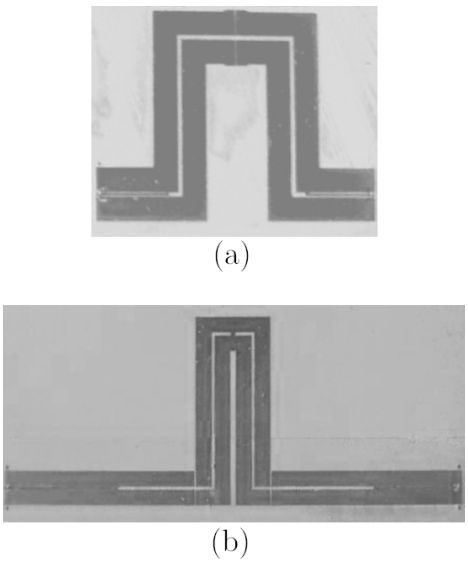

Figure 4.14 – Fabricated bandpass filters with quarter-wavelength slotline resonators. (a) Second-order 1.95-GHz filter. (b) Fourth-order 2-GHz filter with even-mode stubs for harmonic pass band attenuation.

Fig. 4.15 compares the filter measured S parameters with those obtained from its multimodal circuit model (including transmission-line losses). A minimal insertion loss of 1.6 dB can be appreciated in the pass-band response shown in Fig. 4.15(a). In Fig. 4.15 (b) the wide-band response is plotted showing that the first harmonic pass band at $3f_0$ (as expected from a filter based on $\lambda_{0s2}/4$ resonators) is not attenuated because no even-mode stubs are used in the multimodal inverters.

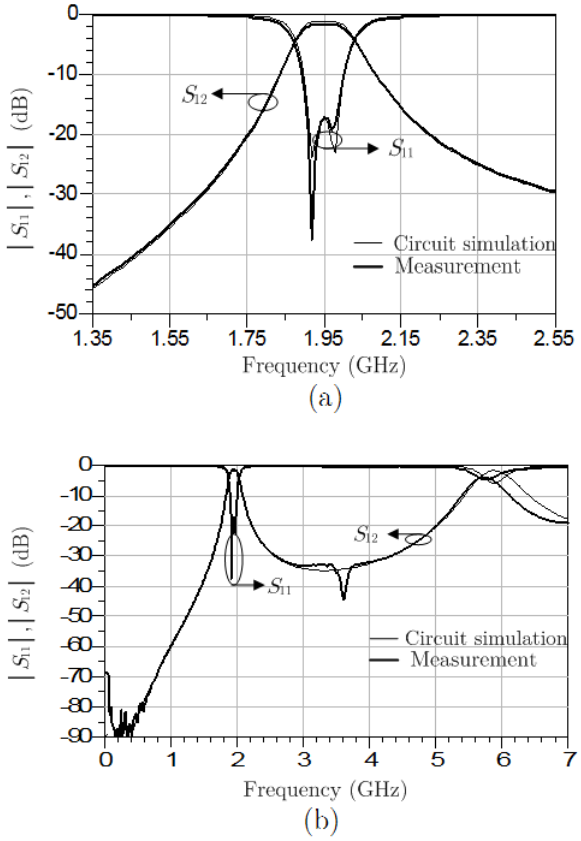

Figure 4.15 – Comparison between measurement and circuit simulation of the filter of Fig. 4.14 (a). (a) Narrow-band response. (b) Wide-band response.

For the fourth-order filter of Fig. 4.14 (b), whose area is 63 mm × 37 mm, a Chebyshev response with a ripple of 0.5 dB was chosen, with $FBW = 0.1$ and a center frequency $f_0 = 2$ GHz. Its relevant lengths are listed in Table 4.4. In this case, the outer multimodal inverters K_{01} and K_{45} include even-mode stubs whose lengths l_{e2} and l'_{e2} have been chosen to attenuate the first and second harmonic pass bands at $3f_0$ ($\beta_{e2}l_{e2} = \pi/6$) and $5f_0$ ($\beta_{e2}l'_{e2} = \pi/10$), respectively. In Table 4.5, the expected attenuated frequency bands are for the filter of Fig. 4.14 (b) are listed, according to the attenuated-band and transmission-zero generating processes described in Section 4.1.2.

l_{o1}	5.79 mm
l'_{o1}	5.97 mm
l_{e2}	8.75 mm
l'_{e2}	5.22 mm
l_{s2}, l'_{s2}	-6.1 mm
l_r	25.43 mm
l'_r	25.61 mm
Coupling gaps (J_{12} and J_{34} inverters)	0.175 mm
Coupling length (K_{23} inverter)	0.6 mm

Table 4.4 – Dimensions of the filter of Fig. 4.14 (b).

Fig. 4.16 compares the filter measured S parameters with those obtained from its multimodal circuit model (including transmission-line losses). The minimal measured insertion loss is 2.2 dB.

Attenuation mechanism	Frequencies (GHz)
$2n \cdot f_0$	4, 8, 12, 16, 20, 24, 28, 32, 36, 40, 44, 48
$\beta_{e2} l_{e2} = (2n+1) \cdot \pi/2$	6, 18, 30, 42
$\beta_{e2} l'_{e2} = (2n+1) \cdot \pi/2$	10, 30, 50
$\beta_{o1} l_{o1} = n \cdot \pi$	17.4, 34.8
$\beta_{o1} l'_{o1} = n \cdot \pi$	16.88, 33.76
$\beta_{s2}(l_{s2} + \lambda_{0s2}/4) \cong (2n+1) \cdot \pi/2$	2.64, 7.92, 13.20, 18.5, 23.75, 29, 34.3, 39.6, 44.9

Table 4.5 – Expected attenuated frequency bands for the filter of Fig. 4.14 (b).

Fig. 4.17 shows a wide-band comparison between simulation and measurement, in which it is apparent that the spurious harmonic bands at $3f_0$ and $5f_0$ are attenuated due to the effect of the even mode stubs. Finally, Fig. 4.18 shows the measured response up to 50 GHz, proving that the other bands listed in Table 4.5 are also attenuated below –20 dB up to 50 GHz. Again, the good agreement between simulations and measurements in Figs. 4.16 to 4.18 validates the proposed filter concept and its multimodal analysis.

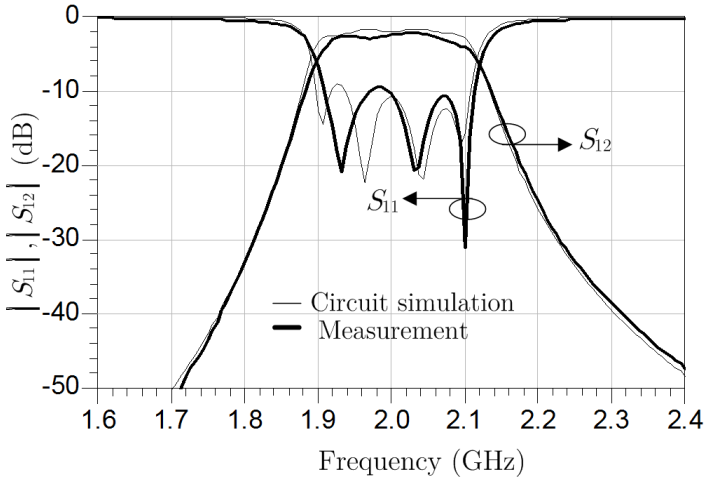

Figure 4.16 – Narrow-band comparison between measurement and circuit simulation of the filter of Fig. 4.14 (b).

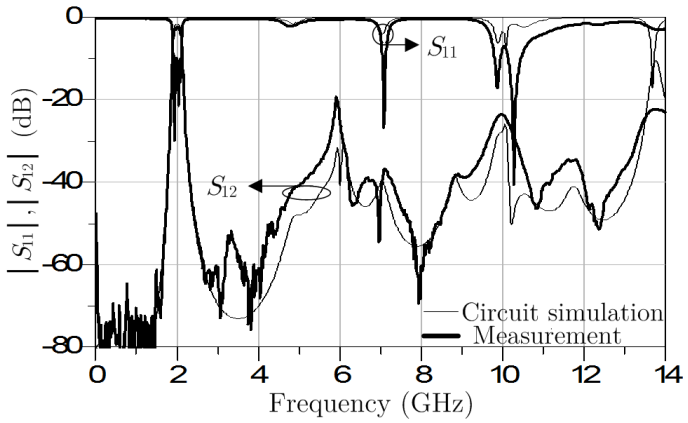

Figure 4.17 – Wide-band comparison between measurement and circuit simulation of the filter of Fig. 4.14 (b).

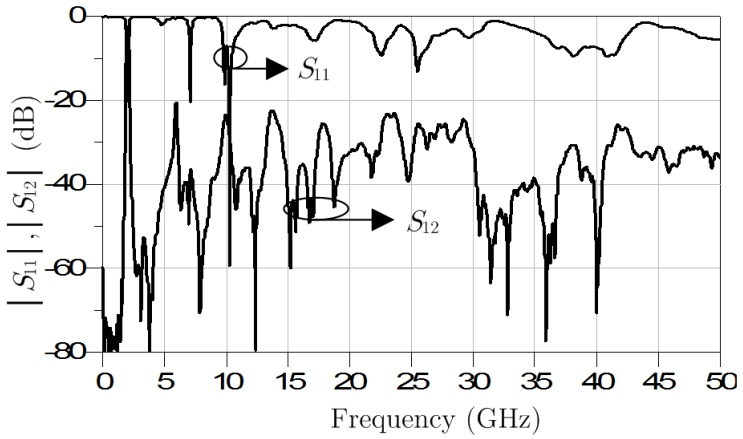

Figure 4.18 – Wide-band measured behavior (0.1GHz-50 GHz) of the filter of Fig. 4.14 (b).

4.2 Uniplanar Bandpass Filters Based on Slotline-CPW Tees

4.2.1 Reduced-length filter based on a single slotline-CPW tee per resonator

Fig. 4.19 shows the layout of a bandpass filter that uses multimodal immittance inverters at the input and output (K_{01} and K_{23}), like the filters proposed in the last section. Instead of bending the resonators, this filter uses slotline-CPW tees to reduce the length of each resonator. This filter can be modeled, by using the multimodal theory of section 2.1.2 for the outer K_{01} and K_{23} inverters, and the theory of section 2.2.1 for the reduced-length slotline ($\lambda_{0s2}/4$) resonators.

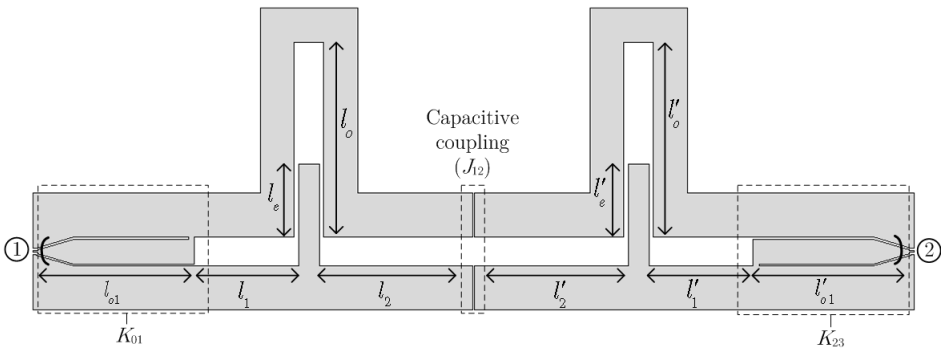

Figure 4.19 – Second-order multimodal coupled-resonator bandpass filter with reduced-length quarter-wavelength ($\lambda_{0s2}/4$) slotline resonators featuring slotline-coplanar tees.

The multimodal circuit model of the filter of Fig. 4.19 is shown in Fig. 4.20. Using the equations proposed in sections 2.1.2 and 2.2.1, a second-order multimodal coupled-resonator bandpass filter with quarter-wavelength ($\lambda_{0s2}/4$) slotline resonators has been designed. The chosen response is Chebyshev with a ripple of 0.1 dB, and a FBW = 0.08 at f_0 = 1.52 GHz. A Rogers RO4350B substrate with a relative permittivity ε_R = 3.66 and thickness h = 1.52 mm has been chosen. The dimensions of the CPW section of the multimodal immittance inverters (K_{01} and K_{23}), are: CPW central-strip width w = 1.22 mm, CPW slot width s = 0.1 mm, slotline slot width $2s+w$ and CPW section ground plane width w_g = 2.18 mm. In order to measure the filter using 250 μm-pitch GSG probes, a taper with a length l_t = 2 mm, CPW central-strip width w = 0.1 mm and CPW slot width s = 0.1 mm has been used at the input and output of the filter.

The dimensions of the slotline-CPW tee are: CPW central-strip width w = 1.04 mm, CPW slot with s = 0.21 mm, slotline slot width $2s+w$, and CPW section ground plane width w_g = 1.68 mm. For a insertion phase of 25° at f_0 = 1.52 GHz, the calculated dimensions of the CPW section are l_e = 3.63 mm and l_o = 9.65 mm.

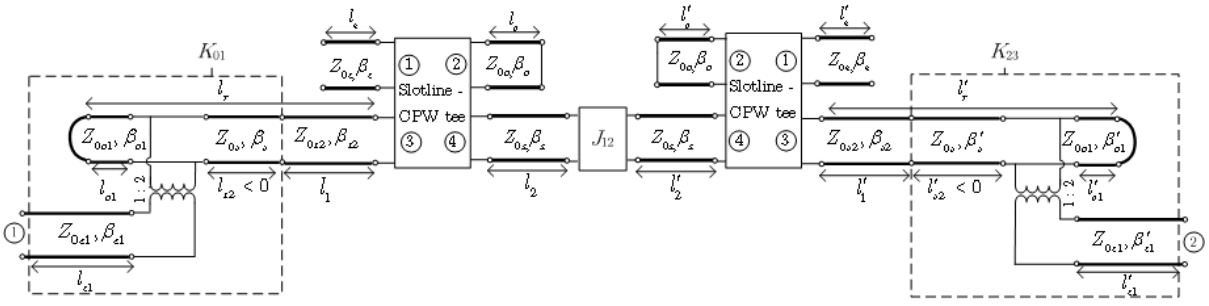

Figure 4.20 – Second-order multimodal coupled-resonator bandpass filter with reduced-length quarter-wavelength ($\lambda_{0s2}/4$) slotline resonators, using MIIs and slotline-CPW Tees.

Fig. 4.21 shows the fabricated filter and its dimensions are shown in Table 4.6 .The total area of the filter is 45.1 mm × 14.9 mm.

l_{o1}, l'_{o1}	8.3 mm
l_{s2}, l'_{s2}(calculated)	-8.1 mm
Length of first slotline section, l_1	4.95 mm
Length of second slotline section, l_2	7.4 mm
l_r, l'_r	34.7 mm
Coupling gap (J_{12} inverter)	0.1 mm

Table 4.6 – Dimensions of the filter of Fig. 4.21.

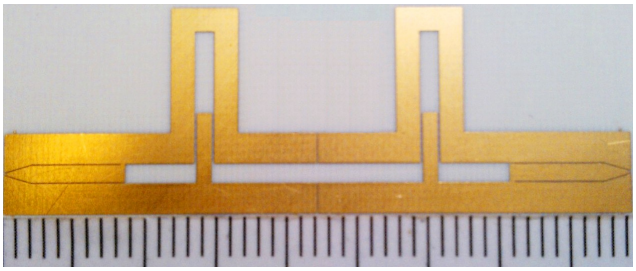

Figure 4.21 – Fabricated second-order multimodal coupled-resonator bandpass filter with reduced-length quarter-wavelength ($\lambda_{0s2}/4$) slotline resonators with slotline-CPW tees (ruler scale in mm).

The filter of Fig.4.21 was measured using GSG probes with a pitch of 250 μm. Fig.4.22 compares the measured S parameters with those obtained from its multimodal circuit model (including transmission-line losses). The minimal insertion loss is 1.55 dB (at 1.52 GHz) , and the measured relative bandwidth is FBW = 0.078.

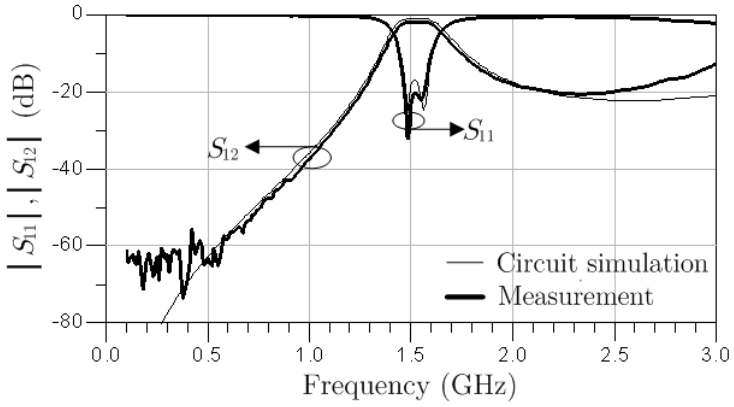

Figure 4.22 – Comparison between measurement and circuit simulation of the filter of Fig. 4.21.

A second-order filter, using the same substrate and transmission line dimensions than that of Fig.4.21, but without slotline-CPW tees for length reduction, has a total length of $2l_r$ = 69.4mm. This means that by using a single slotline-CPW tee per resonator, the length has been reduced approximately 35%.

4.2.2 Reduced-length filter using multiple slotline-CPW tees

In order to reduce the total area of the filter, more reduced-length slotline sections can be used as shown in the second-order filter of Fig. 4.23. This filter uses two pairs of slotline-CPW tees connected in cascade (in total 4 slotline-CPW tees) per resonator. This filter uses slotline inter-digital capacitors at the input and output as immittance inverters. It was fabricated on a Rogers RO4003C substrate, with a relative permittivity ε_R = 3.55 and a thickness h = 1.52 mm. It features a Chebyshev response

with a ripple of 0.2 dB, and a FBW = 0.08 at f_0 = 1.5 GHz. The calculated lengths, at f_0 = 1.5 GHz, of each CPW section are l_e = 4 mm and l_o = 4.1 mm, which represent an insertion phase of 15° per transition, for a total of 60° (including all 4 transitions). The slotlines between cascaded transitions have a slot width s_s = 0.2 mm and strip width w_s = 1.1875 mm.

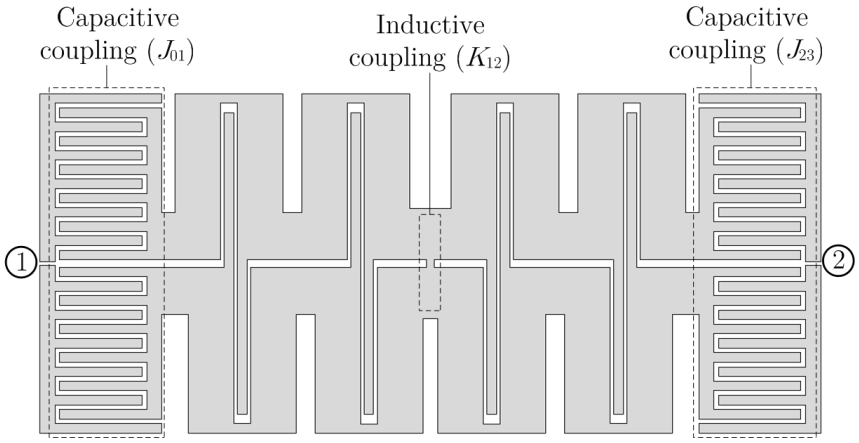

Figure 4.23 – Second-order multimodal coupled-resonator bandpass filter with 4 slotline-CPW Tees per resonator.

The fabricated filter is shown in Fig. 4.24. The area of the filter of Fig. 4.24 is 20.65 mm × 8.95 mm. A slotline filter without slotline-CPW tees for length reduction would have a total length of $2l_r$ = 64mm, thus the filter has been reduced to just 32.2% of the normal length (almost a 68% of length reduction). Compared to the guided wavelength, this filter measures only $0.16\lambda_{0s}$.

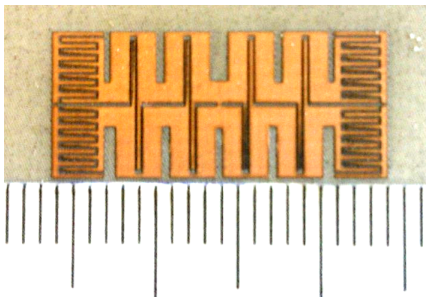

Figure 4.24 – Fabricated second-order multimodal coupled-resonator bandpass filter with 4 slotline-CPW tees per resonator (ruler scale in mm).

The filter of Fig. 4.24 was measured using SG/GS probes with a pitch of 150 μm. Fig. 4.25 compares the measured S parameters with those obtained from its multimodal circuit model (including transmission-line losses). The minimal insertion loss is 2.7 dB (at 1.51 GHz) , and the measured fractional bandwidth is FBW = 0.08 . As can be seen in Fig. 4.25, the measured data agrees with the multimodal circuit modal from 1.1 GHz until 2.1 GHz, whereas the out-of-band response does not. The difference below the passband (from 0.1 GHz to 1.1 GHz), is most probably due to a common-mode excitation in the SG/GS probes. Indeed, it has experimentally been observed that this spurious response largely depends on the measurement set-up (presence and disposition of metallic mechanical supports of the probe station) [25].

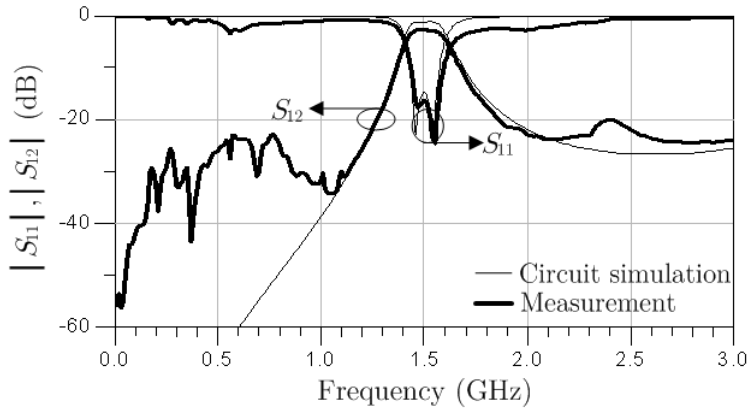

Figure 4.25 – Comparison between measurement and circuit simulation of the filter of Fig. 4.23.

An electromagnetic simulation of the filter of Fig. 4.23 was performed using Agilent Momentum; Fig. 4.26 shows the wide-band comparison with the measured data . As can be seen, the ripples below 1.1 GHz do not appear, but a spike can be seen at 2.3 GHz. This resonance is due to an excitation of a parallel-plate mode in the slotlines with an additional ground plane (the probe station chuck). The first harmonic of the spurious mode can be seen at 4.6 GHz. The propagation of this mode can be avoided by using thicker substrates, or by suspending the filter structure in air with a special holder.

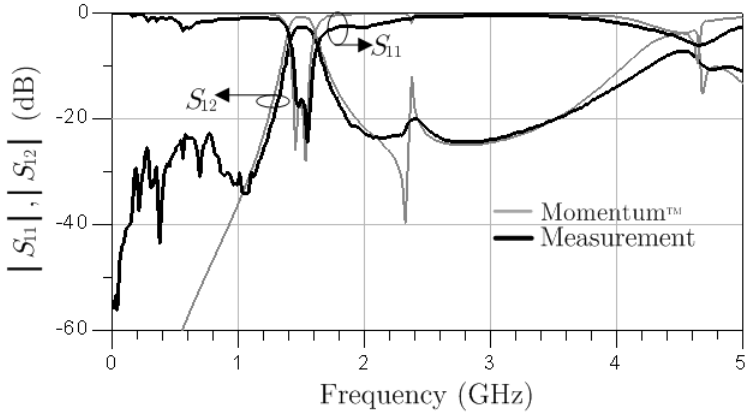

Figure 4.26 – Wide-band comparison between measurement and EM simulation (Agilent Momentum) of the filter of Fig. 4.23.

4.2.3 Filters with slotline-CPW tees as immitance inverters

Fig. 4.27 shows a second-order bandpass filter, that uses inductive couplings at the input and output (K_{12} and K_{23}). The filter uses a double slotline-CPW tee as a central (J_{12}) immitance inverter. The multimodal circuit model of Fig. 4.28 and the design equations presented in Section 2.2.2 were used to design a filter with a Chebyshev response with a ripple of 0.5 dB, and a FBW = 0.1 at f_0 = 1.5 GHz. The filter was fabricated on a Rogers RO4003C substrate, with a relative permittivity ε_R = 3.55 and a thickness h = 1.52 mm.

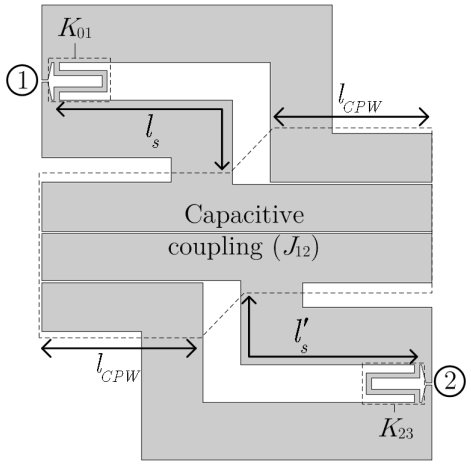

Figure 4.27 – Second-order multimodal bandpass filter with double slotline-CPW tees as immitance inverter.

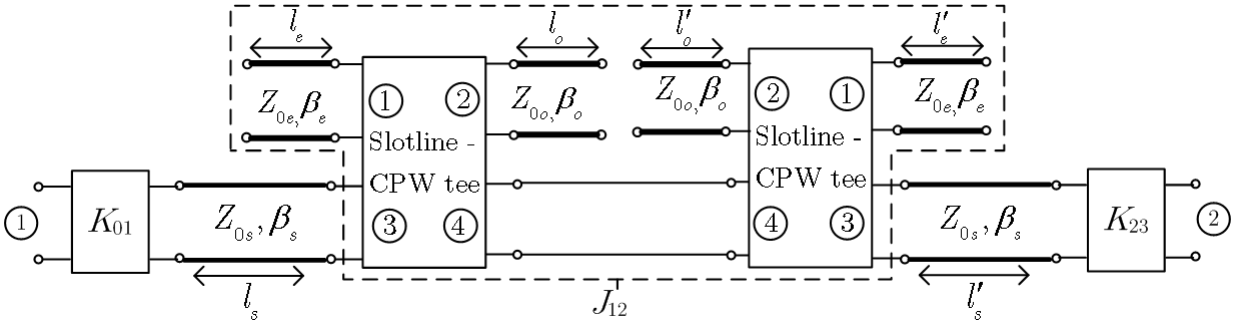

Figure 4.28 – Circuit model of the multimodal bandpass filter with double slotline-CPW tees as immitance inverter of Fig. 4.27.

The dimensions of the filter are shown in Table 4.7. The filter has compact area of 18 mm × 22 mm, or $(\lambda_{0s}/7) \times (\lambda_{0s}/6)$ in terms of the slotline mode.

Length of slotlines, l_s, l'_s	12.6 mm
Length CPW sections (even and odd mode), $l_{CPW} = l_e = l_o = l'_e = l'_o$	7.88 mm
Slotline slot width, s	1.85 mm
CPW central-strip width, w	2.3 mm
CPW gaps, s	0.1 mm
CPW-section ground-plane width, w_g	2.4 mm

Table 4.7 – Dimensions of the filter of Fig. 4.27.

The filter was measured using SG/GS probes. Fig. 4.29 compares its measured S parameters with those obtained from its multimodal circuit model (including transmission-line losses). The minimal insertion loss is 2.2 dB (at 1.53 GHz) , and the measured fractional bandwidth is $FBW = 0.1$. As in the bandpass filter of the previous section, some spikes can be seen below 0.6 GHz, most probably due a common-mode excitation in the SG/GS probes because of the proximity of metallic mechanical supports of the probe station [25].

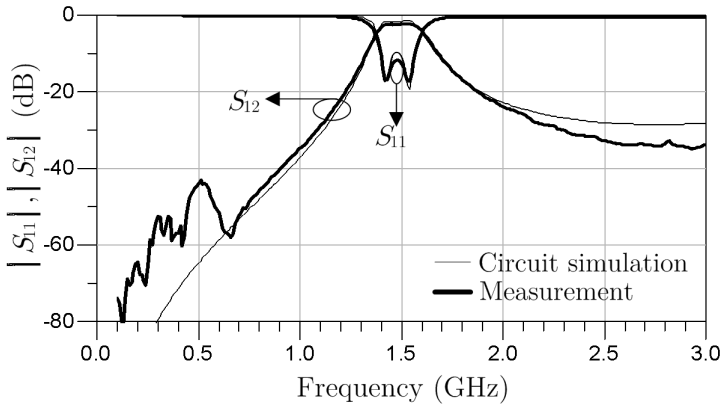

Figure 4.29 – Comparison between measurement and circuit simulation of the filter of Fig. 4.27.

CHAPTER 5

TUNABLE MULTIMODAL BANDPASS FILTERS

Tunable and reconfigurable filters play an important role in the development of next-generation multi-band communication systems, because they can reduce the overall size. In many cases, these components have to be compact and energy-efficient.

This chapter introduces five topologies of reconfigurable and tunable filters using active devices (PIN diodes and varactors) and RF-MEMS. In section 5.1, a PIN-diode bandwidth-reconfigurable filter, using asymmetrically-loaded resonators is presented. Sections 5.2 and 5.3 show two topologies of capacitive-loaded filters (using varactors and RF-MEMS respectively). In Section 5.4, a K-band RF-MEMS bandwidth-reconfigurable filter is demonstrated.

Finally, section 5.5 shows a frequency-reconfigurable filter based on RF-MEMS switchable air-bridges (SABs). These topologies demonstrate a relevant feature of multimodal filters: easy reconfiguration.

5.1 A bandwidth-reconfigurable bandpass filter

Fig. 5.1 shows a second-order bandpass filter with reconfigurable bandwidth, based on the filter topology described in Chapter 4 (Section 4.1.1). In this filter, the asymmetric-short-circuit positions of each resonator can be easily changed using PIN diodes as shown in Fig. 5.1. The design goal is a reconfigurable Butterworth filter that changes its bandwidth from $FBW = 0.15$ (state 1) to $FBW = 0.2$ (state 2), maintaining a central frequency of $f_0 = 2$ GHz . The chosen diodes (Avago HPND-4028) exhibit a low capacitance ($C_d = 0.045$ pF), low forward resistance ($R_s = 3\ \Omega$), and small size (0.65 mm × 0.24 mm). In state 1, diodes D_1 and D_3 are forward-biased, and diodes D_2 and D_4 are reverse-biased. In state 2, these biases are exchanged.

The chosen substrate (Rogers RO3003) has a relative permittivity $\varepsilon_r = 3.02$, $\tan\delta = 0.0013$, thickness of 1.52 mm , and copper-layer thickness of 35 μm. In the design, a uniform CPW has been used with central-strip width of 2.8 mm, gap of 0.16 mm and ground-plane width of 5.6 mm. Therefore, the three inverters are equal ($Z_{0e} = 1/Y_{0e1} = 1/Y_{0e2} = 1/Y_{0e3}$) and the parameters for the length Δl (see Chapter 4, Section 4.11) are equal to those used for the even mode. For the chosen dimensions, $Z_{0e} = 50\ \Omega$ and $Z_{0o} = 110\ \Omega$.

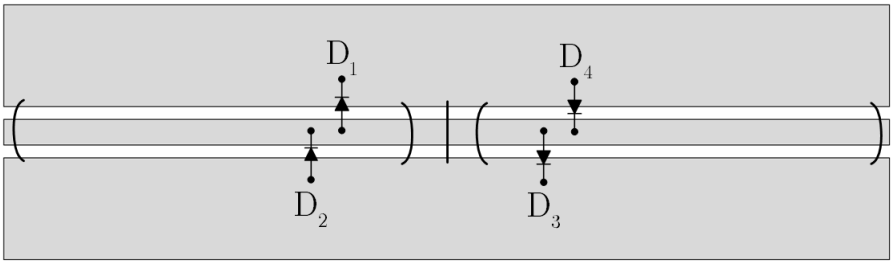

Figure 5.1 – PIN diode positions for the reconfigurable filter.

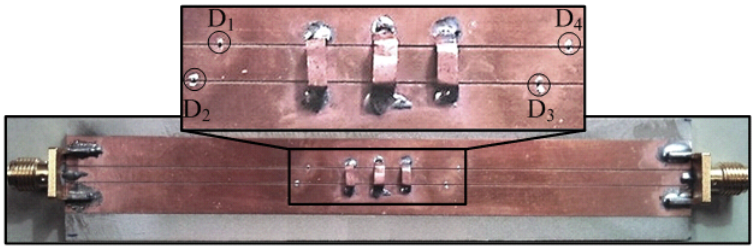

Figure 5.2 – Fabricated reconfigurable multimodal filter.

The assembled filter is shown in Fig. 5.2. In order to measure the filter, a pair of SMA coaxial connectors has been used. Since the coaxial connectors act as a short circuit for the CPW odd mode, there is no need to add additional air bridges at the input and output of the filter. Air bridges were fabricated using a copper film with a thickness of 0.035 mm and width of 1.5 mm. An additional bridge at the center of the structure was added to minimize the parasitic self-inductance. The circuit area without SMA connectors is 116 mm × 14 mm ($1.1\lambda_e \times 0.2\lambda_e$). The diodes were polarized using external bias tees, with a bias current of 20 mA. A comparison between simulated and measured results is shown in Fig. 5.3. The simulated results were obtained using the multimodal circuit model of Fig. 4.2, in which FGCPW (finite-ground CPW) losses and diode parasitics were taken into account. A shift in the central frequency (60 MHz) can be observed in both measured states; this is due to fabrication process errors. Also, a small difference is observed between simulated and measured FBW and insertion loss (IL). This can be attributed to diode losses, which are higher than expected.

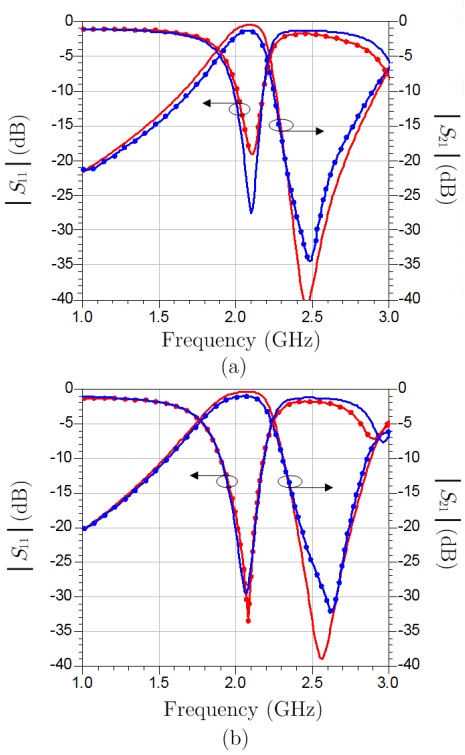

Figure 5.3 – Frequency response of the fabricated tunable filter. (a) State 1. (b) State 2. Continuous line corresponds to the simulated response (multimodal circuit) and dotted line corresponds to measured data.

Table 5.1 summarizes the calculated electrical lengths, the measured insertion loss (IL) and FBW for each state of the fabricated tunable filter. To evaluate the contribution of the PIN diodes to the overall loss of the filter, a third state (when all diodes are off and therefore the structure behaves like a 50-Ω line) is also considered in Table 5.1.

State	FBW(%)	$\theta_1 = \theta_1'(^\circ)$	$\theta_2 = \theta_2'(^\circ)$	IL@2.06 GHz (dB)
1	14	146	34	1.39
2	21	139	41	1.1
3	N/A	N/A	N/A	0.35

Table 5.1 – Measured parameters of the reconfigurable multimodal bandpass filter.

5.2 A frequency-tunable filter with quasi-constant bandwidth

It is well known that frequency-tunable filters can be obtained by using capacitive-loaded resonators [29, 60, 61]. In a conventional CPW even-mode varactor-loaded filter, two equal devices per resonator are needed [61, 62] since the CPW even-mode resonator must be symmetrically-loaded with respect to the central strip in order to avoid odd-mode generation, which is, in this case, undesired. However, an advantage of using the odd-mode for the reconfiguration process (as proposed here) is that only one varactor is needed for each resonator (or inverter), as shown in Fig. 5.4. In it, the varactor is connected to the CPW ground planes, interacting thus with the odd mode while leaving the even mode unaffected.

The circuit of Fig. 5.4 can be viewed either as a varactor-loaded odd-mode–slotline resonator (from the air bridge to the inductive coupling), or from a circuit point of view as a variable multimodal

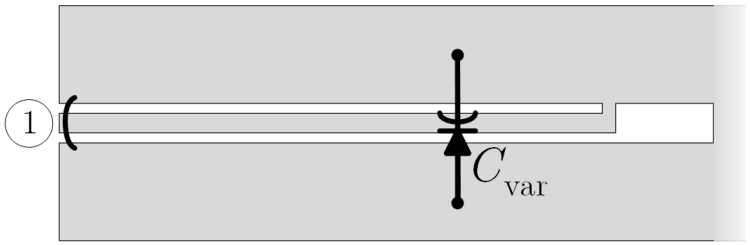

Figure 5.4 – Capacitively-loaded odd-mode–slotline resonator (or inverter).

inverter (since the varactor capacitance C_{var} modifies Y_{Lo1}) with $l_{s2} < 0$, followed by a $\lambda_{0s2}/2$ slotline resonator. From the first point of view, it is apparent that its resonance frequency will decrease with an increasing C_{var}. From the second point of view, it can be rigorously modeled using the circuit model shown in Fig. 5.5 , which is a modification of that of Fig. 4.6(a). In it, the varactor-loaded odd-mode–slotline resonator is also apparent, with length $l_r = l_{o1A} + l_{o1B} + l_{s2} + \lambda_{0s2}/2 \approxeq \lambda_{0s2}/2$. By tuning C_{var}, both K_{01} and l_{s2} will change (according to 2.14 and 2.15). The change in K_{01} will result in a change in the filter FBW. The change in l_{s2} modifies l_r, and together with the C_{var} variation, results in a change of the resonance frequency. A parametric study can be performed using the circuit model of Fig. 5.5 to select an adequate position for the varactor, that yields a good trade-off between a large tuning range and a small variation of the FBW. Another effect of tuning C_{var} is a change in the frequency of the transmission zero discussed in section 4.1.2 produced whenever $\beta_{s2}(l_{s2} + \lambda_{0s2}/2)$ is a multiple of π or Y_{Lo1} is a short circuit.

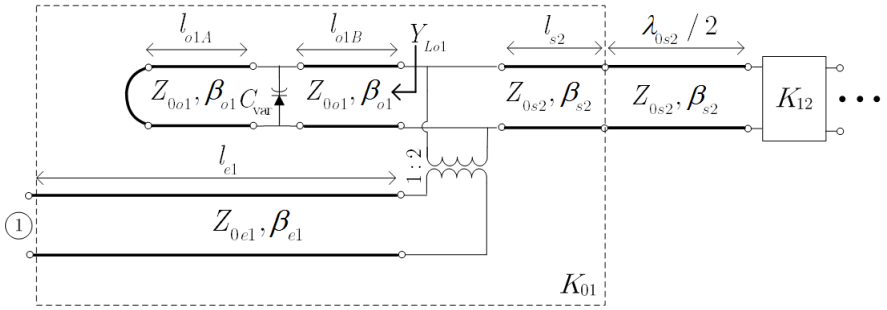

Figure 5.5 – Circuit model for the capacitive-loaded odd-mode–slotline resonator (or inverter) of Fig. 5.4.

The equivalent circuit of Fig. 5.5 can be integrated in a complete circuit model of a tunable filter, and used to assist in its design. To achieve this, the unloaded filter has to be designed at a given frequency f_0 using the procedure of Section 4.1.2. Then, by using its complete multimodal model, a parametric study can be carried out so as to determine what changes in lengths and inner coupling give the best performance for all the C_{var} intended values. The multimodal model of the filter allows a fast tuning of all the relevant parameters, which would be much more cumbersome to do by parametric variations using an electromagnetic simulator. As a numerical example, Fig. 5.6 shows the simulated response of a second-order bandpass filter with center frequency f_0 = 1.4 GHz (when C_{var} = 0) and FBW = 0.1. As the capacitive load increases, the center frequency, as well as the transmission zero above it, shift down, maintaining a quasi-constant bandwidth. The multimodal circuit model shows that for a maximal capacitance C_{var} = 1.4 pF, a frequency shift of 0.28 GHz can be obtained.

A reconfigurable varactor-tuned second-order bandpass filter with half-wavelength slotline resonators was fabricated on a Rogers 4350 substrate with a dielectric thickness of 1.52 mm (Fig. 5.7). The varactors (MACOM MA46580 beam-lead varactors) are mounted on small printed circuit boards (PCBs) containing DC blocks and RF chokes for appropriate biasing (see Fig. 5.8). The filter area is 12.5 cm × 1.15 cm. As in the previous example, the initial design parameters (when C_{var} = 0 pF) were a Butterworth response with FBW = 0.1 and f_0 = 1.4 GHz. The varactor position, as well as the optimal feeding point and coupling length, were parametrically investigated using the multimodal circuit

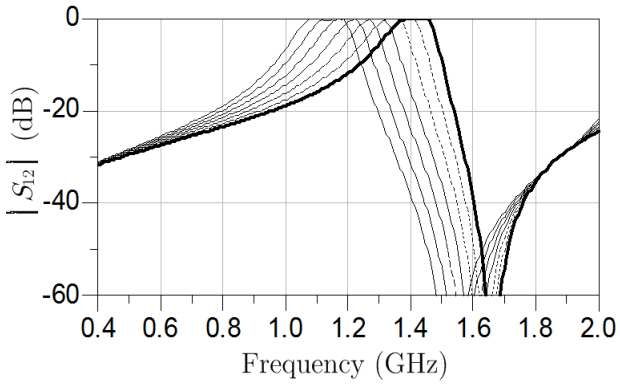

Figure 5.6 – Ideal frequency response of a capacitively-loaded second-order multimodal filter with an additional transmission zero above the pass band and quasi-constant bandwidth.

model of Fig. 5.5. Table 5.2 summarizes the obtained relevant filter parameters. The measured *S* parameters of the tunable filter are shown in Fig. 5.9. The filter can be tuned from 1.002 GHz to 1.374 GHz. It exhibits quasi-constant 3-dB bandwidth, which varies from 121 MHz to 135 MHz over the tuning range. The measured insertion loss varies from 2.17 to 3.45 dB. It is mainly caused by the intrinsic resistance of the varactor at low bias voltages. The in-band return loss is better than 20 dB over the entire tuning frequency range. Table 5.3 lists the filter results for several bias voltages.

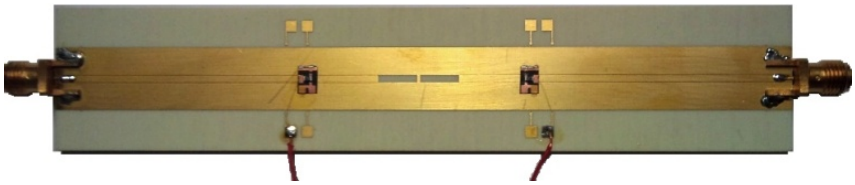

Figure 5.7 – Fabricated reconfigurable second-order bandpass filter with half-wavelength slotline resonators.

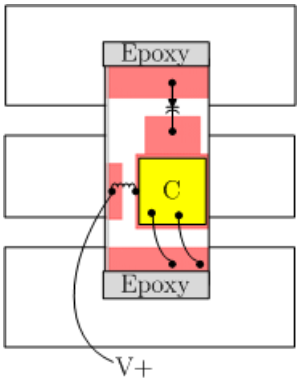

Figure 5.8 – Schematic of the PCB (used in the filter of Fig. 5.7) containing the varactor diode, DC block capacitor (in yellow) and RF chokes for appropriate biasing. The PCB is connected between the ground planes of the CPW, by using conductive epoxy. Gold bonding wires are used to connect the PCB with the bias pads and also to connect the capacitor.

l_{o1}, l'_{o1}	55.5 mm
Length of first slotline section, l_{o1A}	42 mm
Length of first slotline section, l_{o1B}	13.5 mm
l_{s2}, l'_{s2}	-51.9 mm
$\lambda_{0s2}/2$	63 mm
l_r, l'_r	60.36 mm
Coupling length (K_{12} inverter)	0.54 mm

Table 5.2 – Dimensions of the filter of Fig. 5.7.

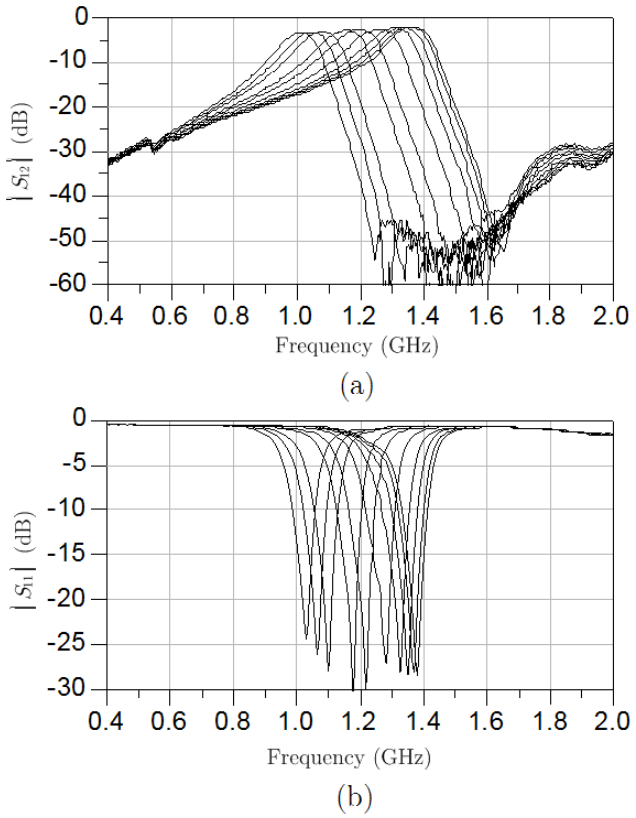

Figure 5.9 – Measured response of the filter of Fig. 5.7. (a) $|S_{21}|$. (b) $|S_{11}|$.

5.3 RF-MEMS half-wavelength filter with reconfigurable frequency

Fig. 5.10 shows the layout of a RF-MEMS capacitive-loaded slotline-resonator filter that uses reconfigurable multimodal immittance inverters (MIIs) as first and last inverters. Its circuit model is shown in Fig. 5.11. The MIIs perform an immittance inversion between the CPW even mode of the filter ports and the slotline mode of the resonators by means of a multimodal CPW section of length l_{o1} (where the CPW even and odd modes propagate simultaneously). Althought the filter of Fig. 5.10 is similar to the filter presented in Section 5.2, in this filter the input and output MIIS are not affected by the capacitive loads. Therefore, the input and output couplig (K_{01} and K_{23}) are constant for every state.

Reverse bias (V)	f_0 (GHz)	3-dB BW (GHz)	3-dB FBW (%)	IL (dB)
18	1.374	0.135	0.098	2.17
10	1.358	0.134	0.098	2.17
8	1.346	0.133	0.099	2.19
6	1.326	0.133	0.1	2.24
4.5	1.298	0.136	0.104	2.33
3	1.247	0.137	0.11	2.5
2	1.188	0.135	0.114	2.55
1.5	1.144	0.135	0.118	2.73
0.7	1.072	0.128	0.12	3.11
0.3	1.038	0.124	0.12	3.24
0	1.002	0.121	0.121	3.45

Table 5.3 – Summary of the measured parameters of filter of Fig. 5.7.

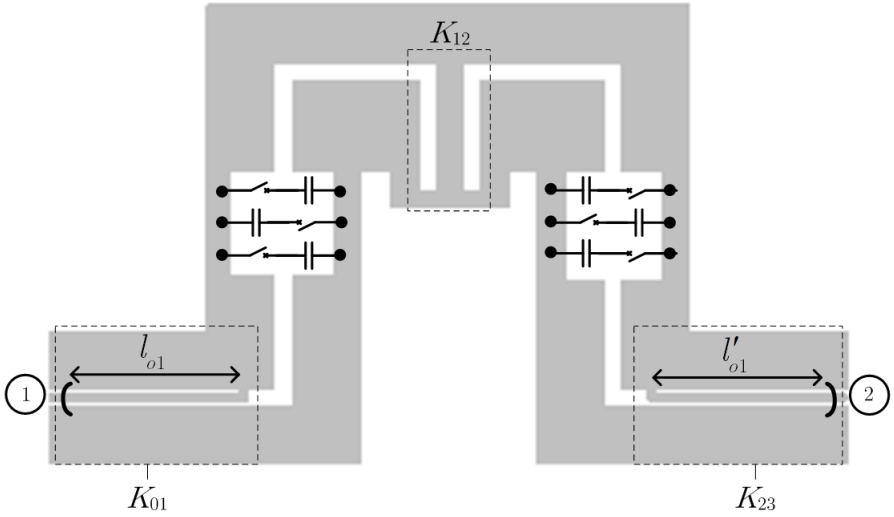

Figure 5.10 – Layout of the fabricated fourth-order bandpass filter with quarter-wavelength slotline resonators.

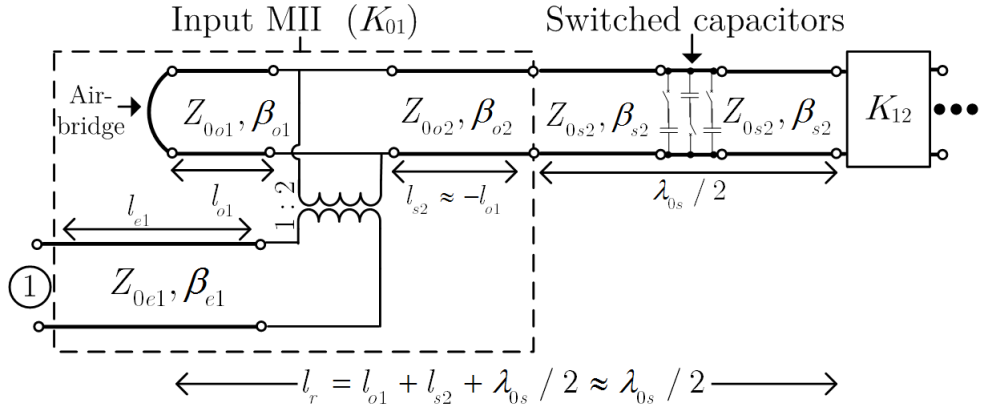

Figure 5.11 – Circuit model of a frequency-reconfigurable filter using switched capacitor banks.

The length l_{s2} can always be chosen to be negative. Since $l_{s2} \approx -l_{o1}$, the resonator lengths are $l_r \approx \lambda_{0s}/2$. Subscripts e, o and s refer, respectively, to the CPW even and odd modes and the slotline mode.

CPW Gap/Strip width (μm)	20/50
70Ω slotline width (μm)	80
$l_{o1} = l'_{o1}$ (μm)	870
l_r(mm)	4.47
Total filter area (mm^2)	4.9×2.9

Table 5.4 – Dimensions of the fabricated filter of Fig. 5.12.

Using the theory presented in Chapter 2 and Chapter 4, a reconfigurable filter can be designed for a given response at the highest frequency (state 000), taking into account the off-state capacitance (10 fF) of the RF-MEMS switched capacitors. The fabricated filter is shown in Fig. 5.12, it was fabricated on a high-resistivity (5 kΩ·cm) silicon substrate, with a permittivity ε_r =11.9 and thickness h = 200 μm, using the integrated RF-MEMS process from FBK. The RF-MEMS switched capacitors have the same characteristics than the ones used in the switched capacitor bank presented in Chapter 3 (Section 3.1.5).

The chosen even-mode and odd-mode characteristic impedances are Z_{0e} = 50 Ω and Z_{0o} = Z_{0s} = 70 Ω, respectively. The additional characteristic parameters of the transmission lines, such as the phase constants (β_e, β_o, and β_s) and losses were obtained as described in [19]. Table 5.4 summarizes the relevant filter dimensions.

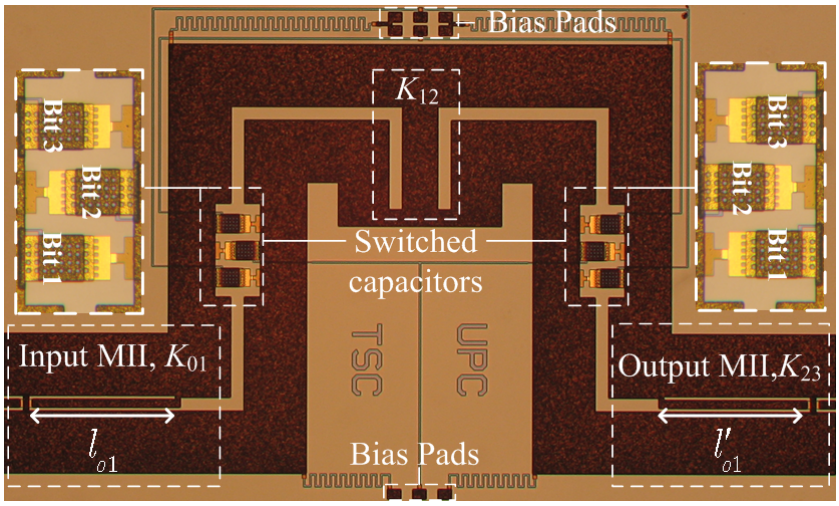

Figure 5.12 – Fabricated frequency-reconfigurable second-order half-wavelength filter using MIIs and switched capacitors.

The simulated response of the circuit model and measured S parameters for all states are shown in Fig. 5.13 (a) and Fig. 5.13(b), showing a very good agreement. As can be seen, the losses of the transmission lines have been included in the circuit model. For state 000, the expected insertion loss is 4 dB for the considered substrate, i.e. a 5-kΩ·cm high-resistivity silicon with permittivity ε_r = 11.9 and thickness h= 200 μm.

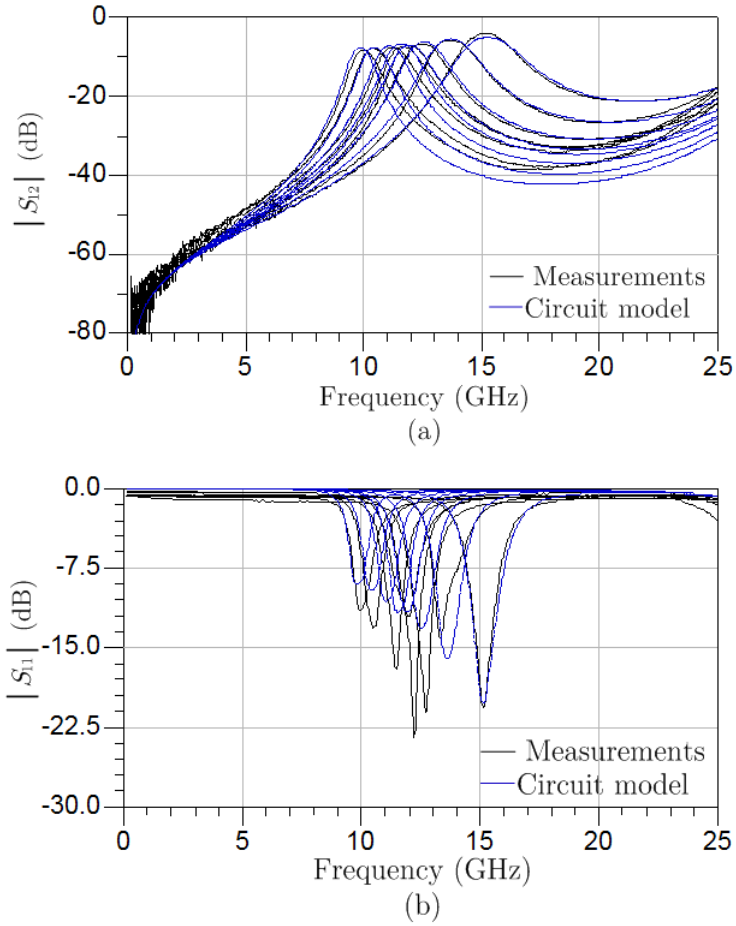

Figure 5.13 – Comparison between measured S-parameters and circuit model simulations. (a) S_{12}. (b) S_{11}.

Table 5.5 shows the measured parameters for each state. Insertion loss can be reduced by using silicon substrates with higher resistivity or quartz substrates [60, 63]. Since the contact resistance R_C of the cantilever switches has a direct impact on the filter insertion loss [60], it should be reduced by increasing the contact area or by including additional switches in parallel to each capacitive load. Furthermore, to keep a constant bandwidth (and thus, similar insertion loss level for each state), a reconfigurable version of the MIIs (such as that used in the tunable filter proposed in section 5.2) could be used.

The linearity of the filter has been measured by plotting the output power versus input power in the 011 state (f_0 = 10.44 GHz). Due to power limitations in the measurement setup, it was not possible to reach the 1dB compression point; however, it was found that an input power of 1.45 W (31.64 dBm) can be handled without any degradation in the response of the filter.

5.4 RF-MEMS half-wavelength filter with reconfigurable bandwidth

Fig. 5.14 shows the scheme of a two-state reconfigurable-bandwidth second-order half-wavelength slotline-resonator filter that uses reconfigurable MIIs as first and last inverters. A MII can be easily reconfigured by replacing, as in Fig. 5.14, its asymmetric upper-CPW-slot shunt short-circuit with several switches to shift the short-circuit position, thus changing the lengths l_{o1}, l_{e2}, and l_{s2} which control the inverter constant, as demonstrated in Chapter 2. Then, it is possible to obtain FBW reconfiguration and maintain the same filter response by simultaneously reconfiguring both the input and output MIIs and the inter-resonator coupling K_{12}. The reconfigurable filter of Fig. 5.14 can be modelled as shown in Fig. 5.15. Subscripts e, o and s refer, respectively, to the even, odd and slotline

C (fF)	State	f_0 (GHz)	3-dB FBW (%)	IL (dB)
10	000	15.22	0.122	4.07
51.5	100	13.75	0.121	5.87
97	010	12.52	0.109	6.54
127.5	001	11.98	0.102	7.09
148.5	110	11.72	0.108	7.3
179	101	11.29	0.103	7.5
224.5	011	10.44	0.98	7.85
276	111	10.04	0.96	8.29

Table 5.5 – Summary of the measured parameters of filter of Fig. 5.12.

modes. The length l_{S2} can always be chosen negative (if so, $l_{s2} \approx -l_{o1}$) and therefore, as it is embedded in the physical slotline, the resonator lengths are $l_r \approx \lambda_{0s}/2$.

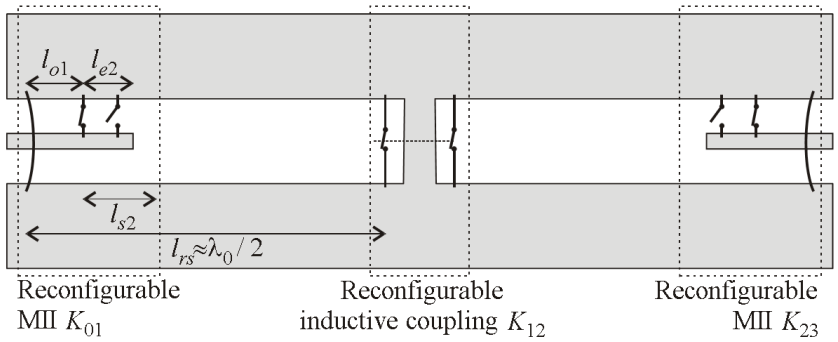

Figure 5.14 – Reconfigurable-bandwidth second-order half-wavelength slotline-resonator filter using MIIs.

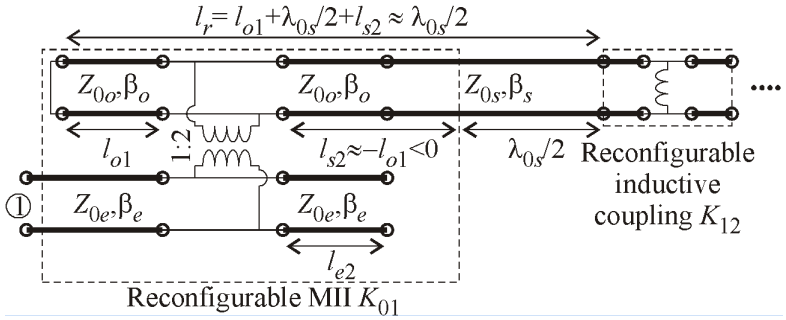

Figure 5.15 – Circuit model for the reconfigurable filter of Fig. 5.14.

Fig. 5.16 shows a reconfigurable-bandwidth second-order Butterworth filter designed according to the principles described above, with a centre frequency f_0 = 18.8 GHz and FBW = 0.08 (state 1) or FBW = 0.04 (state 2). The filter FBW is reconfigured using five electrostatic RF-MEMS ohmic-contact cantilever switches [64], two in either MII (Fig. 5.17(a)) and one in the inter-resonator inductive coupling (Fig. 5.17(b)). Each switch can be modeled as a shunt impedance Z_S. In the down-state Z_S is composed by a contact resistance R_{ON} = 1.6 Ω in series with an inductance L_c = 112.5 pH, whereas in the up-state Z_S is a capacitance C_{OFF} = 38 fF. The switches, with an air-gap of 3 μm, have a low pull-in voltage of 15 V. The filter was fabricated on a quartz substrate (ε_r = 3.8) using the RF-MEMS

fabrication process from FBK described in [5]. The area of the filter, including bias lines, is 4.40 mm × 4.44 mm.

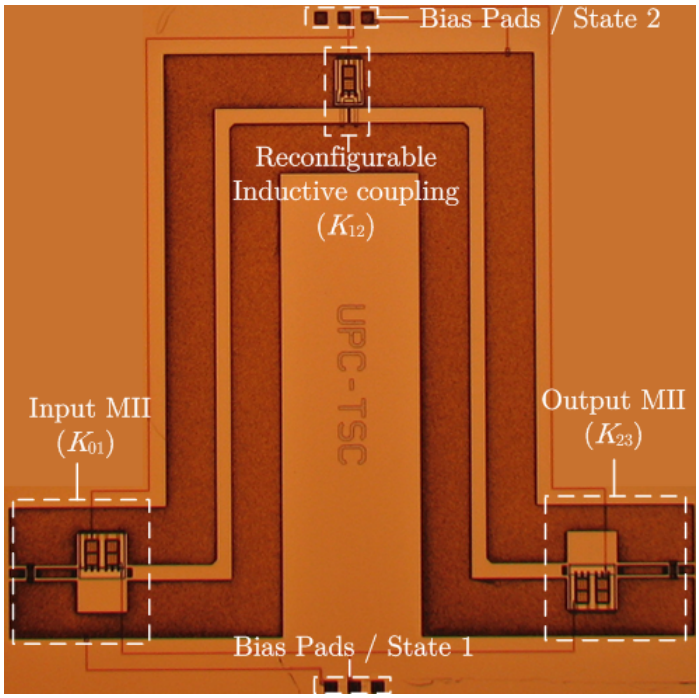

Figure 5.16 – Implemented reconfigurable-bandwidth bandpass filter.

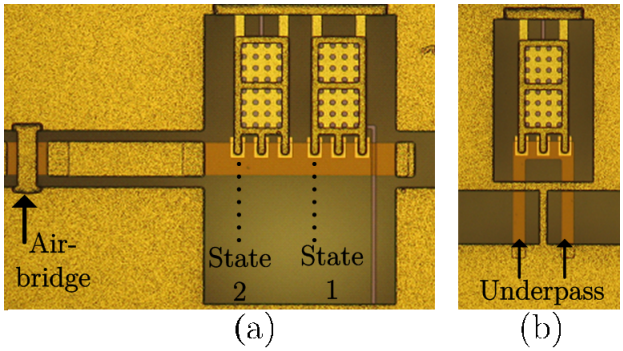

Figure 5.17 – RF-MEMS reconfigurable sections of the fabricated filter. (a) Reconfigurable CPW-slotline transition (input). (b) Reconfigurable inter-resonator coupling.

In state 1 (FBW = 0.08), the inner switches of both MIIs (Fig. 5.17 (a)) are actuated (down-state), whereas the switch of the central inter-resonator coupling K_{12} (Fig. 5.17 (b)) is not actuated (up-state), and thus its coupling is determined by the fixed short-circuit. In state 2 (FBW = 0.04), the outer switches of the MIIs and that of the central inductive coupling are biased. In this state, the switch in (Fig. 5.17 (b)) contacts an underpass metallization, thus reducing the inductance of the coupling. The required widths of the underpass lines were obtained from electromagnetic simulations. The filter was designed in two steps. First, an initial design of a two-state filter (with the required FBW) featuring ideal switches was performed using the circuit model of Fig. 5.15 and the theory in presented in Chapter 2 and Chapter 4. The chosen characteristic impedances were Z_{0e} = 65 Ω and $Z_{0o} = Z_{0s}$ = 110 Ω. The dimensions of the required inter-resonator coupling were obtained by the pole-splitting method [41]. Table 5.8 shows the required normalized K_{12} and electrical lengths of the MIIs, (notice that since θ_{s2} is negative, $|\theta_{s2} = \beta_o l_{s2}| \approx |\theta_{o1} = \beta_o l_{o1}|$), then, the circuit model of the RF-MEMS switches was included into the circuit model of Fig. 5.15, to optimize the filter dimensions.

	Initial design parameters			Measured filter parameters		
State	$\theta_{o1}(°)$	$\theta_{s2}(°)$	$\overline{K_{12}}$	3-dB FBW	f_0 (GHz)	IL (dB)
1	27.7	-26.8	0.089	0.082	18.8	3.7
2	19.1	-18.8	0.044	0.043	18.9	5.2

Table 5.6 – Initial design parameters and measured performance of the designed filter.

Fig. 5.18 shows the measured responses for both states of the reconfigurable-bandwidth filter, along with those predicted by the circuit simulation, showing a good agreement. The main filter parameters are summarized in Table 5.8. The 3-dB FBW varies from 0.082 down to 0.043, which represents a change of 90%, while maintaining a Butterworth frequency response. The measured insertion loss (IL) in both states is in the range expected for circuits featuring low-actuation-voltage ohmic-switches, which provide moderate values of R_{ON}. As expected, the insertion loss of state 2 is higher than that of state 1, since the FBW decreases to roughly a half of that of state 1 [41].

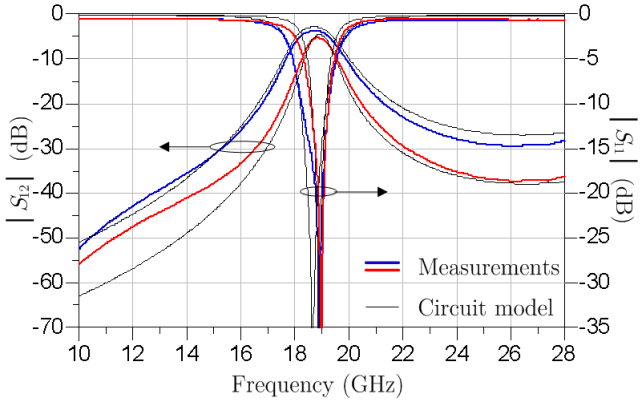

Figure 5.18 – Comparison between the measured S parameters of the reconfigurable-bandwidth half-wavelength second-order bandpass filter and those predicted by the circuit model. Blue traces correspond to state 1, and red ones to state 2.

5.5 RF-MEMS quarter-wavelength reconfigurable filter based on SABs

Fig. 5.19 shows the scheme of a quarter-wavelength slotline-resonator second-order bandpass filter that uses reconfigurable MIIs as first and last inverters. Its circuit model is shown in Fig. 5.20. The MIIs can be reconfigured by changing the position of their odd-mode short-circuit (the air bridge) by means of a switchable air-bridge (SAB), as shown in Fig. 5.19 and Fig. 5.20. As a result, the odd mode length l_{o1} will be shortened and, since l_{o1} is part of the physical resonator of length l_r (Fig. 5.20), l_r will be shortened, producing a frequency shift (increase) in the filter central frequency.

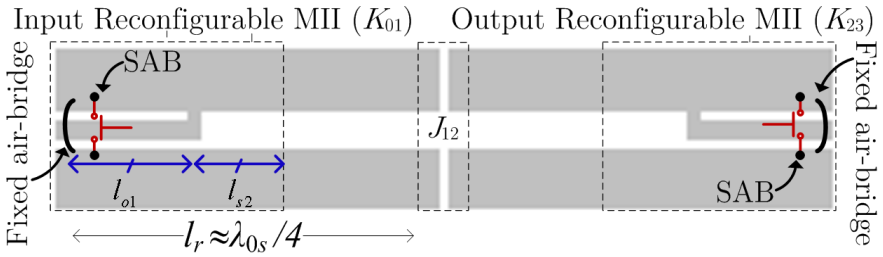

Figure 5.19 – Frequency-reconfigurable second-order quarter-wavelength filter using MIIs and SABs.

Using the circuit model of Fig. 5.20 and the theory presented in Chapter 2 and Chapter 4, a reconfigurable filter can be designed for a given response at the lowest frequency (state 1), and the optimal

position of the SAB can be parametrically investigated to give an appropriate second (highest) frequency state (state 2). This optimal position is selected to maintain the 3-dB FBW as constant as possible by keeping the change in the ratio l_{o1}/l_r as small as possible (since the FBW is a function of l_{o1}/l_r, as demonstrated in Chapter 2).

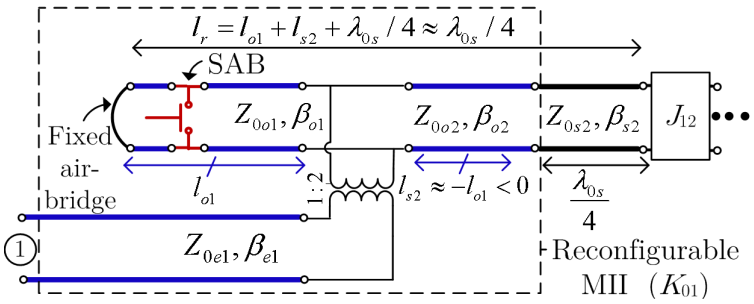

Figure 5.20 – Circuit model of a frequency-reconfigurable second-order quarter-wavelength filter using MIIs and SABs.

The effect of the intrinsic inductance and contact resistance of the SAB should be estimated by measurement or by electromagnetic simulation, and then should be taken into account in the circuit simulation. Using this approach, a quarter-wavelength slotline-resonator second-order bandpass filter with reconfigurable central frequency has been designed using the FBK RF-MEMS integrated technology [5].The filter was fabricated on a 5-kΩ·cm high-resistivity silicon with a permittivity ε_r = 11.9 and thickness h = 200 μm. The chosen even-mode and odd-mode characteristic impedances are Z_{0e} = 50 Ω and Z_{0o} = Z_{0s} = 78 Ω, respectively. The additional characteristic parameters of the transmission lines, such as the phase constants (β_e, β_o, and β_s) and losses were obtained as described in [19]. The simulated response of the circuit model for both states is shown in Fig. 5.21. The losses of the transmission lines have been included in the circuit model.

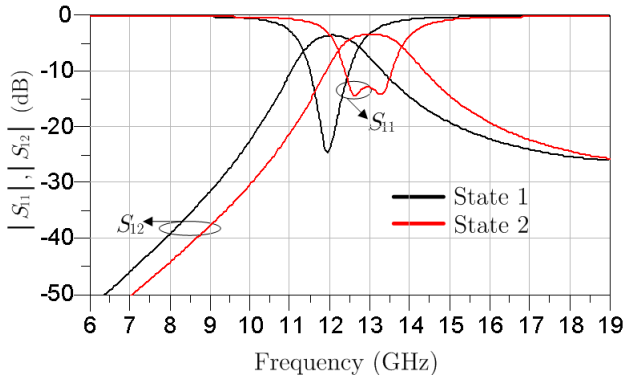

Figure 5.21 – Simulated S parameters of the frequency-reconfigurable quarter-wavelength second-order filter.

The expected insertion loss (IL) is around 3.7 dB for the considered substrate. Table I shows the filter main parameters for a center frequency f_{01} = 12 GHz and a Butterworth response (state 1).

In state 2, the position of the odd-mode short-circuit (air-bridge) will be changed using SABs, to reduce the length of the odd mode resonators (to increase the center frequency to f_{02} = 13 GHz). Since the inter-resonator coupling J_{12} does not change, the response for this second state will not be of a Butterworth-type.

	Initial design parameters		Simulated filter parameters		
State	$\theta_{o1}(°)$	$\overline{K_{12}}$	3-dB FBW	f_0 (GHz)	IL (dB)
1	24.7	15.005	0.12	12	3.7
2	22.5	15.005	0.12	13	3.6

Table 5.7 – Parameters of the frequency-reconfigurable filter.

Fig. 5.22 shows the second-order bandpass filter with reconfigurable center frequency designed according to the principles described above. The area of the filter, including bias lines, is 4.97 mm × 0.74 mm.

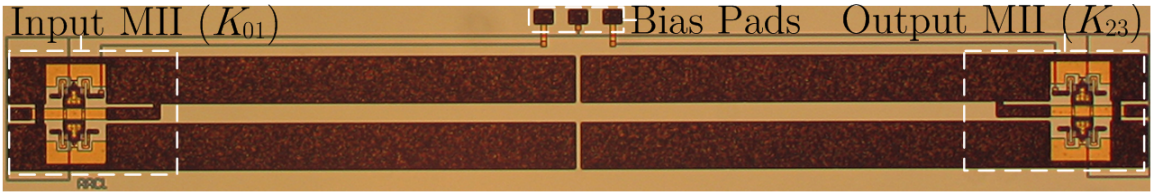

Figure 5.22 – Fabricated RF-MEMS frequency-reconfigurable filter using SABs.

Fig. 5.23 shows a close-up of the input MII. When the SAB is in the up-state, the length l_{o1} is defined by the position of the fixed air-bridge and the asymmetrical short-circuit. When the SAB is in the down state, l_{o1} is defined by the position of the SAB ohmic contacts and the asymmetrical short-circuit. Then, when a bias voltage V_{bias} higher than V_{pi} is applied simultaneously to both SABs (input and output), there will be a shift in the central frequency and a change in the input and output couplings.

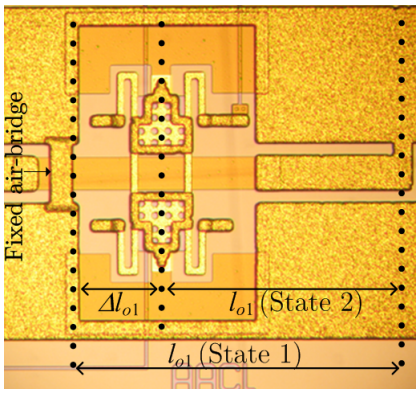

Figure 5.23 – Input MII with an RF-MEMS SAB.

Table II shows the dimensions of the reconfigurable second-order quarter-wavelength filter. The difference between the length l_{o1} of state 1 and the one of state 2 is Δl_{o1} = 140 μm.

l_{o1}, State 1	l_{o1}, State 2	Δl_{o1}	l_r, State 1	l_r, State 2	Coupling gap
490 μm	350 μm	140 μm	2310 μm	2170 μm	25 μm

Table 5.8 – Dimensions of the frequency-reconfigurable filter.

Fig. 5.24 and Fig. 5.25 show and compare the measured and simulated responses for both states of the reconfigurable filter. The bias voltage applied to the SABs (state 2) was V_{bias} = 60 V. The measured IL for both states is lower than 4.7 dB and the measured FBW is only 0.02 higher than the expected

by the circuit simulation, but the same 3-dB FBW is maintained in both states as anticipated. The IL levels are in the expected range for planar filter topologies using 5-kΩ·cm high-resistivity substrates. As show in Fig. 5.25, the wideband response of the circuit simulation agress with the measurements, validating the multimodal circuit model. The small discrepancies seen above 30 GHz are attributed to the modelling of the capacitive coupling (performed at f_{01}), which ceases to be accurate above this frequency.

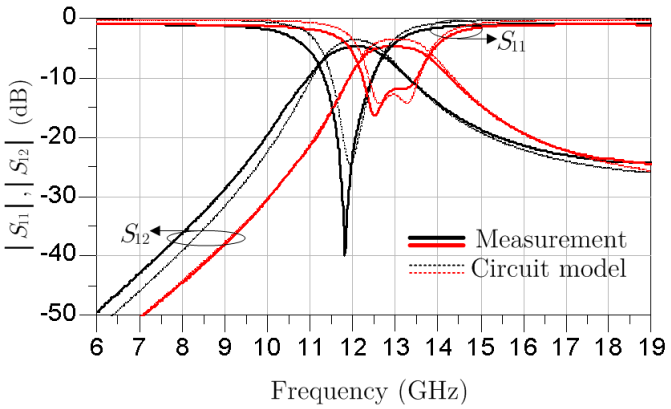

Figure 5.24 – Comparison between the measured S parameters of the frequency-reconfigurable filter and those predicted by the circuit model. Black traces correspond to state 1, and red ones to state 2.

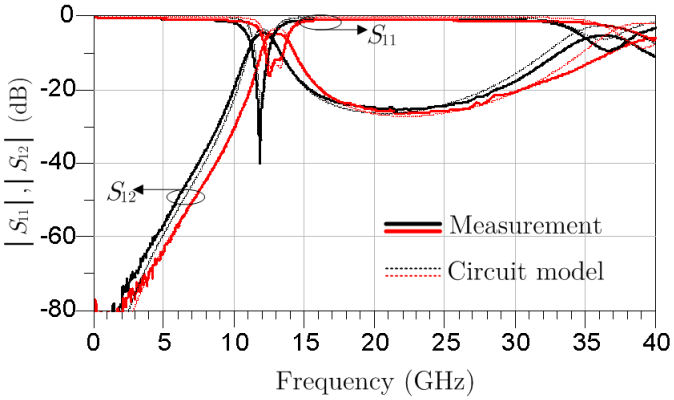

Figure 5.25 – Wideband comparison between the measured S parameters of the frequency-reconfigurable filter and those predicted by the circuit model. As above, black traces correspond to state 1, and red ones to state 2.

CHAPTER 6

MULTIMODAL BANDSTOP FILTERS

This chapter presents the design and validation of two uniplanar multimodal band-stop filters, based on the band-stop resonators described in Chapter 2. The first filter topology uses CPW even-mode quarter-wavelength resonators, which can be modeled using the circuit model for CPW circuits with asymmetric shunt impedances proposed in [16], as demonstrated in Chapter 2 (section 2.1.3). The second topology uses resonators based on CPW-asymmetric series impedances, that can modeled using the multimodal equivalent circuit proposed in [15], as demonstrated in Chapter 2 (section 2.3.1). The overall area of this second topology structure is considerably reduced, in comparison to ordinary CPW symmetrical structures.

6.1 Quarter-wavelength band-stop filters

Fig. 6.1 shows the topology of a second-order multimodal band-stop filter with quarter-wavelength ($\lambda_{0e}/4$) even-mode resonators. As demonstrated in Chapter 2 (section 2.1.3) a single even-mode stub can be used to produce a transmission zero in an odd-mode structure. The equivalent circuit model of the second-order band-stop filter is shown in Fig. 6.2.

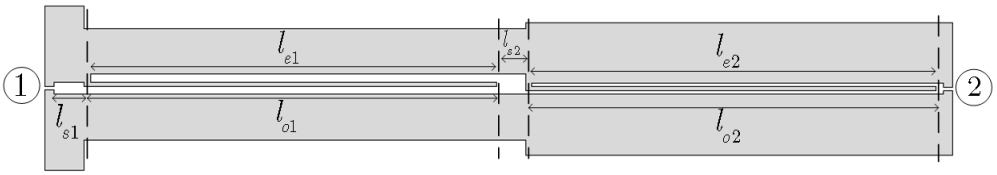

Figure 6.1 – Second-order multimodal band-stop filter with quarter-wavelength ($\lambda_{0e}/4$) even-mode resonators.

As can be seen in Fig. 6.2, the CPW odd-mode immitance inverter (which is the spacing between the asymmetric short-circuits, $l_{o1}+l_{s2} \approx \lambda_{0o}/4$), is embedded in the first CPW section; therefore the overall area is reduced compared with traditional CPW filters (using straight stubs), which have a minimal area of $(\lambda_0/4)^2$.

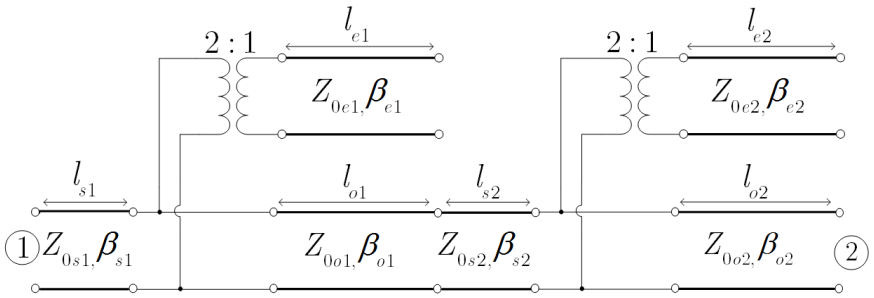

Figure 6.2 – Circuit model of a second-order multimodal band-stop filter with quarter-wavelength ($\lambda_{0e}/4$) even-mode resonators.

The required impedances for a second-order band-stop filter are [39]

$$Z_{0e1} = Z_M \left[1 + \frac{1}{\alpha g_0 g_1}\right], \tag{6.1}$$

which is the first resonator even-mode impedance. As defined in Chapter 2, $Z_M = Z_{0s1}/4$. The second resonator even-mode impedance is

$$Z_{0e2} = Z_M \left[g_0/\alpha g_2\right], \tag{6.2}$$

The immitance inverter, which is embedded in the CPW section (odd-mode), has an impedance of

$$Z_{12inv} = 4 \cdot Z_M \left[1 + \alpha g_0 g_1\right]. \tag{6.3}$$

The bandwidth parameter is $\alpha = \cot\left[(\pi/2)\,(1 - FBW/2)\right]$, and the output impedances is $Z_{0o2} = Z_{0s1} g_0 g_3$, where g_0,g_1,g_2 and g_3 are the normalized elements of a second-order low-pass filter prototype [39].

Using 6.1–6.3, a band-stop filter with a central frequency $f_0 = 2.2$ GHz and a $FBW = 0.26$ with a Butterworth response was designed. The chosen slotline impedance was $Z_{0s1} = 100\Omega$. The calculated impedances of the second-order filter are shown in Table 6.2.

CPW even-mode impedance, Z_{0e1}	110.36 Ω
CPW odd-mode impedance, Z_{0o1}	129.28 Ω
CPW even-mode impedance, Z_{0e2}	85.36 Ω

Table 6.1 – Calculated impedances of the of a second-order multimodal band-stop filter with quarter-wavelength ($\lambda_{0e}/4$) even-mode resonators.

The parameters of the substrate are: relative permittivity $\varepsilon_r = 3.02$,with a thickness 1.52 mm and a metallization thickness of 0.035 mm. The width of the strips of the input slotline is $w_{sg} = 2.5$ mm, with a slotline slot width $s = 0.4$ mm. The CPW central-strip width of the first resonator is $w = 0.15$ mm. Its slot width is $s = 0.25$ mm, the total slotline slot width is $2s + w$, and lateral-ground-plane width is $w_g = 1.5$ mm. The CPW central-strip width of the second resonator is $w = 0.15$ mm, its slot width is $s = 0.1$ mm, the slotline slot width is $2s + w$, and the lateral-ground-plane width is $w_g = 2$ mm. The length of each section is shown in Table 6.2.

Length of input slotline section, l_{s1}	1 mm
Length of 1st resonator even-mode section, l_{e1}	26.6 mm
Length of 1st resonator odd-mode section, l_{o1}	27.4 mm
Length of the inter-resonator slotline section, l_{s2}	0.95 mm
Length of 2nd resonator even-mode section, l_{e2}	26.5 mm
Length of 2nd resonator odd-mode section, l_{o2}	26.5 mm
Total area of the filter	55.4 mm × 5.4 mm

Table 6.2 – Calculated lengths of the second-order multimodal band-stop filter with quarter-wavelength ($\lambda_{0e}/4$) even-mode resonators.

The filter length is approximately a half of the guided wavelength at f_0, and its total area is just $(\lambda_{0s}/2) \times (\lambda_{0s}/20)$). The filter was measured using SG/GS probes. A comparison between the circuit model (taking into account transmission-line losses) and the measured data of a filter is shown in Fig. 6.3. The measured relative bandwidth is $FBW = 0.26$ and the maximum attenuation is 30 dB. The difference below the pass band (from 0.1 GHz to 1.2 GHz), is attributed to a common-mode excitation in the SG/GS probes due to the proximity of metallic mechanical supports of the probe station [25].

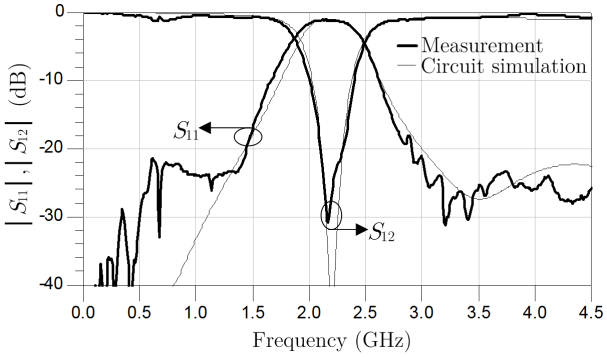

Figure 6.3 – Comparison between measured data and the multimodal circuit model of the fabricated second-order quarter-wavelength band-stop filter .

The wide-band response of the filter is shown in Fig. 6.4. As can be seen, the filter has a first harmonic stop band at 6.4 GHz, as expected for a quarter-wavelength filter. To obtain a better match between the equivalent circuit and the measured data, the parasitics produced by the slotline impedance steps

must be added to the equivalent circuit. The maximum return loss is affected by these parasitics, therefore impedance steps must be avoided whenever possible.

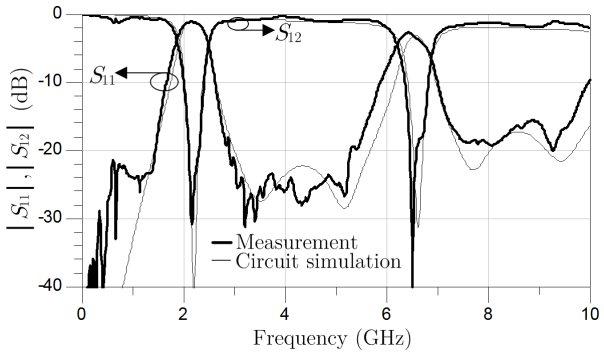

Figure 6.4 – Wide-band comparison between measured data and the multimodal circuit model of the fabricated second-order band-stop filter.

6.2 Band-stop filter based on CPW asymmetric series impedances

A band-stop filter, based on CPW-asymmetric series impedances is shown in Fig. 6.5. As explained in Chapter 2, each resonator is composed of a CPW section (limited by air-bridges) that contains a series-connected slotline, terminated with an open circuit. In this filter, a CPW slow-wave structure, similar to those proposed in [65], has been used to reduce the length of the CPW sections. Each resonator is separated by a even-mode slow-wave CPW line, with a length $l_{inv} \approx \lambda_e/4$. The multimodal circuit model of the band-stop filter is shown in Fig. 6.6.

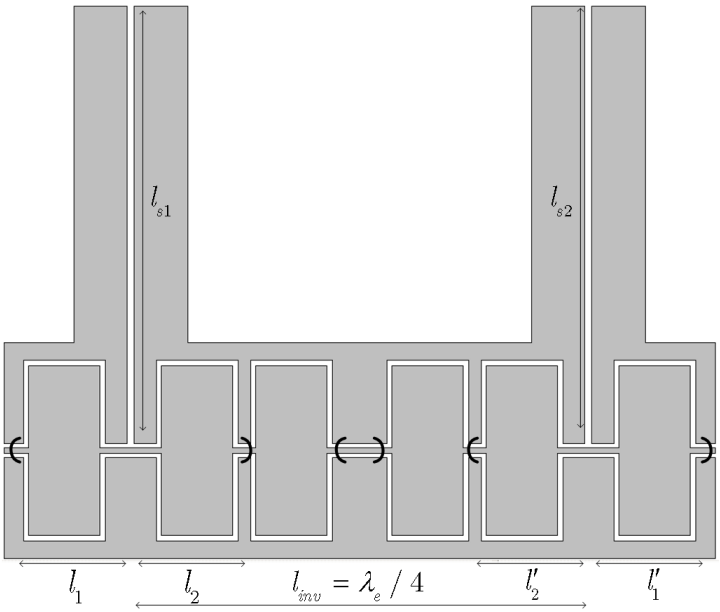

Figure 6.5 – Second-order multimodal band-stop filter based on CPW-asymmetric series impedances (open-circuited slotline stubs).

Using the circuit model of 6.6, a second-order multimodal band-stop filter was designed and implemented. The design parameters are: central frequency f_0 = 1.8 GHz with a fractional bandwidth FBW = 0.1 , and a Butterworth response. The parameters of the chosen substrate are: relative permittivity ε_r = 3.02 , thickness of 1.52 mm and metallization thickness of 0.035 mm. The CPW slow-wave sections have a slot width s = 0.125 mm, and the widths of the central CPW strips are w_1 = 0.150 mm

and $w_2 = 4.75$ mm. The lateral-ground-plane width is $w_{g1} = 2.825$ mm for the first section and $w_{g2} = 0.5$ mm for the wider CPW section . The width of the strips of the open-circuited slotline stubs is $w_{sg} = 1.5$ mm, with a slotline slot $s = 0.2$ mm. The length of each section is shown in Table 6.3.

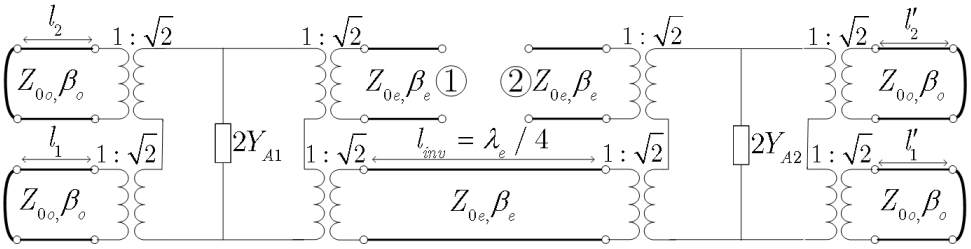

Figure 6.6 – Circuit model of a second-order multimodal band-stop filter based on CPW-asymmetric series impedances.

The synthesis method explained in Chapter 2 (Section 2.3.1) and the circuit model of Fig. 6.6 has been used to calculate the required lengths. The short-circuited odd-mode CPW stubs, which provide the inductive elements, have a physical length $l_1 = l_2 = l'_1 = l'_2 = 3.1$ mm, which represents an electrical length of 17.5°. The open-circuited slotline stubs have a physical length of $l_{s1} = l_{s2} = 13$ mm, which represents an electrical length of 45°. Therefore, the total area of the second-order filter is $(\lambda_{0s}/5) \times (\lambda_{0s}/6)$.

Lengths of CPW sections, $l_1 = l_2 = l'_1 = l'_2$	3.1 mm
Length of slotline sections, $l_{s1} = l_{s2}$	13 mm
Length of 1st-resonator odd-mode section, l_{inv}	6.3 mm
Total area of the filter	19.5 mm × 16.4 mm

Table 6.3 – Calculated lengths of the of a second-order multimodal band-stop filter with quarter-wavelength ($\lambda_{0e}/4$) even-mode resonators.

A comparison between the circuit model (taking into account transmission line losses) and the measured data of a filter is shown in Fig. 6.7. The measured fractional bandwidth is $FBW = 0.095$ and the maximum attenuation is 17.8 dB. Although this type of filter has higher losses than the quarter-wavelength band-stop filters shown in Section 6.1, it is more compact.

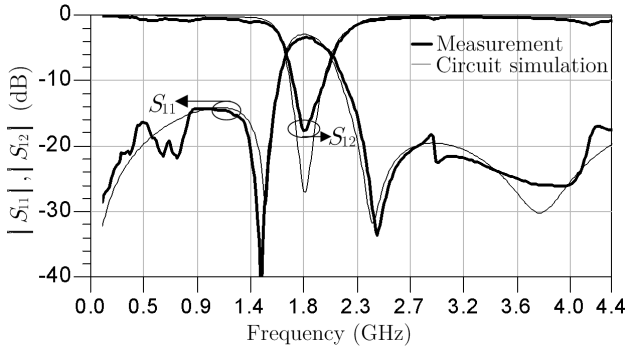

Figure 6.7 – Comparison between measured data and the multimodal circuit model of the fabricated second-order band-stop filter based on CPW asymmetric-series impedances.

CHAPTER 7

CONCLUSIONS AND FUTURE WORK

7.1 Multimodal Bandpass filters

In this work, new multimodal resonators and filters were developed, which feature a compact area, easy reconfiguration and the possibility of generate additional transmission zeros, with a performance similar of better than existing traditional monomodal CPW structures. A synthesis method (based on multimodal circuit models) has been developed for every multimodal filter presented in this work.

Chapter 2 (Section 2.1) describes the circuit models and design equations of basic structures based on CPW asymmetrical series and shunt impedances. Chapter 2 also deals with CPW circuits with slotline-CPW tees, which can be used as immittance inverters or to reduce the length of a slotline section.

Using structures based on CPW asymmetrical shunt impedances, new multimodal immitance inverters (MII) based on shunt-short-circuit CPW transitions have been presented and analyzed. These type of inverters enable the design of compact filters with improved out-of-band rejection.

In Chapter 4 (Section 4.1.2) the MIIs are used to design new structures for uniplanar bandpass filters of arbitrary order. The multimodal immitance inverters perform the mode conversion between the exciting CPW even modes and the inner slotline modes, implement part of the slotline resonator as a CPW odd-mode stub, and allow the addition of frequency traps within the resonator structure to suppress spurious harmonic passbands. These inverters have been characterized by means of a rigorous multimodal circuit model and analytical design expressions for their parameters.

By using these multimodal immitance inverters, several uniplanar multimodal bandpass filters have been designed, thus contributing to the development of a general theory of uniplanar filters, which use multimodal CPW sections. The proposed filters combine the usual even-mode excitation with the versatility and robustness of slotline resonators concerning bending easiness, fabrication tolerances, absence of spurious modes, and easiness of reconfiguration. These are intrinsically CPW designs since they do not replicate classical monomodal filter structures, but on the contrary, take advantage of the CPW multimodal properties to achieve their filter functionality. As demonstrated by the experimental results presented in Section 4.1.2, the insertion loss of the implemented second-order filter with half-wavelength slotline resonators and SLS sections (Section 4.1.2.2) is 1.8 dB at 2 GHz, with a very wide rejection of harmonic passbands. The second-order filter with quarter-wavelength resonators (Section 4.1.2.3) exhibits a minimum insertion loss of 1.6 dB at 1.95 GHz, and very compact size (25.4 mm × 18.95 mm). The fourth-order filter with quarter-wavelength slotline resonators exhibits an insertion loss of 2.2 dB at 2 GHz, and an out-of-band rejection of 20 dB up to 50 GHz. The out-of-band rejection has been improved by using even-mode resonators, which can be also used to design band-stop filters as shown in Chapter 6 (Section 6.1), where a second-order multimodal band-stop filter with quarter-wavelength ($\lambda_{0e}/4$) even-mode resonators a compact area ($\lambda_{0s}/2$) × ($\lambda_{0s}/20$) has been demonstrated. Moreover, a compact band-stop filter based on CPW asymmetrical series impedances has been described in Section 6.2, which also has a small area of ($\lambda_{0s}/5$) × ($\lambda_{0s}/6$).

7.2 Tunable and reconfigurable multimodal bandpass filters

As an added feature to this work, new topologies of tunable and reconfigurable multimodal microwave filters were developed. Section 5.1.1 describes a second-order bandwidth-reconfigurable bandpass filter, which can be easily reconfigured using PIN diodes, as shown in Chapter 5 (Section 5.1). Experimental results showed that this type of reconfigurable filter has a low insertion loss in both states (below 1.4 dB at 2 GHz) and good return loss. In addition, the bandwidth-reconfigurable filter has a third state (when all diodes are turned off), in which the structure behaves like a 50Ω transmission line, thus it can be used as a switchable filter.

Several reconfigurable filter topologies based on multimodal immitance inverters are presented in Chapter 5. In Section 5.1, a varactor-tuned filter, featuring a tuning range of 1.002–1.374 GHz with quasi-constant 3-dB bandwidth (from 121 to 135 MHz) and insertion loss in the range 2.17–3.45 dB has been presented. Section 5.3 describes a K-band RF-MEMS uniplanar reconfigurable-bandwidth second-order filter, that uses 3-bit switched capacitor banks to change its resonant frequency (only 3 switches per resonator are used), and can achieve a tuning range of half an octave. The RF-MEMS filter exhibits excellent power handling capabilities, since it can support an input power of nearly 1.5 W without reaching its compression point. Section 5.4 shows a K-band uniplanar second-order half-wavelength coupled-resonator filter featuring multimodal impedance inverters and an inter-resonator coupling which are easily reconfigured using low-voltage RF-MEMS ohmic-contact switches. Its 3-dB *FBW* can be changed by 90%, maintaining the same type of Butterworth response. Section 5.5 describes a quarter-wavelength reconfigurable filter based on RF-MEMS switchable air-bridges (SABs), which change both the inverter constants and the slotline-resonator lengths. The measured insertion loss of the reconfigurable filter based on SABs is below 4.7 dB for both states, in the expected range for planar filter topologies using high-resistivity silicon substrates, and its 3-dB *FBW* is the same for the two frequency states. This filter is able to shift upwards its center frequency; therefore this type of reconfiguration could be used in combination with varactor-loaded resonators to expand the frequency range.

In general, multimodal filters based on CPW asymmetrical shunt impedances are an example of how the additional degrees of freedom (as compared to classical monomodal CPW topologies) can be used to develop new topologies of reconfigurable filters.

7.3 Bandpass filter based on slotline-CPW tees

By using slotline-CPW tees it is possible to reduce dramatically the length of a slotline, as shown in Chapter 2 (Section 2.2.1.1). It has been proven that by using the multimodal circuit models and design equations presented in Section 2.2, it is possible to design new topologies of uniplanar band-pass filters based on slotline-CPW tees.

As an example, new compact filters with a reduced length have been shown in Chapter 4. In Section 4.2.2, it has been proven that by using slotline-CPW tees, the length of a second-order quarter-wavelength filter (which normally has a length of $\lambda_s/2$) can be reduced to just $0.16\lambda_s$. Also, in Section 4.2.3, a new uniplanar second-order quarter-wavelength filter has been presented, featuring low insertion loss and a reduced area of just $(\lambda_{0s}/7) \times (\lambda_{0s}/6)$. Slotline filters using multimodal slotline-CPW tees can be used to implement ultra-compact uniplanar diplexers, since the length of the interconnecting slotlines can be reduced as well. Moreover, the theory presented in Section 2.2 can be used to design new types of band-pass and band-stop filters, which feature a compact area compared to traditional uniplanar structures.

7.4 Future work

7.4.1 Ultra-compact filters based on slotline-CPW tees

Multilayer techniques have been extensively used in microwave circuits with the aim of achieving high density [66, 67]. Uniplanar circuits can be easily integrated in multilayer modules, since they do not require a backside ground plane.

Filters using slotline-CPW tees, to reduce the length (Section 4.2.2) or as immitance inverters; use input and output capacitive couplings (J_{01} and J_{23}) which use a large portion of the total area. Fig. 7.1 shows a second-order quarter-wavelength multimodal bandpass filter with a single slotline-CPW tee as immitance inverter (K_{12}), which can be designed using the theory presented in Chapter 2 (section 2.2.2). The area of the filter could be greatly reduced by using a second layer (as shown in Fig. 7.1) to form an integrated metal-isolator-metal (MIM) capacitor, winch can be used as input and output admittance inverters (J_{01} and J_{23}). This could be done using any multilayer process, including LTCC technology. An added advantage of using LTCC is that the lengths of the slotline-CPW transition will be reduced due to the higher effective permittivity of the internal layers (red layer in Fig. 7.1), compared to the top layers (yellow layer in Fig. 7.1).

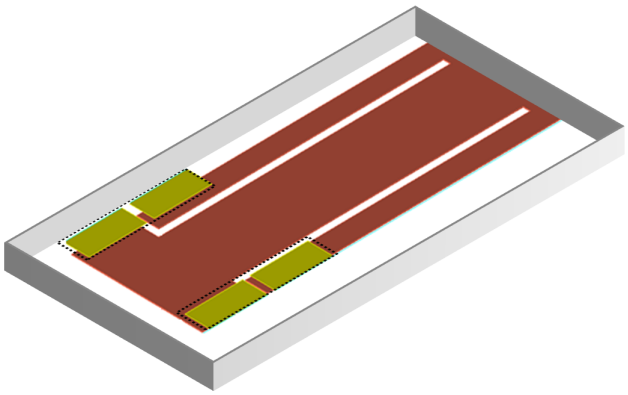

Figure 7.1 – 3-D layout of a compact second-order quarter-wavelength two-layer multimodal bandpass filter with a single slotline-CPW tee as immitance inverter. The yellow layer is on the top of the substrate (top layer of MIM capacitors are also SG/GS probe pads), while the red layer is an internal layer. The MIM capacitors (inside dotted lines) are the input J_{01} and output J_{23} couplings of the filter.

7.4.2 Tunable Multimodal matching networks and impedance tuners based on slotline-CPW tees

If the two fundamental modes of the CPW are used in slotline-CPW tees, new multimodal matching networks and impedance tuners can be designed. For example, a multimodal impedance tuner can be more compact and can achieve a better coverage since both modes of the CPW are used, which translates in more states if each CPW mode can be independently affected, by means of active devices such as varactor diodes or RF-MEMS capacitive and ohmic switches.

7.4.3 Compact multimodal circuits using even-mode and odd-mode slow-wave structures

Slow-wave CPW lines have been studied extensively in the past, but always as monomodal transmission lines. By analyzing the characteristic parameters of each CPW mode in a slow-wave structure, it is possible to design reduced-length multimodal filters. This technique could be used in combination with slotline-CPW tees which, as demonstrated in Chapter 2, can be used to reduce the length of slotline sections. Both approaches can be used to design more complex topologies such as diplexers and multiplexers.

APPENDIX A

RF-MEMS SWITCHES MASK SET

A.1 Mask of a RF-MEMS capacitive switch.

Fig. A.1 shows the mask set of the capacitive switch presented in Chapter 3 (Section 3.1.3, Fig. 3.7).

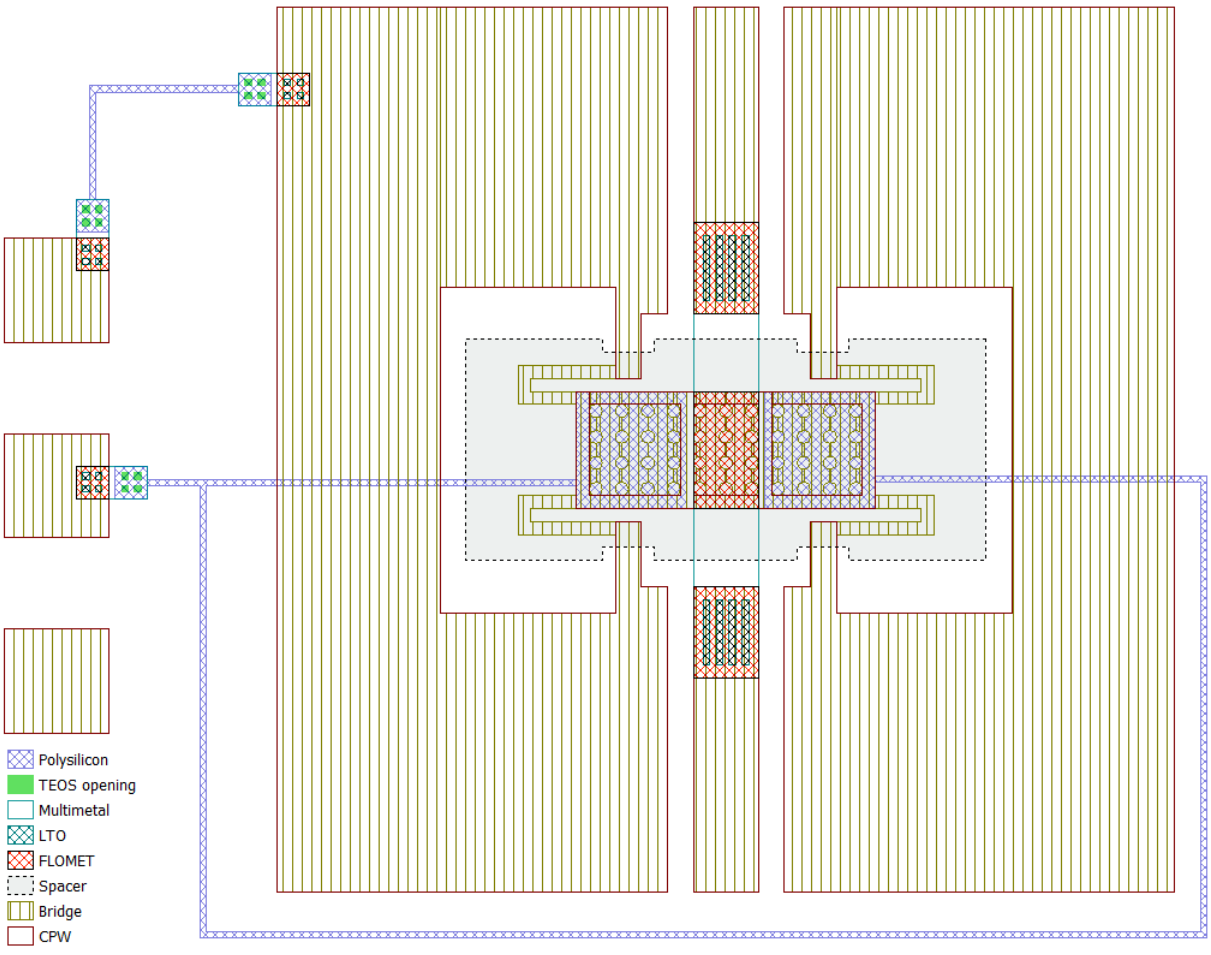

Figure A.1 – Mask of the capacitive switch presented in Chapter 3 (Section 3.1.3).

A.2 Mask of a RF-MEMS switchable air-bridge (quartz substrate).

Fig. A.1 shows the mask set of the ohmic switch presented in Chapter 3 (Section 3.1.4.1, Fig. 3.11), which was fabricated on a quartz substrate.

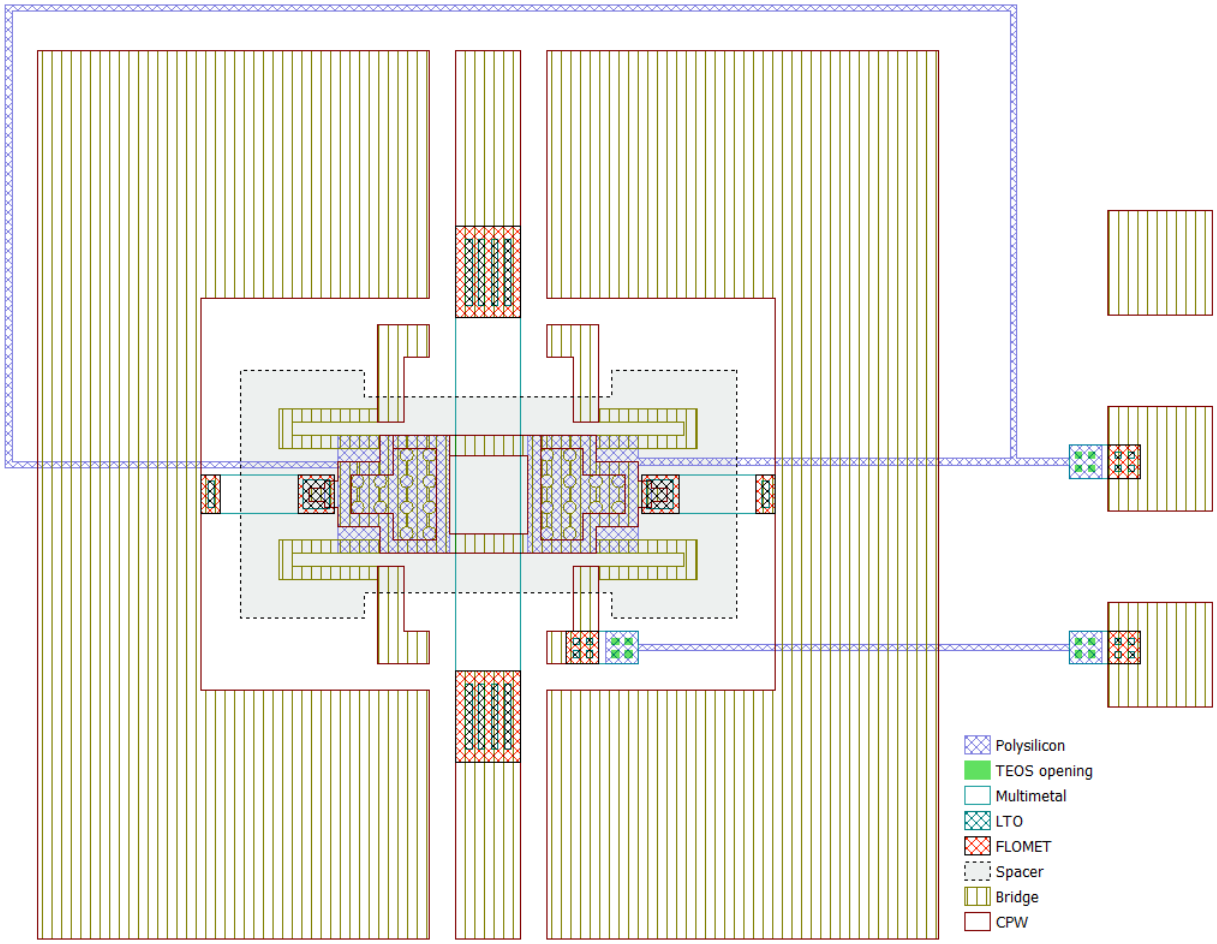

Figure A.2 – Mask of a RF-MEMS ohmic switch (SAB) fabricated on a quartz substrate.

A.3 Mask of a RF-MEMS switchable air-bridge (silicon substrate).

Fig. A.3 shows the mask set of the ohmic switch presented in Chapter 3 (Section 3.1.4.2, Fig. 3.18), which was fabricated on a silicon substrate.

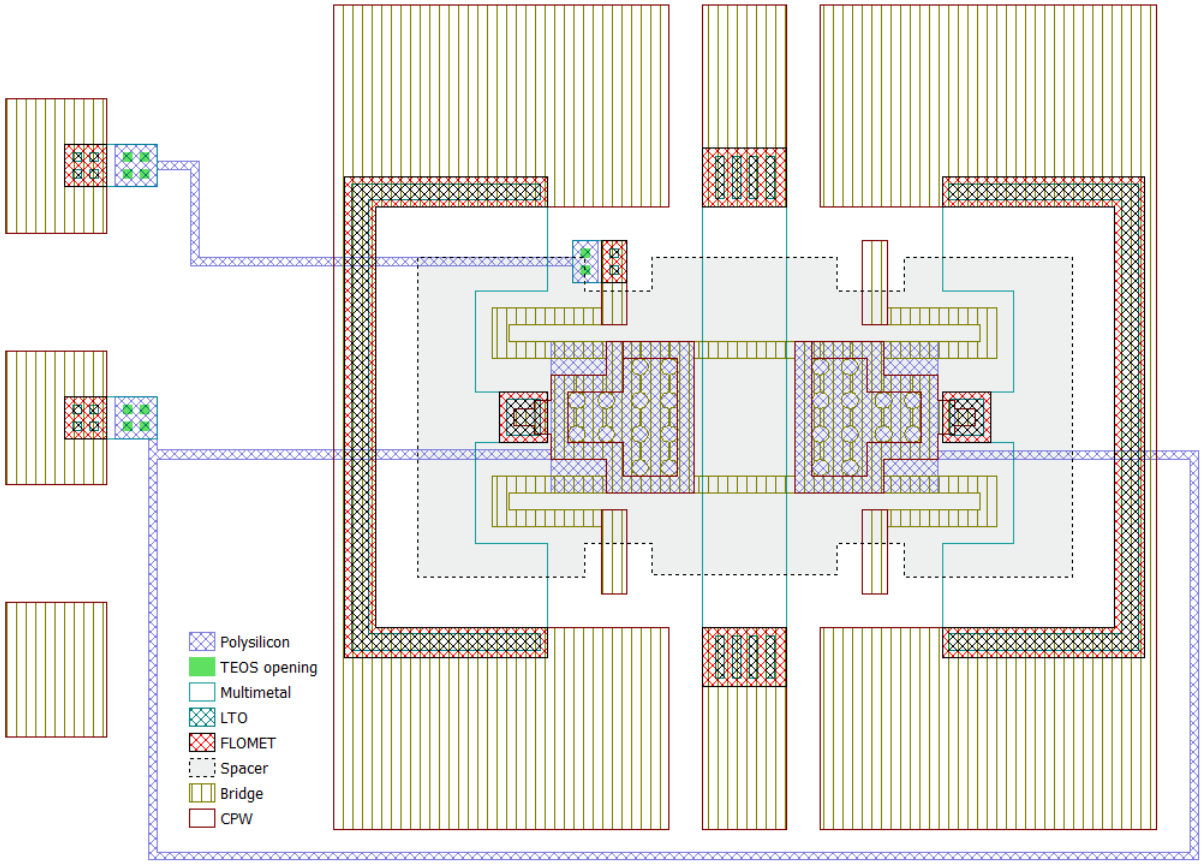

Figure A.3 – Mask of a RF-MEMS ohmic switch (SAB) fabricated on a silicon substrate.

A.4 Mask of switched capacitor bank.

Fig. A.4 shows the mask set of the switched capacitor bank presented in Chapter 3 (Section 3.1.5, Fig. 3.20 (a)).

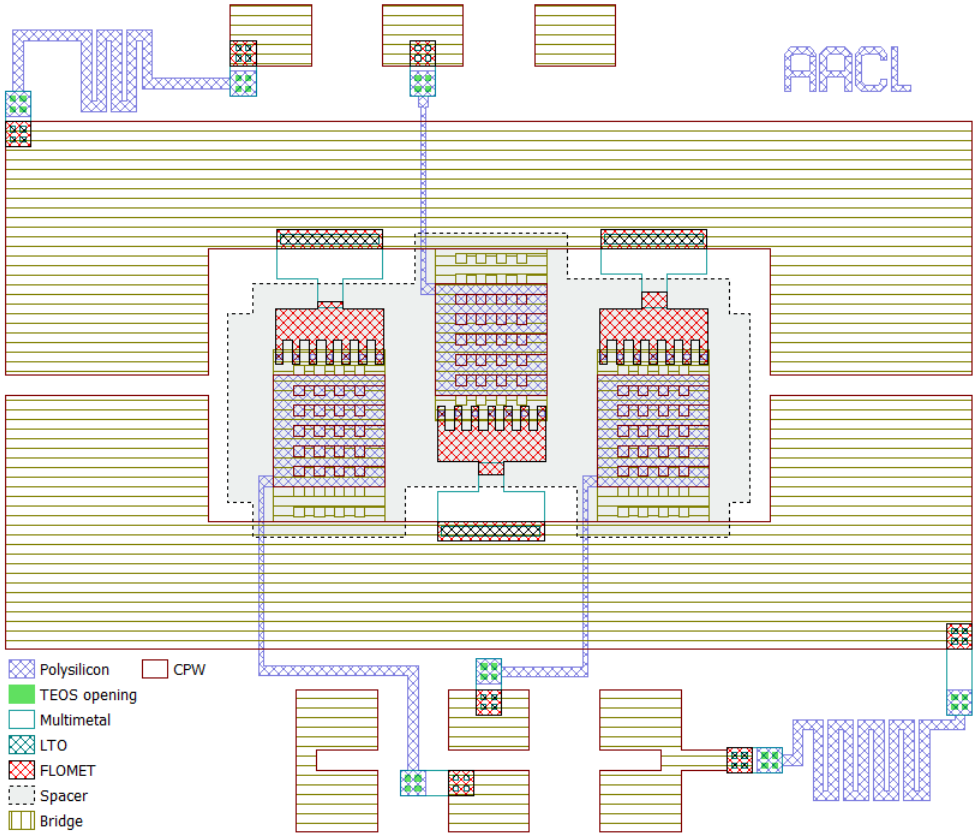

Figure A.4 – Mask of the RF-MEMS switched capacitor bank presented in Chapter 3 (Section 3.1.5).

APPENDIX B

SELECTED MULTIMODAL CIRCUIT MODELS IN AGILENT ADS

B.1 Circuit model of a filter with MIIs and quarter-wavelength slotline resonators

Fig. B.1 shows the Agilent ADS circuit model of a filter with multimodal immittance inverters (MIIs) and quarter-wavelength slotline resonators, similar than the ones introduced in Chapter 4 (Section 4.1.2.3). As can be seen in Fig. B.1 the design equations and characteristic parameters of the CPW (even and odd modes) and slotline sections are shown. This filter uses even-mode stubs to add transmission zeros at 6.8 GHz and 10.7 GHz (the filter was measured up to 10 GHz, therefore the transmission zero at 10.7 GHz is not shown in Fig. B.2).

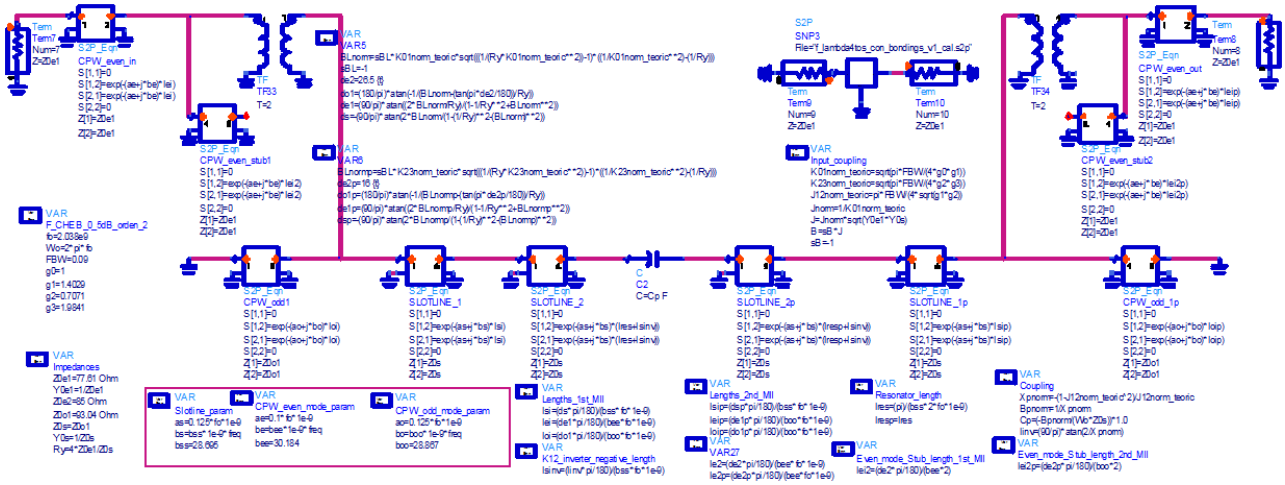

Figure B.1 – Agilent ADS circuit model of a filter with multimodal immittance inverters (MIIs) and quarter-wavelength slotline resonators.

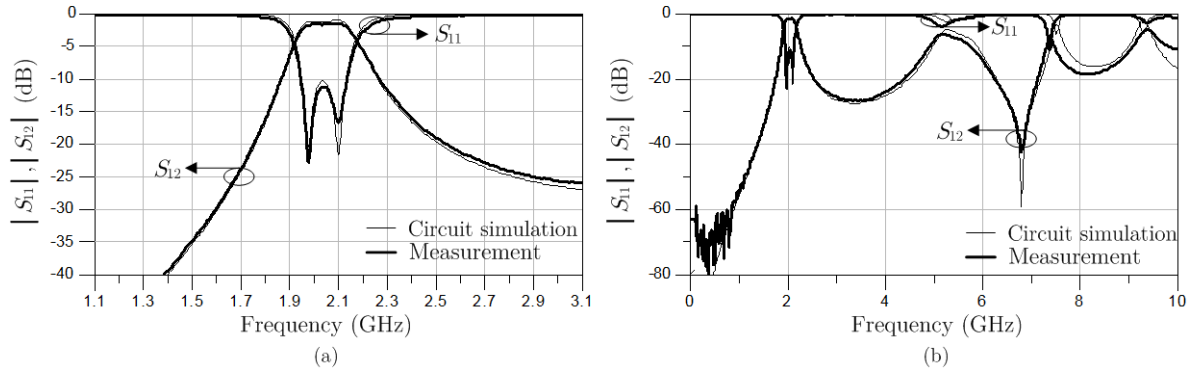

Figure B.2 – Comparison between measurement and circuit simulation (using the circuit model of Fig. B.1) of a second-order filter with multimodal immittance inverters (MIIs) and quarter-wavelength slotline resonators. (a) Narrow-band. (b) Wide-band.

B.2 Uniplanar delay line using multimodal slotline-CPW tees

Fig. B.3 shows the Agilent ADS circuit model of the uniplanar delay line of Fig. 2.18 (Chapter 2, Section 2.2.1.1).

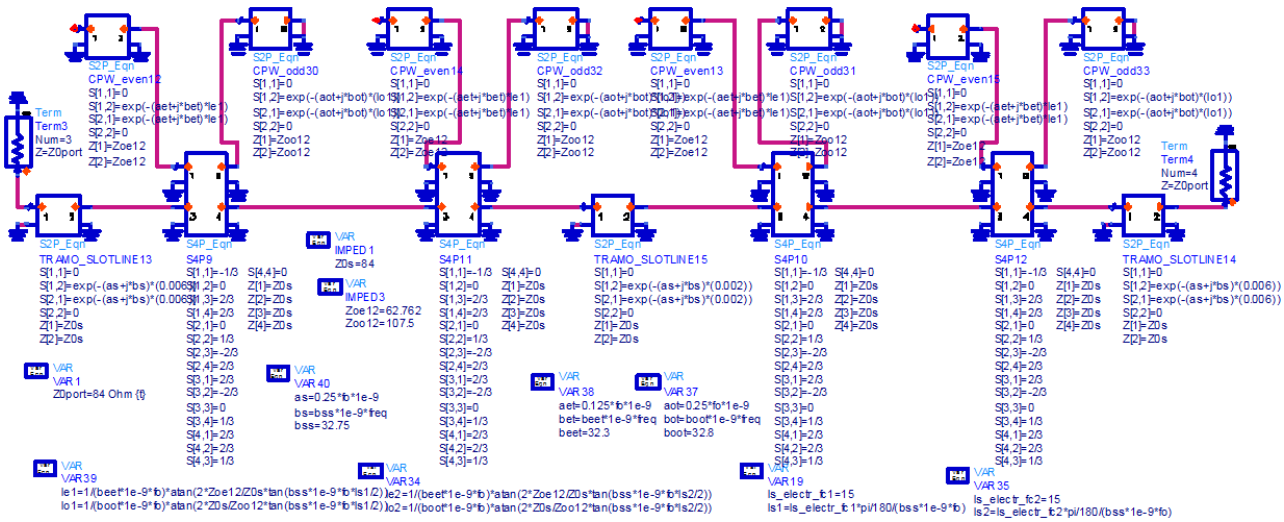

Figure B.3 – Agilent ADS circuit model of the uniplanar delay line of Fig. 2.18.

B.3 Circuit model of a filter with MIIs and multomodal slotline-CPW tees for length reduction

Fig. B.4 shows the Agilent ADS circuit model of the filter of Fig. 4.19 (Chapter 4, Section 4.2.1).

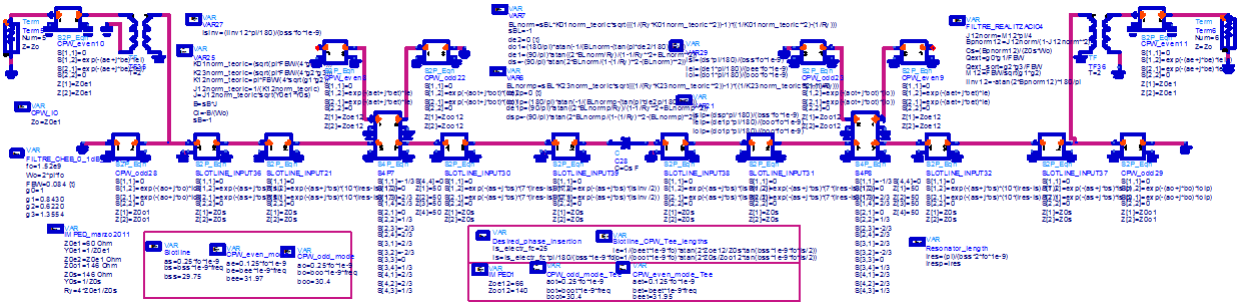

Figure B.4 – Agilent ADS circuit model of a filter with multimodal immittance inverters (MIIs) and quarter-wavelength slotline resonators, with slotline-CPW tees to reduce the lenght.

LIST OF PUBLICATIONS

Journal articles

[J1] A. Contreras, M. Ribó, L. Pradell, J. Casals-Terré, F. Giacomozzi, and J. Iannacci, "K-band RF-MEMS uniplanar reconfigurable-bandwidth bandpass filter using multimodal immittance inverters," *Electronics Letters*, vol. 49, no. 11, pp. –, 2013.

[J2] A. Contreras, M. Ribó, L. Pradell, and P. Blondy, "Uniplanar bandpass filters based on multimodal immittance inverters and end-coupled slotline resonators," *Microwave Theory and Techniques, IEEE Transactions on*, vol. 61, no. 1, pp. 77–88, 2013.

Conference articles

[C1] A. Contreras, J. Casals-Terré, L. Pradell, F. Giacomozzi, J. Iannacci, and M. Ribó, "Reconfigurable Multimodal Bandpass Filter Based on RF-MEMS Switchable CPW Air-Bridges," To appear in *Proceedings of Microwave Integrated Circuits Conference (EuMIC), 2013 8th European*, 2013.

[C2] A. Contreras, J. Casals-Terré, L. Pradell, F. Giacomozzi, S. Colpo, J. Iannacci, and M. Ribó, "Reconfigurable uniplanar bandpass filter based on RF-MEMS switched capacitors", *14th International Symposium on RF MEMS and RF Microsystems, MEMSWAVE 2013*, June 2013.

[C3] A. Contreras, J. Casals-Terré, L. Pradell, F. Giacomozzi, S. Colpo, J. Iannacci, and M. Ribó, "A RF-MEMS switchable CPW air-bridge," in *Microwave Integrated Circuits Conference (EuMIC), 2012 7th European*, 2012, pp. 441–444.

[C4] A. Contreras, J. Casals-Terré, L. Pradell, F. Giacomozzi, S. Colpo, J. Iannacci, and M. Ribó, "Conmutadores RF-MEMS de baja tensión," in *XXVI Simposio Nacional de la Unión Científica Internacional de Radio, URSI*, Sept. 2012.

[C5] A. Contreras, J. Casals-Terré, L. Pradell, F. Giacomozzi, S. Colpo, J. Iannacci, and M. Ribó, "Low-Voltage Capacitive and Ohmic RF-MEMS Switches", *13th International Symposium on RF MEMS and RF Microsystems, MEMSWAVE 2012*, June 2012.

[C6] A. Contreras, L. Pradell, and M. Ribó, "A novel tunable multimodal bandpass filter," in *Microwave Conference (EuMC), 2011 41st European*, 2011, pp. 1059–1062.

[C7] A. Contreras, M. Ribó, L. Pradell, "Filtro uniplanar multimodal reconfigurable", *XXVI Simposio Nacional de la Unión Científica Internacional de Radio, URSI*, Sept. 2011.

[C8] A. Contreras, M. Ribó, L. Pradell, "Modelado circuital multimodal de un resonador pasobanda reconfigurable", *XXV Simposium Nacional de la Unión Científica Internacional de Radio, URSI*, Sept. 2010.

BIBLIOGRAPHY

[1] M. Ribó, "Modelatge multimodal de transicions i asimetries en guies d'ones coplanars," Ph.D. dissertation, Universitat Ramon Llull, 2001.

[2] M. Llamas, D. Girbau, M. Ribo, L. Pradell, F. Giacomozzi, and S. Colpo, "RF-MEMS Uniplanar 180º Phase Switch Based on a Multimodal Air-Bridged CPW Cross," *Microwave Theory and Techniques, IEEE Transactions on*, vol. 59, no. 7, pp. 1769–1777, 2011.

[3] D. Girbau, "MEMS switches and capacitors for microwave communications systems," Ph.D. dissertation, Universitat Politècnica de Catalunya, 2006.

[4] L. Castaner and S. Senturia, "Speed-energy optimization of electrostatic actuators based on pull-in," *Microelectromechanical Systems, Journal of*, vol. 8, no. 3, pp. 290–298, 1999.

[5] F. Giacomozzi, V. Mulloni, S. Colpo, J. Iannacci, B. Margesin, and A. Faes, "A flexible technology platform for the fabrication of RF-MEMS devices," in *Semiconductor Conference (CAS), 2011 International*, vol. 1, 2011, pp. 155–158.

[6] J. Navarro and K. Chang, "Varactor-tunable uniplanar ring resonators," *Microwave Theory and Techniques, IEEE Transactions on*, vol. 41, no. 5, pp. 760–766, 1993.

[7] K. Hettak, N. Dib, A.-F. Sheta, and S. Toutain, "A class of novel uniplanar series resonators and their implementation in original applications," *Microwave Theory and Techniques, IEEE Transactions on*, vol. 46, no. 9, pp. 1270–1276, 1998.

[8] R. Simons, *Coplanar Waveguide Circuits, Components, and Systems*, ser. Wiley Series in Microwave and Optical Engineering. Wiley, 2004.

[9] K. Hettak, G.-Y. Delisle, and L. Talbi, "A 38-GHz integrated uniplanar subsystem for high-speed wireless broad-band multimedia systems," *Microwave Theory and Techniques, IEEE Transactions on*, vol. 47, no. 6, pp. 935–942, 1999.

[10] K. Hettak, N. Dib, A. Omar, G.-Y. Delisle, M. Stubbs, and S. Toutain, "A useful new class of miniature CPW shunt stubs and its impact on millimeter-wave integrated circuits," *Microwave Theory and Techniques, IEEE Transactions on*, vol. 47, no. 12, pp. 2340–2349, 1999.

[11] I. Wolff, *Coplanar Microwave Integrated Circuits*. Wiley, 2006.

[12] K. Hettak, T. Laneve, and M. Stubbs, "Size-reduction techniques for CPW and ACPS structures," *Microwave Theory and Techniques, IEEE Transactions on*, vol. 49, no. 11, pp. 2112–2116, 2001.

[13] K. Hettak, G. Morin, and M. Stubbs, "Compact MMIC CPW and asymmetric CPS branch-line couplers and Wilkinson dividers using shunt and series stub loading," *Microwave Theory and Techniques, IEEE Transactions on*, vol. 53, no. 5, pp. 1624–1635, 2005.

[14] S.-C. Lin, T.-N. Kuo, Y.-S. Lin, and C. H. Chen, "Novel coplanar-waveguide bandpass filters using loaded air-bridge enhanced capacitors and broadside-coupled transition structures for wide-band spurious suppression," *Microwave Theory and Techniques, IEEE Transactions on*, vol. 54, no. 8, pp. 3359–3369, 2006.

[15] M. Ribó, J. De la Cruz, and L. Pradell, "Circuit model for mode conversion in coplanar waveguide asymmetric series-impedances," *Electronics Letters*, vol. 35, no. 21, pp. 1851–1853, 1999.

[16] M. Ribó and L. Pradell, "Circuit model for mode conversion in coplanar waveguide asymmetric shunt impedances," *Electronics Letters*, vol. 35, no. 9, pp. 713–715, 1999.

[17] ——, "Circuit model for coplanar-slotline tees," *Microwave and Guided Wave Letters, IEEE*, vol. 10, no. 5, pp. 177–179, 2000.

[18] ——, "Circuit model for a coplanar-slotline cross," *Microwave and Guided Wave Letters, IEEE*, vol. 10, no. 12, pp. 511–513, 2000.

[19] L. Zhu, "Unified 3-D definition of CPW- and CSL-mode characteristic impedances of coplanar waveguide using MOM-SOC technique," *Microwave and Wireless Components Letters, IEEE*, vol. 13, no. 4, pp. 158–160, 2003.

[20] M. Llamas, M. Ribó, D. Girbau, and L. Pradell, "A Rigorous Multimodal Analysis and Design Procedure of a Uniplanar 180 Hybrid," *Microwave Theory and Techniques, IEEE Transactions on*, vol. 57, no. 7, pp. 1832–1839, 2009.

[21] M. Llamas, D. Girbau, M. Ribó, L. Pradell, A. Lazaro, F. Giacomozzi, and B. Margesin, "MEMS-Based 180º Phase Switch for Differential Radiometers," *Microwave Theory and Techniques, IEEE Transactions on*, vol. 58, no. 5, pp. 1264–1272, 2010.

[22] K. Goverdhanam, R. N. Simons, and L. P. B. Katehi, "Coplanar stripline propagation characteristics and bandpass filter," *Microwave and Guided Wave Letters, IEEE*, vol. 7, no. 8, pp. 214–216, 1997.

[23] R. Azadegan and K. Sarabandi, "Miniature high-Q double-spiral slot-line resonator filters," *Microwave Theory and Techniques, IEEE Transactions on*, vol. 52, no. 5, pp. 1548–1557, 2004.

[24] J. Lee and K. Sarabandi, "A Miniaturized Conductor-Backed Slot-Line Resonator Filter With Two Transmission Zeros," *Microwave and Wireless Components Letters, IEEE*, vol. 16, no. 12, pp. 660–662, 2006.

[25] N. Yang, C. Caloz, K. Wu, and Z. N. Chen, "Broadband and Compact Coupled Coplanar Stripline Filters With Impedance Steps," *Microwave Theory and Techniques, IEEE Transactions on*, vol. 55, no. 12, pp. 2874–2886, 2007.

[26] A. Deleniv, M. Gashinova, A. Eriksson, and A. Khalabuhov, "Novel band-pass filter utilizing S-shaped slot line resonators," in *Microwave Symposium Digest, 2003 IEEE MTT-S International*, vol. 2, 2003, pp. 1081–1084 vol.2.

[27] S. Remillard, P. Radzikowski, S. Cordone, D. Applegate, A. Mehrotra, J. Kokales, and A. Abdelmonem, "A closed slot-line resonator filter," *Microwave and Wireless Components Letters, IEEE*, vol. 14, no. 5, pp. 234–236, 2004.

[28] Y.-H. Shu, J. Navarro, and K. Chang, "Electronically switchable and tunable coplanar waveguide-slotline band-pass filters," *Microwave Theory and Techniques, IEEE Transactions on*, vol. 39, no. 3, pp. 548–554, 1991.

[29] J.-X. Chen, Z.-H. Bao, C. Xu, and G.-A. Zhang, "Uniplanar tunable bandpass filter using centrally-loaded slot-line resonator," *Microwave and Optical Technology Letters*, vol. 52, no. 12, pp. 2805–2807, 2010.

[30] A. Gorur and C. Karpuz, "Uniplanar compact wideband bandstop filter," *Microwave and Wireless Components Letters, IEEE*, vol. 13, no. 3, pp. 114–116, 2003.

[31] G. Ponchak, J. Papapolymerou, and M. Tentzeris, "Excitation of coupled slotline mode in finite-ground CPW with unequal ground-plane widths," *Microwave Theory and Techniques, IEEE Transactions on*, vol. 53, no. 2, pp. 713–717, 2005.

[32] T. Weller, R. Henderson, K. J. Herrick, S. Robertson, R. Kihm, and L. P. B. Katehi, "Three-dimensional high-frequency distribution networks. I. Optimization of CPW discontinuities," *Microwave Theory and Techniques, IEEE Transactions on*, vol. 48, no. 10, pp. 1635–1642, 2000.

[33] J. Zhou, M. Lancaster, and F. Huang, "Compact superconducting coplanar meander line filters," *Electronics Letters*, vol. 39, no. 8, pp. 665–667, 2003.

[34] Y.-S. Lin, W.-C. Ku, C.-H. Wang, and C. H. Chen, "Wideband coplanar-waveguide bandpass filters with good stopband rejection," *Microwave and Wireless Components Letters, IEEE*, vol. 14, no. 9, pp. 422–424, 2004.

[35] C.-H. Wu, C.-H. Wang, Y.-S. Lin, and C. H. Chen, "Parallel-Coupled Coplanar-Waveguide Bandpass Filter With Multiple Transmission Zeros," *Microwave and Wireless Components Letters, IEEE*, vol. 17, no. 2, pp. 118–120, 2007.

[36] M. Rittweger, M. Abdo, and I. Wolff, "Full-wave analysis of coplanar discontinuities considering three-dimensional bond wires," in *Microwave Symposium Digest, 1991., IEEE MTT-S International*, 1991, pp. 465–468 vol.2.

[37] E. Soliman, P. Pieters, and E. Beyne, "Thin film tunnels versus air-bridges in coplanar waveguide discontinuities," in *Microwave Symposium Digest, 1998 IEEE MTT-S International*, vol. 2, 1998, pp. 1039–1042 vol.2.

[38] M. Llamas, "Circuitos de microondas uniplanares multimodales, reconfigurables," Ph.D. dissertation, Universitat Politècnica de Catalunya, 2009.

[39] B. Schiffman and G. Matthaei, "Exact Design of Band-Stop Microwave Filters," *Microwave Theory and Techniques, IEEE Transactions on*, vol. 12, no. 1, pp. 6–15, 1964.

[40] G. Matthaei, L. Young, and E. Jones, *Microwave filters, impedance-matching networks, and coupling structures*, ser. Artech House microwave library. McGraw-Hill, 1964, no. v. 1.

[41] J. Hong and J. Lancaster, *Microstrip Filters for RF/Microwave Applications*, ser. Wiley Series in Microwave and Optical Engineering. Wiley, 2004.

[42] G. Rebeiz, *RF MEMS: Theory, Design, and Technology*. Wiley, 2004.

[43] L. Castañer, J. Pons, R. Nadal-Guardia, and A. Rodríguez, "Analysis of the extended operation range of electrostatic actuators by current-pulse drive," *Sensors and Actuators A: Physical*, vol. 90, no. 3, pp. 181 – 190, 2001.

[44] S. Senturia, *Microsystem Design*. Springer, 2000.

[45] D. Peroulis, S. Pacheco, and L. P. B. Katehi, "RF MEMS switches with enhanced power-handling capabilities," *Microwave Theory and Techniques, IEEE Transactions on*, vol. 52, no. 1, pp. 59–68, 2004.

[46] B. Pillans, J. Kleber, C. Goldsmith, and M. Eberly, "RF power handling of capacitive RF MEMS devices," in *Microwave Symposium Digest, 2002 IEEE MTT-S International*, vol. 1, 2002, pp. 329–332 vol.1.

[47] A. Cruau, C.-M. Tassetti, P. Nicole, and G. Lissorgues, "Influence of RF signal power on tunable MEMS passive components," in *Microwave and Optoelectronics Conference, 2003. IMOC 2003. Proceedings of the 2003 SBMO/IEEE MTT-S International*, vol. 1, 2003, pp. 533–536 vol.1.

[48] J. Reid, L. Starman, and R. Webster, "RF actuation of capacitive MEMS switches," in *Microwave Symposium Digest, 2003 IEEE MTT-S International*, vol. 3, 2003, pp. 1919–1922 vol.3.

[49] J. Rizk, E. Chaiban, and G. Rebeiz, "Steady state thermal analysis and high-power reliability considerations of RF MEMS capacitive switches," in *Microwave Symposium Digest, 2002 IEEE MTT-S International*, vol. 1, 2002, pp. 239–243 vol.1.

[50] W. Thiel, K. Tornquist, R. Reano, and L. P. B. Katehi, "A study of thermal effects in RF-MEM-switches using a time domain approach," in *Microwave Symposium Digest, 2002 IEEE MTT-S International*, vol. 1, 2002, pp. 235–238 vol.1.

[51] B. D. Jensen, K. Saitou, J. Volakis, and K. Kurabayashi, "Fully integrated electrothermal multidomain modeling of RF MEMS switches," *Microwave and Wireless Components Letters, IEEE*, vol. 13, no. 9, pp. 364–366, 2003.

[52] F. Coccetti, B. Ducarouge, E. Scheid, D. Dubuc, K. Grenier, and R. Plana, "Thermal analysis of RF-MEMS switches for power handling front-end," in *Microwave Conference, 2005 European*, vol. 3, 2005, pp. 4 pp.–.

[53] F. Solazzi, C. Palego, S. Halder, J. Hwang, A. Faes, V. Mulloni, B. Margesin, P. Farinelli, and R. Sorrentino, "Electro-thermal analysis of RF MEM capacitive switches for high-power applications," in *Solid-State Device Research Conference (ESSDERC), 2010 Proceedings of the European*, 2010, pp. 468–471.

[54] C. Palego, F. Solazzi, S. Halder, J. Hwang, P. Farinelli, R. Sorrentino, A. Faes, V. Mulloni, and B. Margesin, "Effect of substrate on temperature range and power capacity of RF MEMS capacitive switches," in *Microwave Conference (EuMC), 2010 European*, 2010, pp. 505–508.

[55] D. Peroulis, S. Pacheco, K. Sarabandi, and L. P. B. Katehi, "Electromechanical considerations in developing low-voltage RF MEMS switches," *Microwave Theory and Techniques, IEEE Transactions on*, vol. 51, no. 1, pp. 259–270, 2003.

[56] F. Casini, P. Farinelli, G. Mannocchi, S. DiNardo, B. Margesin, G. De Angelis, R. Marcelli, O. Vendier, and L. Vietzorreck, "High performance RF-MEMS SP4T switches in CPW technology for space applications," in *Microwave Conference (EuMC), 2010 European*, 2010, pp. 89–92.

[57] N. Yang, C. Caloz, K. Wu, and Z. N. Chen, "Broadband and Compact Coupled Coplanar Stripline Filters With Impedance Steps," *Microwave Theory and Techniques, IEEE Transactions on*, vol. 55, no. 12, pp. 2874–2886, 2007.

[58] R. N. Simons, N. Dib, and L. P. B. Katehi, "Modeling of coplanar stripline discontinuities," *Microwave Theory and Techniques, IEEE Transactions on*, vol. 44, no. 5, pp. 711–716, 1996.

[59] L. Zhu and K. Wu, "Field-extracted lumped-element models of coplanar stripline circuits and discontinuities for accurate radiofrequency design and optimization," *Microwave Theory and Techniques, IEEE Transactions on*, vol. 50, no. 4, pp. 1207–1215, 2002.

[60] A. Pothier, J.-C. Orlianges, G. Zheng, C. Champeaux, A. Catherinot, D. Cros, P. Blondy, and J. Papapolymerou, "Low-loss 2-bit tunable bandpass filters using MEMS DC contact switches," *Microwave Theory and Techniques, IEEE Transactions on*, vol. 53, no. 1, pp. 354–360, 2005.

[61] C. Lugo, G. Wang, J. Papapolymerou, Z. Zhao, X. Wang, and A. Hunt, "Frequency and Bandwidth Agile Millimeter-Wave Filter Using Ferroelectric Capacitors and MEMS Cantilevers," *Microwave Theory and Techniques, IEEE Transactions on*, vol. 55, no. 2, pp. 376–382, 2007.

[62] E. Pistono, P. Ferrari, L. Duvillaret, J.-M. Duchamp, and R. Harrison, "Hybrid Narrow-Band Tunable Bandpass Filter Based on Varactor Loaded Electromagnetic-Bandgap Coplanar Waveguides," *Microwave Theory and Techniques, IEEE Transactions on*, vol. 53, no. 8, pp. 2506–2514, 2005.

[63] A. C. Reyes, S. El-Ghazaly, S. Dorn, M. Dydyk, D. Schroder, and H. Patterson, "Coplanar waveguides and microwave inductors on silicon substrates," *Microwave Theory and Techniques, IEEE Transactions on*, vol. 43, no. 9, pp. 2016–2022, 1995.

[64] J. Iannacci, F. Giacomozzi, S. Colpo, B. Margesin, and M. Bartek, "A general purpose reconfigurable MEMS-based attenuator for Radio Frequency and microwave applications," in *EUROCON 2009, EUROCON '09. IEEE*, 2009, pp. 1197–1205.

[65] A. Gorur, C. Karpuz, and M. Alkan, "Characteristics of periodically loaded CPW structures," *Microwave and Guided Wave Letters, IEEE*, vol. 8, no. 8, pp. 278–280, 1998.

[66] P. Pursula, T. Karttaavi, M. Kantanen, A. Lamminen, J. Holmberg, M. Lahdes, I. Marttila, M. Lahti, A. Luukanen, and T. Vaha-Heikkila, "60-GHz Millimeter-Wave Identification Reader on 90-nm CMOS and LTCC," *Microwave Theory and Techniques, IEEE Transactions on*, vol. 59, no. 4, pp. 1166–1173, 2011.

[67] I. Wolff, "Design and Technology of Microwave and Millimeterwave LTCC Circuits and Systems," in *Signals, Systems and Electronics, 2007. ISSSE '07. International Symposium on*, 2007, pp. 505–512.